UNIVERSITY OF SOUTHAMPTON
FACULTY OF ENGINEERING, SCIENCE AND MATHEMATICS
SCHOOL OF ENGINEERING SCIENCES

NUMERICAL MODELLING OF SUPERCONDUCTING COMPOSITES IN AC MAGNETIC FIELDS

by

Marta Costa Bouzó

Thesis for the degree of DOCTOR OF PHILOSOPHY
NOVEMBER 2004

UNIVERSITY OF SOUTHAMPTON

ABSTRACT

FACULTY OF ENGINEERING, SCIENCE AND MATHEMATICS
SCHOOL OF ENGINEERING SCIENCES

Doctor of Philosophy

NUMERICAL MODELLING OF SUPERCONDUCTING COMPOSITES IN AC MAGNETIC FIELDS

by Marta Costa Bouzó

This thesis is focused on numerical modelling of high-temperature superconductors (HTS) for the purpose of a better understanding of the loss mechanisms which occur in alternating magnetic fields and whose consequences still constitute one of the remaining obstacles for practical applications of superconductivity.

The Critical State Model, developed for low temperature superconductors, only gives a qualitative approximation of the electromagnetic behavior of high temperature superconductors. For precise quantitative analysis, HTS are well described by a non linear current-voltage characteristic, as the power law $E(J) = E_c(J/J_c)^n$ assigned to superconductors modelled in this work. For studying HTS with such non-linear property and with complex geometries numerical methods are necessary.

For modelling infinite long tapes with rectangular cross-sections a simple 2D integral formulation developed by Brandt is used, which results in a stiff differential equation for the current density. To solve it, Rosenbrock method was implemented and validated.

A extensive part of this thesis is dedicated to the coupling effect between superconductors via a resistivity matrix, for which analytical calculations are limited to a very simple situation. Such 3D effect is modelled in superconductors with finite dimensions using the finite element method (FEM) software Flux3D. Due to the highly non-linear E-J law, initial tests using Flux3D showed the inefficiency of the linear system solver used at each Newton-Raphson step. To improve the general performance of Flux3D new iterative solvers, Gmres and Bi-CGStab, were implemented. FEM simulations were carried out to study the coupling phenomenon in strips and slabs superconductors.

For the particular case of infinite slabs or thin discs, the 3D coupling effect can be modelled by using a 2D formulation based on a extension of Brand's formulation for the sheet current in thin finite superconductors. Being simpler than FEM, this method is found to be successful for modelling the coupling phenomenon at different applied fields, and therefore was used to analyze the influence of different geometrical and physical characteristics of superconductors on the coupling effect.

Contents

Acknowledgements

First of all, I wish to express my gratitude to my supervisor, Yifeng Yang, for his support and for his helpful guidance, comments and suggestions, essential for carrying out this thesis. I am also grateful to Carlo Beduz for his advises and support.

I would like to thank all colleagues from the department for their help and collaboration, and for the enjoyable atmosphere created during these years.

Thanks to staff members at the University for their advise in their respective areas.

Finally, many special thanks to all my family members and my friends for their support and for all the good moments during my experience in England.

Chapter 1

Introduction to high-T_c superconductivity

1.1 What is Superconductivity?

Superconductivity is a strange phenomenon characterized by the zero resistance which is observed in some materials when they are cooled below a certain temperature known as *critical temperature* T_c.

1.2 History of superconductivity

Superconductivity was discovered in 1911 by Heike Kamerlingh Onnes [26]. He was examining the properties of the electric resistance in metals at low temperatures when he observed that electric resistivity of the mercury cooled by liquid helium decreased with falling the temperature and disappeared at 4.15 K. In the next years, many other metals and alloys were found to be superconducting if they are cooled at sufficiently low temperatures, under 23 K.

Since there is not resistance at all, the superconductor can carry current indefinitely provided that the temperature is kept low. The requirement of such extreme temperatures can only be reached with some expensive gases as liquid helium.

It was in 1986 when the history of high temperature superconductivity began, when Karl Müller and J. George Bednorz observed superconductivity in lanthanum copper oxides doped with barium at temperatures up to 38 K [6]. One year later, in 1987,

superconductivity was found at 93 K in the compound yttrium barium copper oxide (YBCO)[39]. At that temperature YBCO can be cooled in liquid nitrogen, more abundant and cheaper than liquid helium. In the following years intense attention was put to find other copper oxides superconductors at higher temperatures. So far, one of the superconductors at highest temperature is the HBCCO (mercury barium calcium copper oxide) with $T_c = 133\,\mathrm{K}$ [2].

Since the discovery of high-temperature superconductors the superconductivity research focused in different directions. Whereas some researches try to find superconductors at higher and higher temperatures, other people work in the improvement of the properties of already discovered superconductors around 100 K, and investigate their possible practical applications.

1.3 Applications of superconductivity

Superconductivity can be applied to different areas of science and engineering. As they become more cost effective, future expansion of theses applications can be assured in many cases.

Applications of high temperature superconductors include superconducting motors, fault-current limiters, generators, energy storage systems, power cables, magnetic shielding devices, medical imaging systems, superconducting quantum interference devices (SQUIDS), infrared sensors, analog signal processing devices, microwave devices, etc.

The property of superconductors to conduct electricity with high current density and zero resistance can be exploited in the use of electrical transmission lines, where in traditional conductors part of generated electricity is dissipated in resistive losses. Similarly, superconducting motors and generators could be made with a weight of about one tenth that of conventional ones of the same power, therefore at lower costs, thank to the high currents that a HTS wire can carry.

Superconductors are used in many applications where intense magnetic fields are required since superconducting magnets are cheaper than conventional ones, more compact and can produce higher fields. In medical applications, the superconducting magnet has been used in magnetic resonance imaging (MRI) of many parts of the human body. The intense magnetic fields and the uniformity in space and time needed for such applications can be reached maintaining the coils in theirs superconducting state. Similarly, particle accelerators can increase their energy level by using superconducting magnets.

Superconducting accelerators projects are developed in CERN laboratory in Switzerland and Fermilab in USA.

Based on the property of magnetic field repulsion of superconductors (Meissner effect) other applications of superconductivity such as maglev exploit this unique feature of magnetic levitation. Prototypes of high speed levitated trains have already been constructed in Japan by using LTS with liquid helium as a refrigerant.

In the electronics industry, superconductors are used in ultra-high-performance filters. Since superconducting wire has near zero resistance, even at high frequencies, many more filter stages can be employed to achieve a desired frequency response. This is a great advantage in high-congestion radio frequency applications such as cellular telephone systems. Another electronic application is the possibility of building computers 1000 times faster than computers based on silicon chip technology. This is achieved through the use of basic Josephson junctions.

1.4 Principles of high-T_c superconductivity

Apart from the zero-resistance characteristic, another equally important property of superconductors, related to their behavior when they are exposed to a magnetic field, was discovered in 1933 by W.Meissner and R.Ochsenfeld [24]. They found that any magnetic field applied to a superconductor is expelled from inside it when the material is cooled below T_c. The same effect occurs regardless whether the superconductor is cooled below T_c prior or after the field is applied. Such total expulsion of magnetic field is known as *Meissner effect* (figure 1.1). Macroscopic theory of London brothers [22] and later in 1950 the theory of Ginzburg and Landau [14] propose equations to explain this effect.

The magnetization M of the material relates to the magnetic field H and the induction B by the relation $B = \mu_0(H + M)$. In the Meissner state $B = 0$ and therefore $M = -H$ (perfect diamagnetism).

For a given material, there is however a magnetic field sufficiently strong such that the field penetrates into the superconductor and the normal state is restored. This field is called the *critical magnetic field* ($H_c(T)$) and depends on the temperature, being higher for materials with high T_c. With regard to this feature superconductors are classify in two groups: Type-I and Type-II.

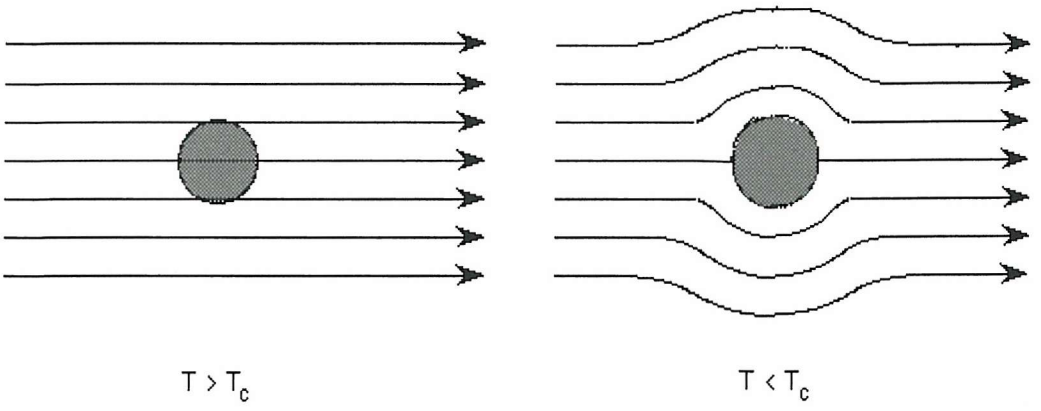

Figure 1.1: Meissner effect in a superconductor.

Type-I superconductors expel the applied field (Meissner effect) as it is lower than the critical magnetic field, $H_c(T)$. As the applied field exceeds $H_c(T)$, penetration occurs resulting in a transformation to normal state (See figure 1.2.(b)).

For Type-II Superconductors there are two critical fields. Field lines begin to penetrate into the material at H_{c1}, converting some regions to the normal state, while others are still superconducting. It is at a higher critical field H_{c2} when it becomes totally normal material. This behavior is shown in figure 1.3.

Type-I superconductors are comprised of pure metals, whereas Type-II superconductors are mostly alloys or intermetallic compounds. The critical field varies enormously between Type-I and Type-II superconductors. The maximum critical field (H_c) in any Type-I superconductor is about 2000 Gauss (0.2 T), but in Type-II materials, superconductivity can persist to several hundred thousand Gauss (H_{c2}). For Type-II superconductors, the critical fields and temperature are, in general, much higher than Type-I superconductors, so they have much more potential for applications.

In addition to critical temperature T_c and critical magnetic field $H_c(T)$, there is a *critical current* J_c, which is the maximum current that a superconductor can carry without any dissipation. Whereas in Type-I superconductors J_c depends only on H_c, in Type-II ones the three "criticals" are related forming a critical boundary surface $T - H - J$, below which the material is superconductor.

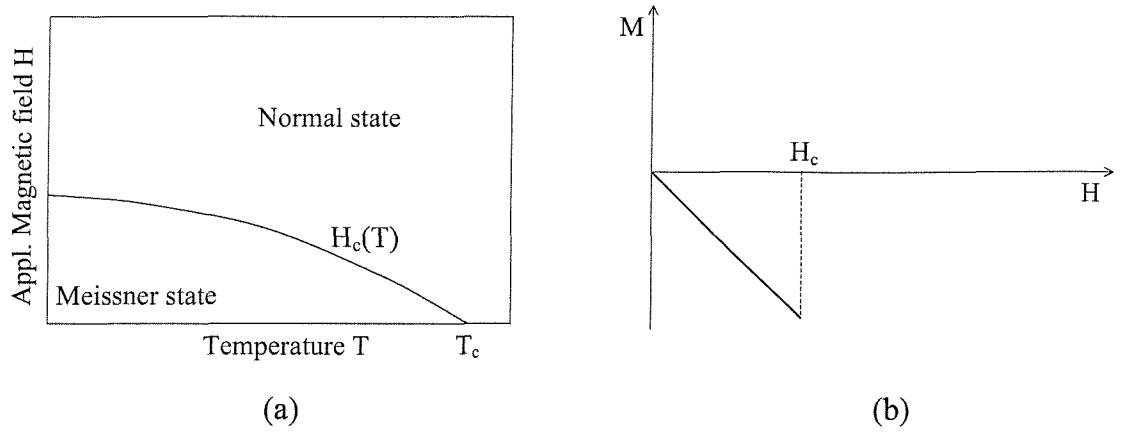

Figure 1.2: Critical magnetic field (a) and magnetization as a function of the applied magnetic field H for a Type-I superconductor (b). It shows perfect diamagnetism below H_c (M=-H), then it becomes normal material.

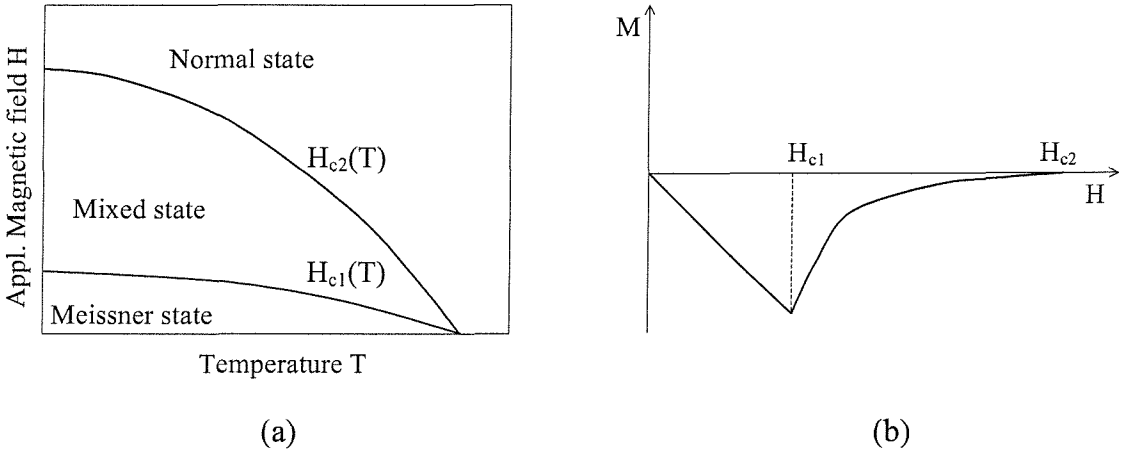

Figure 1.3: Critical magnetic field (a) and magnetization as a function of the applied magnetic field H for a Type-II superconductor (b). Above H_{c1} flux begins to penetrate until H_{c2} when there is no magnetization left.

A more detailed explanation of superconductivity is found in [33], [12], [11], [38], which have been used as references in this chapter.

1.5 Type-II superconductivity

In 1957 A. Abrikosov [1] presented the theory about the behavior of type-II superconductors based in the Ginzburg- Landau theories. He explained the three possible states depending on the critical temperature and critical magnetic field: normal, mixed and superconducting states.

Below H_{c1} all the magnetic flux is expelled and the superconductor behaves as a perfect diamagnet ($M = -H$). In the mixed state between the two critical fields, the magnetic field penetrates partially into the superconductor and normal and superconducting regions coexist. The field penetrates in the form of individual quantized flux lines which arrange themselves into a regular pattern of Abrikosov flux lattice, forming vortices of normal material. The vortices repel each other slightly and form a triangular lattice. A vortex has a non-superconducting core allowing the flux to pass through it, and is surrounded by a superconducting region as it is shown in figure 1.4.

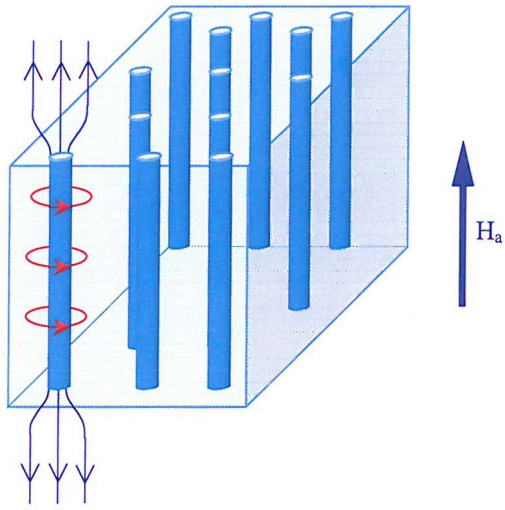

Figure 1.4: Mixed state of Type-II superconductors where magnetic flux lines penetrated the superconductor forming vortices. The vortex on the left shows the magnetic field passing through the core surrounded by superconducting currents.

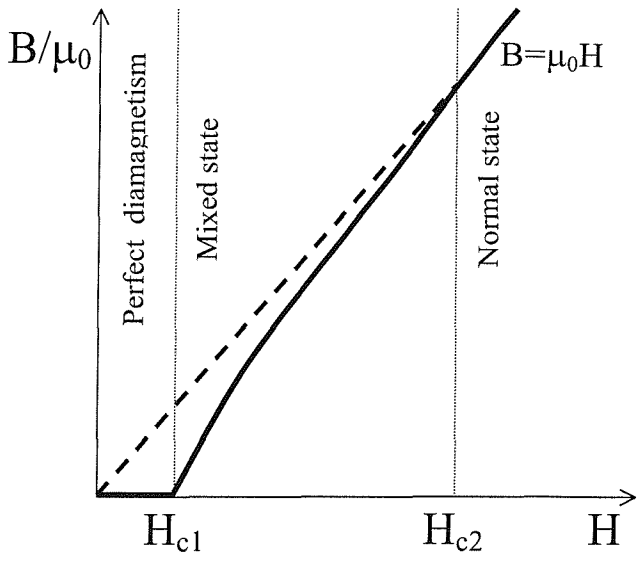

Figure 1.5: Internal and applied field for an ideal Type-II superconductor.

The number of flux vortices increases with increasing field. Above H_{c2}, the flux lines pile and there is not space for superconductivity which is destroyed.

Figure 1.5 shows the flux density inside the superconductor as a function of the applied field. Below H_{c1} the flux density is zero. For applied fields well above of H_{c1}, the magnetization becomes negligibly so $B \approx \mu_0 H$, and goes to zero at H_{c2} where $B = \mu_0 H$.

1.5.1 Flux pinning, flux flow, flux creep and $E-J$ characteristic

In a pure superconductor the vortex structure is in equilibrium, there is not force to move them. When current flows, the flux lines experiment a force, Lorentz force, which tries to move them ($F = J \times B$). This movement is stopped if there are impurities or imperfections in the material's structure, causing the flux lines to be trapped. This effect is known as *flux pinning*. There is a certain value of the current, denominated *critical current* (J_c), when the Lorentz force equalles to the finite pinning force. For a higher current density above J_c the vortices start to move (*flux-flow*) leading to dissipation.

For HTC superconductors at high operation temperatures flux motion may be activated by thermal fluctuation of the lattice, even below J_c. This motion is slower than flux flow and is known as *flux-creep*. At low temperatures up to 18 k, this phenomenon is insignificant and the induced voltage and resistance of the conductor is essentially zero.

But for 77 K it has to be taken into account.

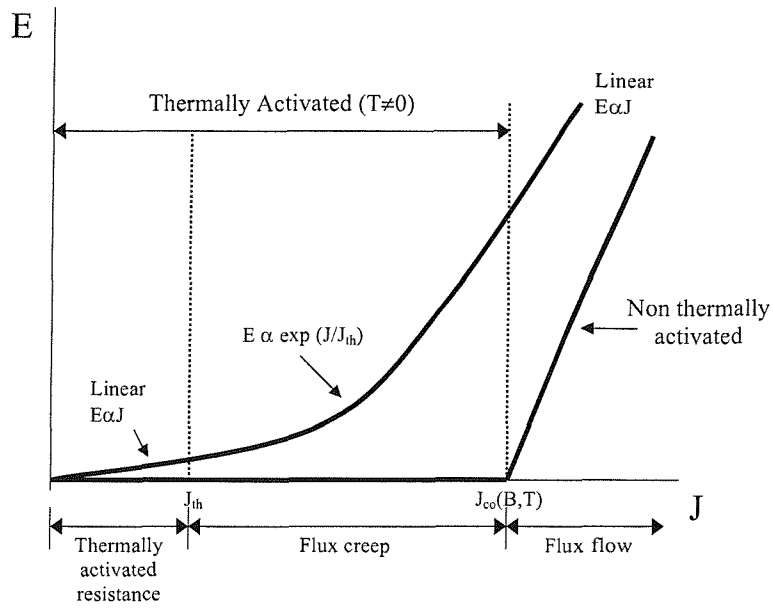

Figure 1.6: Electric field versus the current density under the influence of the thermally activated flux motion.

Figure 1.6 shows the electric field in function of the density current at a constant temperature showing the different states. Defining a current parameter J_{th} the three states are represented. J_{c0} is defined as the J_c value that would have obtained in the absence of flux creep.

1.5.2 Bean critical state model

Electrodynamics of type II superconductors due to an applied external field can be described by Bean's critical state model (1962) [5]. Critical sate model postulates that for low applied fields or currents, the outer part of the sample is in a "critical state" with special values of the current density and magnetic field, and the interior is shielded from these fields and currents. In particular, in Bean's model, the current is assumed to flow at a critical density J_c, independent of the time rate of change of the magnetic flux. Then, only three states for the current flow are possible when the magnetic field is applied: zero current for the regions not affected by the applied field and critical current

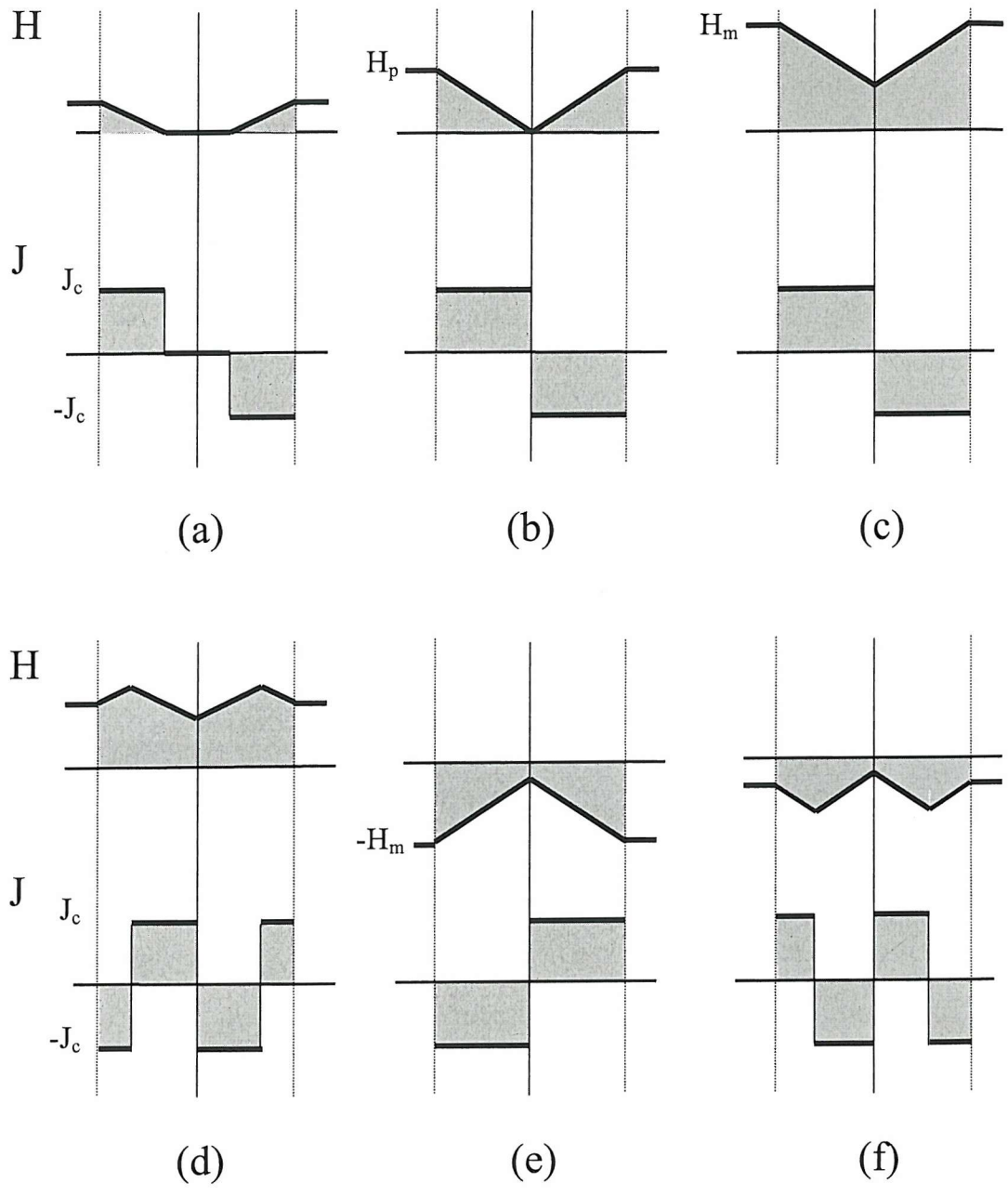

Figure 1.7: Bean critical state model for a infinite slab in an applied magnetic field.

for the rest.

As an example, consider an infinite slab of superconductor with a sinusoidal applied field parallel to one of its sides. The field is increasing from zero to a maximum value H_m and then is decreasing to $-H_m$. Figure 1.7 shows the field and current density inside the superconductor.

When the external field is applied, the currents start to flow producing a uniform field opposite to the applied field change. These currents flow at the critical density J_c and the field inside is given by $\nabla \times H = J$. At a low field (figure 1.7.(a)) there is a field and current free region near the center. At $H = H_p$ the fields and currents reach the center of the slab as shown in figure 1.7.(b). There is current flowing through the whole slab and the field reduces to zero at the center. H_p is denominated penetration field. If the field continues increasing, since the currents have already penetrated over the whole cross section, they can't oppose to the increment of the field which, therefore, increases in the whole conductor (figure 1.7.(c)). If the applied field is now decreased, the flux does not recede completely in the reverse order since some of it is trapped inside the slab. Currents start to flow in the outer part with reversed critical current to oppose to the decrease, however in the part where the magnetic field has not changed yet, the current remains flowing in the same direction (figure 1.7.(d)). This reversed current propagates inwards as the applied field is further reduced. When the applied field reaches $-H_m$, the field and current profiles are totally reversed as shown in figure 1.7.(e). Observe that the field inside exceeds the applied field which means the flux is trapped inside. As the applied field stars to increase again at the outer regions reversed current appears (figure 1.7.(f)).

1.5.3 Hysteresis in superconductors

Assuming Bean's critical state model and considering $M = \mu_0^{-1}B - H$, observe in figure 1.8 the magnetic behavior of type-II superconductors. For each value of H there are two possible values of M hence when H is cycled M does not return to its initial value. The magnetization saturates at $H = H_p$. When the applied field starts to decrease, the magnetization does not come back in reverse path since there is flux trapped in the material. It returns to zero when the internal field is equal to the applied field ($\mu_0^{-1}B = H$). The energy loss in one cycle is the area enclosed by this hysteresis loop in the plane of the magnetization M versus the applied magnetic field H.

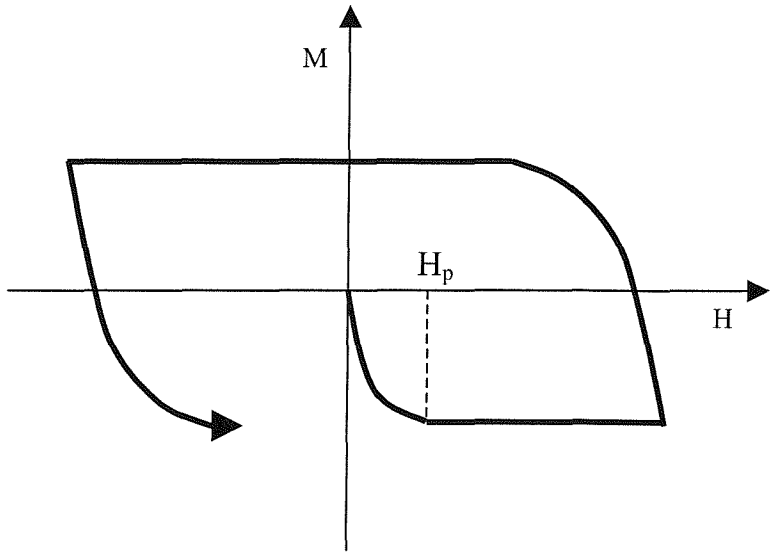

Figure 1.8: Hysteresis loop of magnetization M versus applied magnetic field H.

1.6 Ac losses

Although since type-II superconductors were discovered many improvements were done and many difficulties were solved, one of the remaining barriers for large scale power utilization of superconductors are the ac losses. In most of the applications in power engineering, the superconductor material is in presence of ac currents or changing magnetic fields , so there will be energy losses and the consequent heating generated in the superconductor will require a large amount of refrigerator power for its removal. This amount depends on the temperature at which the superconductor operates. For example, removing one watt of heat deposited at room temperature requires $500 - 1000$ W of refrigeration power at 4 K and 10 W at 77 K.

There are three different mechanisms of ac losses: hysteresis losses and self-field losses in the superconductor region, and eddy current losses in the normal material region.

1.6.1 Hysteresis losses

Hysteresis losses result from the magnetic hysteresis due to flux pinning. When a time-varying applied magnetic field penetrates into the superconductor and is increased, produces the constant movement of the vortices in the lattice, therefore an electric field is generated, and there is dissipating energy. Hysteresis losses vary depending on the

penetration depth of the magnetic flux.

Assuming the Bean critical state model, analytical formulas for the losses can be obtained for same simple configurations.

Usually, calculations of ac losses are done integrating the instantaneous power dissipation $E(r,t) \times J(r,t)$ within the superconductor volume surface. This integral is easily calculated since by Bean's model the current is equal to J_c and E is calculated as the change of the flux.

For a superconductor in presence of a magnetic field there is another way to calculate losses. The total loss per unit volume in a complete cycle is the area enclosed by the hysteresis loop in the plane of M versus H (figure 1.8).

For simple geometries, the critical state can be obtained exactly, as summarized next.

Slab parallel to the field

Consider an infinite slab of thickness $2a$ in an applied magnetic field parallel to the slab as it is shown in figure 1.9.(a) . Suppose that the field is reduced from the maximum value H_m to $-H_m$.

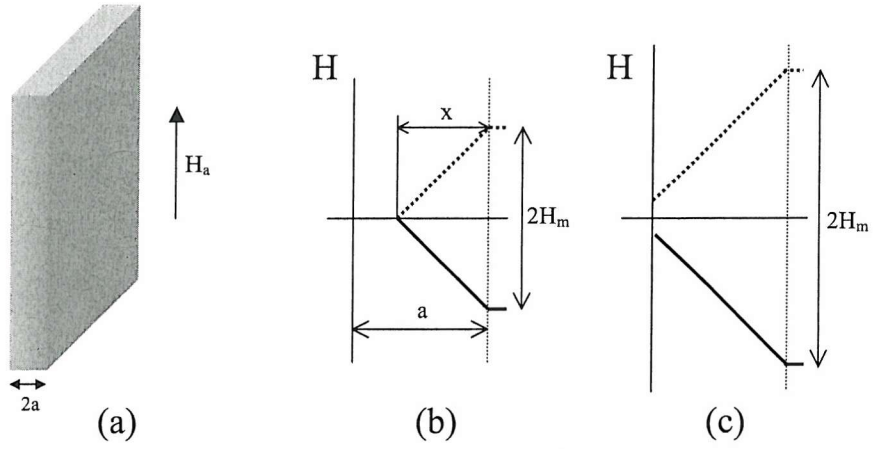

Figure 1.9: Superconducting slab in an ac applied field (a), and magnetic field profile inside the slab for $H < H_p$ (b) and $H > H_p$ (c).

Figure 1.9.(b) shows the field profile when $H_m \leq H_p$. H_p is the value of the field such

that the magnetic field reaches the center of the slab and from Bean's model is equal to $J_c a$. The hysteresis losses per cycle per unit volume, obtained integrating $E \cdot J$ over the volume, are

$$Q = 2\frac{1}{2a}\int_{-a}^{a} J_c \triangle\phi(x)\mathrm{d}x = \frac{2}{3}\mu_0 H_m^2 \left(\frac{H_m}{H_p}\right) \qquad H_m \leq H_p$$

For the case $H_m \geq H_p$ the slab is saturated at the peak field (figure 1.9.(c)), and the losses per unit volume per cycle Q are given by

$$Q = 2\frac{1}{2a}\int_{-a}^{a} J_c \triangle\phi(x)\mathrm{d}x = 2\mu_0 H_m^2 \left(\frac{H_p}{H_m} - \frac{2}{3}\left(\frac{H_p}{H_m}\right)^2\right) \qquad H_m \geq H_p$$

The first factor in both previous equations ($2\mu_0 H_m^2$) is the maximum volumetric energy stored by the magnetic field.

Similar to infinite slab, results can be obtained for a cylinder in a field parallel to its axis. When the applied field is perpendicular to the cylinder is more complicated since the field and current profiles are not one-dimensional functions. Wilson [38] derives an approximate solution for low fields below full penetration which has to be solved numerically.

Strip in perpendicular field

Consider a strip of zero thickness and width $2a$ as shown in figure 1.10.(a) with a finite critical current I_c.

The power loss is determined in [9] using the integration of $M\mathrm{d}H$. The field profiles in this geometry are non-linear due to the demagnetization field occurring at the strip edges (figure 1.10.(b)). The power loss per unit length is given by :

$$Q = \mu_0 2a H_m I_c \left(\frac{2I_c}{\pi H_m 2a}\ln\cosh\left(\frac{\pi H_m 2a}{I_c}\right) - \tanh\left(\frac{\pi H_m 2a}{I_c}\right)\right)$$

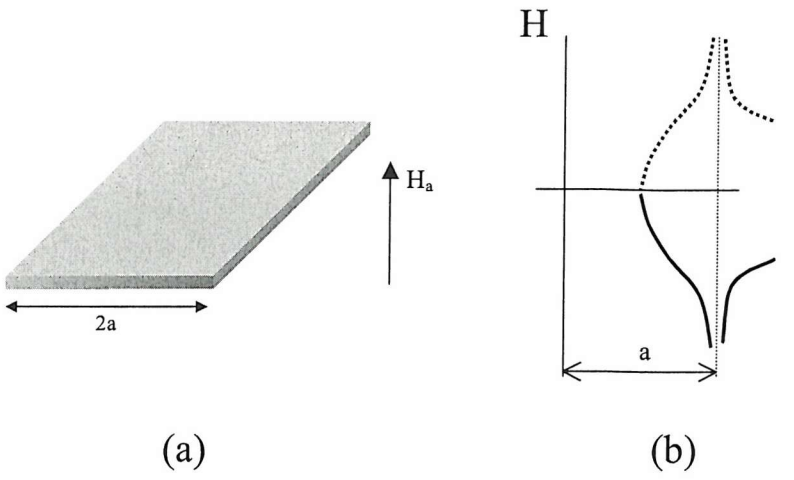

Figure 1.10: Superconducting strip in an ac applied field (a), and magnetic field profile when the field is decreased from H_m to $-H_m$ (b).

1.6.2 Self-field losses

Similarly to ac hysteresis losses due to an ac applied magnetic field described before, there are losses in a superconductor carrying ac transport current. The ac current creates a self-field varying in time, which induces the magnetic hysteresis and therefore dissipating energy, known as the *self-field losses.*

Self-field losses in a carrying current wire

In a wire carrying transport current, the self-field induced penetrates from the exterior and its flux lines form concentric lines around the wire (figure 1.11). The current flows parallel to the axis of the wire near the edges penetrating as far as it is needed to carry all the current.

In [41] an analytical formula for the loss is presented. Figure 1.11.(b) shows the profile of the self-field in a wire of radio a. The losses per cycle per unit length are given by

$$Q = \frac{\mu_0}{\pi}(I_c)^2 \left((1-i)\ln(1-i) + \frac{2-i}{i} \right) \qquad i < 1$$

where $i = I_m/I_c$, I_m the current peak, and $I_c = \pi a^2 J_c$.

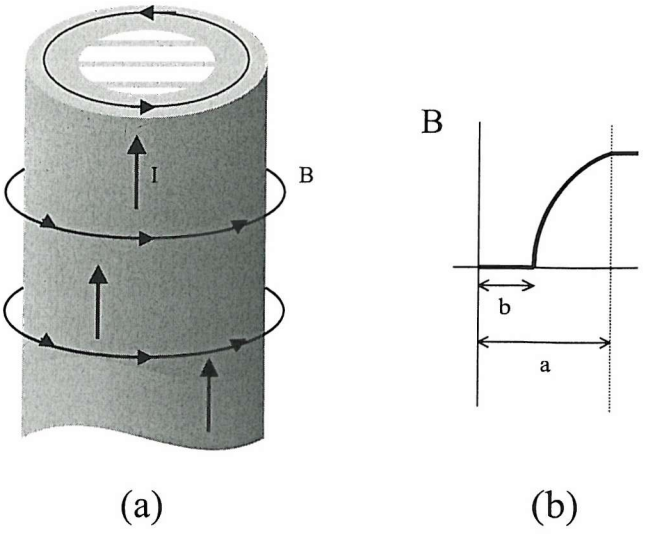

Figure 1.11: Self field in a superconducting wire carrying a transport current I (a), and magnetic field profile inside the wire (b).

This formula can be extended to wires with elliptic cross-section as it was calculated by Norris [25].

Self-field losses in a strip

Norris [25] calculated the self-field hysteresis loss for superconducting thin strips. The profile of the field is similar to the one represented in figure 1.10.(b) for a strip in an external field. The losses per cycle per unit length are

$$Q = \frac{\mu_0}{\pi}(I_c)^2 \left((1-i)\ln(1-i) + (1+i)\ln(1+i) - i^2\right) \qquad i < 1$$

1.6.3 Coupling in filamentary composites

To reduce the hysteresis losses and for stability reasons, superconductors are usually manufactured in form of filamentary composite, that is, fine superconductors embedded in a normal material matrix. However, in such configurations long length filaments can couple under ac magnetic fields hence defeat the objective of loss reduction by fine filaments.

There is a critical length l_c, for a given amplitude and frequency of the applied field, such that filaments longer than that length couple together leading to resistivity losses.

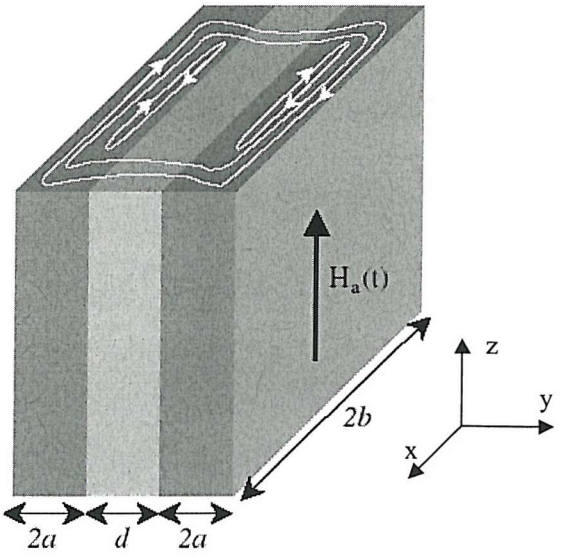

Figure 1.12: Coupling current between two slabs separated by a normal matrix.

Solutions to minimize theses losses are to increase the matrix resistivity or to twist the filaments together, with the twist-pitch length less than $2l_c$.

Coupling in slab geometry

The critical coupling length l_c can be obtained from the simple model of two parallel infinite slabs separated by a normal matrix and under the assumptions of Bean's model.

Consider two slabs with a normal conductor between them as it is shown in figure 1.12. In presence of an AC magnetic field in the z direction, current is induced to flow in each slab in the xy-planes. Assume the filaments have not resistance and all the voltage is across the matrix. Let $I(x)$ be the current in one of the slabs at distance x from the center of the slab. Between x and $x + \delta x$ let some of this current δI cross the normal matrix driven by the induced voltage, $V = -\frac{\partial \phi}{\partial t}$. Supposing that $\dot{B}$ is the same everywhere, then $V = \dot{B}dx$. Therefore

$$\delta I(x) = \dot{B}dx/(\rho d/\delta x)$$

Integrating this equation with the boundary conditions $I(b) = I(-b) = 0$, we obtain

$$I(x) = \dot{B}((2b)^2 - 4x^2)/(8\rho)$$

The maximum current is at the center, $x = 0$, and is limited by $2aJ_c$, which is the value reached when the slabs are fully coupled and all the current is flowing in one slab crossing through the matrix to the other.

Therefore there is a critical ramp rate of the field, $\dot{B}_c$, when the slabs are fully coupled, given by

$$\dot{B}_c = 16\rho J_c a/(2b)^2 \tag{1.1}$$

and the critical coupling length is $l_c = 2b_c$ with

$$b_c = 2\sqrt{\frac{\rho J_c a}{\dot{B}}} \tag{1.2}$$

1.6.4 Measurement of ac losses

There are two experimental ways to measure AC losses: calorimetrically or electrically. Here they will be briefly described using as references [38] and [41].

The calorimetric method consists on the measurement of the volume of gas which is boiled away by ac loss power or the heating of the sample. Figure 1.13 shows a simple arrangement for calorimetric measurement using the boil-off rate of helium gas. To obtain a good accuracy is important to separate the cryogen boil-off due to the cryostat heat leak, current leads, etc..The specimen is enclosed by a bell jar which is vented to the flow-measuring device, but the boil-off due to current leads and heat leak into the cryostat is vented separately. From the measurement of the volume flow rate $\dot{V}$ the mass flow rate $\dot{m}$ is obtained. Then knowing the latent heat of vaporization of the cryogen λ and its density, the power loss is easily calculated as $\dot{m}\lambda = \rho\lambda\dot{V}$. Liquid helium is suited for this method.

In [4] a simple technique using the temperature increase for measurement of losses due to ac magnetic fields and transport currents is presented. The ac losses are obtained by comparing the temperature increase after a fixed time of unknown ac power dissipation with that after the same time of known dc power dissipation.

The electrical method for loss measurement of isolated samples works by measuring of magnetic hysteresis using pick up coils , and for devices as coils relies on the measurement of the electric power supplied to them. This method is faster but more complex than calorimetric techniques.

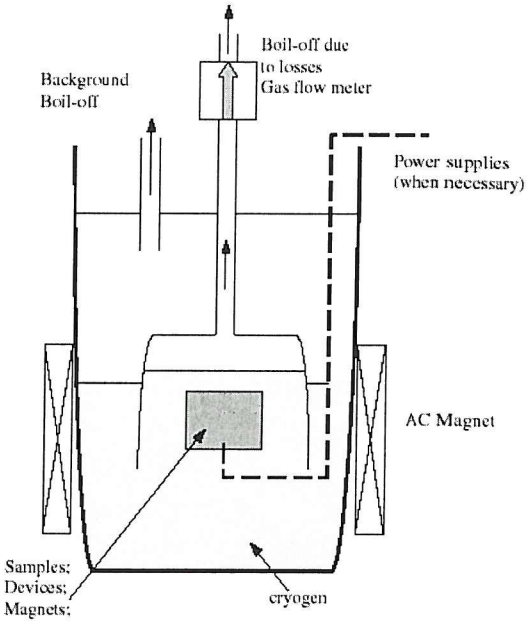

Figure 1.13: Calorimetric measurement of ac-losses via the boil-off rate of the cryogen (from reference [41]).

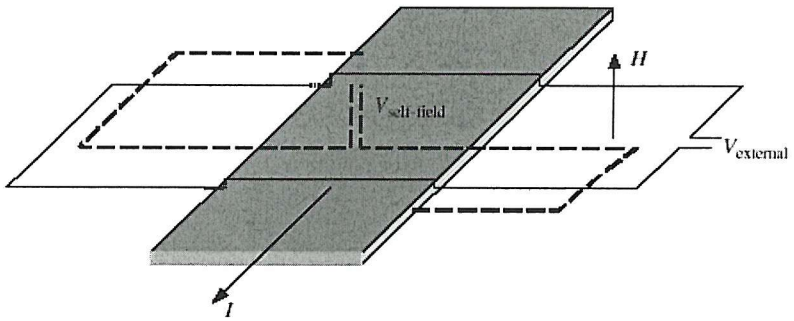

Figure 1.14: Electric measurement of ac-losses due to ac current and external magnetic field (from reference [41]).

There are several electrical measurements that are important for determining hysteresis loss, self-field loss, and coupling loss, as explained in [41]. The arrangement of coils and conductors may vary with the geometry in order to minimize measurement errors. Figure 1.14 shows a circuit for measurement of self-field and external field losses.

The basic idea is to multiply current by voltage electronically and then to integrate the product electronically over one cycle, yielding the energy supplied to the magnet.

Measurements for a tape with twisted superconducting filaments are presented in [40]. Electronic methods for self-field AC losses measurements are used in [7] for Bi-2223 tapes and in [19] for PbBi-2223 tapes.

1.7 Numerical calculation of losses

Analytical formulation for loss calculation presented in section 1.6 were given for simple geometries based on Bean critical state model. This model does not apply satisfactorily for HTS where the $E - J$ characteristic is a power law like function such as $E(J) = E_c(J/J_c)^n$. For ac loss calculation in such case, numerical models representing with accuracy the physical phenomenon produced are required.

The aim of these thesis is to present effective numerical models to give a precise idea of the electric and magnetic field distributions inside the superconductor. In particular the thesis will focus in modelling high-T_c superconductors in external AC-magnetic field.

Integral formulations and finite element method (FEM) are tools commonly used for modelling the general physical problem. Whereas the FEM is required for 3D problems of superconductors with finite dimensions, which are solved with a large numerical effort, integral formulations are a better alternative for modelling 2D problems due to their simplicity.

The 2D problem of infinite long tapes in perpendicular fields where the current has only one component along the conductor is solved with Brandt's formulation, which consists in solving an integral equation for the current density. The implementation of a numerical method to solve Brandt's formulation is explained and validated in chapter 2.

The 3D problem of finite superconductors is solved using a FEM software as it is explained in chapter 4. With this model the coupling phenomenon is well analyzed for strip and slab geometries.

Chapter 5 is dedicated to modelling of infinite slabs and thin discs of finite length. In

this geometries the currents are restricted to a plane and have two components. Therefore a integration formulation can be applied. Similarly to the problem of infinite long tapes, the reduction to a 2D problem results in a integral equation, in this case for the stream function of the induced sheet current. The coupling effect between superconductors via a resistivity matrix is well modelled by using this method.

Chapter 2

2D Modelling of superconducting tapes

2.1 Introduction

When superconductors are exposed to AC magnetic fields, high losses due to hysteresis are produced. In order to predict them it is important to have models to calculate the current and field profiles inside the superconductors.

Calculations of losses in 2D superconductors can be obtained analytically for superconductors in the critical state with simple geometries by knowing the exact field profiles [5]. However, for Hight-T_c superconductors the critical state does not apply successfully since the material is characterized by a non-linear $E - J$ power law such as $E(J) = E_c(J/J_c)^n$ which includes the Bean limit ($n \rightarrow \infty$). Therefore, for modelling of losses in high-T_c superconductors or with more complex geometries numerical methods are required.

Numerical simulations of this 2D problems with a $E - J$ power law have been developed based on the finite element method (FEM) or in an integration formulation. Although FEM finite element method is generally utilized ([3],[18]), because of the high non-linearity, sometimes is not too efficient and requires a large numerical effort. Integration methods as Brandt's method [10] are advantageous due to their simplicity.

Brandt's formulation applied to superconductors with rectangular cross section is presented in the next section. Due to the non-linear behavior of the superconductor

properties, the final differential equation obtained is highly non-linear and stiff. The objective of this work is the implementation of a numerical method to solve Brandt's equation efficiently.

In section 3, Rosenbrock method [17] is presented as an effective method for stiff problems. The performance of the solver RODAS, based on a Rosenbrock method of order 4, is investigated and compared with other implementations.

Finally, current and field profiles obtained using RODAS are shown and commented in section 4 for partial and total penetrated superconductors. Also, it will be analyzed the influence of some parameters as the n-value of the $E - J$ relation and the aspect ratio of the superconductor in the "stiffness".

2.2 Numerical modelling of superconductors in 2D using Brandt's method

In order to study the electromagnetic behavior of a superconductor, Maxwell equations must be solved:

$$\nabla \cdot \mathbf{B} = 0 \tag{2.1}$$

$$\nabla \times \mathbf{H} = \mathbf{J} \tag{2.2}$$

$$\nabla \times \mathbf{E} = -\frac{\partial \mathbf{B}}{\partial t} \tag{2.3}$$

$$\nabla \cdot \mathbf{E} = \rho/\epsilon_0 \tag{2.4}$$

Also, to describe the electromagnetic of the superconductor material requires constitutive law between flux density B and the magnetic field distribution H. It is assumed the material law $B = \mu_0 H$.

Relation between the electric field E and the current density J for Type-II superconductors can be expressed by a highly non-linear power-law as follow:

$$E(J) = E_c(J/J_c)^n \tag{2.5}$$

It has been found that for practical superconductors $\alpha \approx 20$ and therefore the system will be extremely non-linear.

Maxwell equations plus the two laws $B-H$ and $E-J$ are the tool used to calculate the electromagnetic behavior of a superconductor of arbitrary shape when a perpendicular

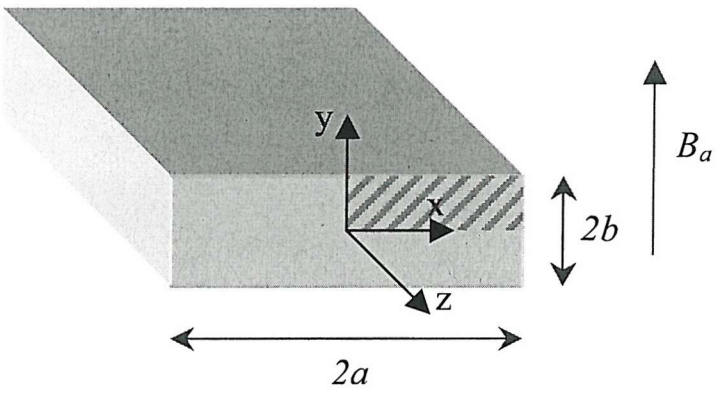

Figure 2.1: Superconductor cross-section model.

arbitrary magnetic field is applied. Since the current is uniform along the tape axis, then a 2D model of the tape cross section can be used.

Different numerical models in 2D have been developed in the last years. In [23] and [20], the problem is solved using a finite differences method. The FEM is utilized in [3] and inserted in commercial software as Flux2D [18]. Brandt proposed a simpler formulation based in an integral equation which is presented and implemented here. Later, Yazawa [43] extended it to include transport current through the superconductor.

2.2.1 Brandt's method

Brandt [10] proposes a 2D model for long superconductors of arbitrary cross-section in perpendicular field which consists on solving the Maxwell equations in an integral form. In that way, it avoids calculating the spatial derivatives and it is not necessary to consider the boundary conditions since the integral equations contain the appropriate differential equations plus the boundary conditions.

The analysis considers a superconductor cross-section placed in the xy-plane and a time dependent applied field B_a in the y direction (figure 2.1). This applied field induces current to flow along the z direction, and this current generates a magnetic field H without z component.

From $\mathbf{B} = \mu_0\mathbf{H}$, where $\mathbf{B} = \nabla \times \mathbf{A}$ is the induction, and $\nabla \times \mathbf{H} = \mathbf{J}$, then

$$\mathbf{J} = \frac{1}{\mu_0}\nabla \times \mathbf{B} = \frac{1}{\mu_0}\nabla \times \nabla \times \mathbf{A} = -\frac{1}{\mu_0}\nabla^2\mathbf{A} \tag{2.6}$$

For a uniform applied field B_a in the y direction the associated vector potential is $\mathbf{A}_a = -xB_a\hat{\mathbf{z}}$ and $\nabla^2 A_a = 0$. Hence (2.6) can be expressed as

$$J = -\frac{1}{\mu_0}\nabla^2 A_j = -\frac{1}{\mu_0}\nabla^2(A - xB_a) \tag{2.7}$$

The solution of previous equation is

$$A(\mathbf{r}) = -\mu_0 \int\int Q(\mathbf{r},\mathbf{r}')J(\mathbf{r}')\,\mathrm{d}r' - xB_a \tag{2.8}$$

with the internal kernel

$$Q(\mathbf{r},\mathbf{r}') = \frac{\ln|\mathbf{r}-\mathbf{r}'|}{2\pi} \tag{2.9}$$

The integral kernel gives information about the geometry of the superconductor, which connects a field point $\mathbf{r} = (x, y)$ and a source point $\mathbf{r}' = (x', y')$.
The relation (2.8) can be inverted as

$$J(\mathbf{r}) = -\frac{1}{\mu_0}\int\int Q^{-1}(\mathbf{r},\mathbf{r}')\,[A(\mathbf{r}') + x'B_a]\;\mathrm{d}r' \tag{2.10}$$

The inverse Kernel Q^{-1} satisfies $\int_S Q^{-1}(\mathbf{r},\mathbf{r}')\,Q(\mathbf{r}',\mathbf{r}'')\mathrm{d}^2r' = \delta(\mathbf{r}-\mathbf{r}'')$

The induction law in the form $E(J) = -\dot{A}$ allows to obtain the equation of movement for J from equation (2.8),

$$E(J(\mathbf{r},t)) = \mu_0 \int\int Q(\mathbf{r},\mathbf{r}')\dot{J}(\mathbf{r}',t)\,\mathrm{d}r' + x\dot{B}_a \tag{2.11}$$

Finally, to solve the time integration ,express $\dot{J}$ as a function of J and $\dot{B}$.

$$\dot{J}(\mathbf{r},t) = \frac{1}{\mu_0}\int\int_S Q^{-1}(\mathbf{r},\mathbf{r}')\left[E(J(\mathbf{r}',t)) - x'\dot{B}_a\right]\mathrm{d}^2r' \tag{2.12}$$

Note that equation (2.12) describes self and mutual inductance of a set of infinite long wires according to Faraday's law: $\mathrm{d}\mathbf{I}/\mathrm{d}t = \mathbf{V}\mathbf{L}^{-1}$

2.2.2 Numerical implementation for superconductors with rectangular cross section

Numerical solution of (2.12) can be demonstrated using the simple case of a rectangular conductor. Consider the model shown in figure 2.1 of a superconductor with rectangular cross section in the xy-plane, width $2a$ and thickness $2b$.

In order to calculate numerically the solution for the final equation, equidistant points discretize the cross section

$$x_i = (i - \frac{1}{2})\frac{a}{N_x} \qquad i = 1..N_x \tag{2.13}$$

$$y_j = (j - \frac{1}{2})\frac{b}{N_y} \qquad j = 1..N_y \tag{2.14}$$

By labelling the lattice points (x_i, y_j) by a indices $k = 1 \ldots N$, being $N = N_x \times N_y$, one can write the equation in a discrete form for $J_k(t) = J(x_i, y_j, t)$ with $k = 1 \ldots N$ as

$$\dot{J}_k(t) = \frac{\triangle S}{\mu_0} \sum_{k'=1}^{N} Q^{-1}_{k,k'}[E(J_{k'}) - x_{k'}\dot{B}_a(t)] \tag{2.15}$$

and the kernel $\mathbf{Q}$ as a matrix $Q_{i,j}$ of $N \times N$ elements.

$$\begin{aligned} Q_{i,j} &= \frac{1}{2\pi} \ln \mid \mathbf{r} - \mathbf{r}' \mid = \frac{1}{2\pi} \ln \left((x_i - x_j)^2 + (y_i - y_j)^2\right)^{\frac{1}{2}} \\ &= \frac{1}{4\pi} \ln((x_i - x_j)^2 + (y_i - y_j)^2)) \end{aligned} \tag{2.16}$$

The kernel diverges at $\mathbf{r} = \mathbf{r}'$. Brandt's proposed that for a grid such that $dx = a/N_x \simeq dy = b/N_y$ a good accuracy is achieved letting $Q_{i,j} = \frac{1}{4\pi} \ln(0.015 dx dy)$.

Since the inverse of $Q_{i,j}$ must satisfy $\int_S Q^{-1}(\mathbf{r} - \mathbf{r}')Q(\mathbf{r} - \mathbf{r}'')\mathrm{d}^2 r = \delta(\mathbf{r}' - \mathbf{r}'')$, then

$$1 = \int\int_S \delta(\mathbf{r}' - \mathbf{r}'')\mathrm{d}^2r'' = \int\int_S \mathrm{d}^2r'' \int_S Q^{-1}(\mathbf{r} - \mathbf{r}')Q(\mathbf{r} - \mathbf{r}'')\mathrm{d}^2r$$
$$= \sum_{j=1}^{n} \Delta S \sum_{k=1}^{n} Q^{-1}_{j,k} Q_{k,j} \Delta S \tag{2.17}$$

Therefore, the right kernell must be calculated as $Q^{*-1}_{i,j} = Q^{-1}_{i,j}\Delta S^{-2}$

As the magnetic field is applied in the y direction, the current J is symmetrical with respect to the x-axis ($J(x,y) = J(x,-y)$) and antisymmetrical respect to the y-axis ($J(-x,y) = -J(x,y)$), hence in (2.15) only a quarter of the total cross section needs to be considered, $0 \leq x \leq a$ and $0 \leq y \leq b$ (shown with diagonal lines in figure 2.1), replacing the kernel by the symmetric kernel

$$Q_{sym}(x,y,x',y') = Q(x,y,x',y') - Q(x,y,-x',y') + Q(x,y,x',-y') - Q(x,y,-x',-y')$$
$$= \frac{1}{4\pi} \ln \frac{((x-x')^2 + (y-y')^2)\,((x-x')^2 + (y+y')^2)}{((x+x')^2 + (y-y')^2)\,((x+x')^2 + (y+y')^2)} \tag{2.18}$$

Finally, replacing in (2.15)

$$\dot{J}_k(t) = \frac{\triangle S}{\mu_0} \sum_{k'=1}^{N} Q^{-1}_{k,k'} [E(J_{k'}) - x_{k'} \dot{B}_a(t)]$$
$$= \frac{\triangle S^{-1}}{\mu_0} \sum_{k'=1}^{N} Q^{-1}_{sym_{k,k'}} [E(J_{k'}) - x_{k'} \dot{B}_a(t)] \tag{2.19}$$

Equation (2.15) can be expressed in matrix form

$$\dot{\mathbf{J}}(\mathbf{r},t) = \frac{1}{\mu_0 \triangle S} \mathbf{Q}^{-1} \left[\mathbf{E}(\mathbf{J}) - \dot{B}_a(t) x \right] \tag{2.20}$$

Inserting in (2.20) the expression for an applied field sinusoidal, $B(t) = B_a \sin(\omega t)$,

$$\dot{\mathbf{J}}(\mathbf{r},t) = \frac{1}{\mu_0 \triangle S} \mathbf{Q}^{-1} \left[E_c \left(\frac{\mathbf{J}}{J_c} \right)^n - x B_a \omega \cos(\omega t) \right] \tag{2.21}$$

Taking $M = Q\mu_0 \triangle S$ then

$$\mathbf{M}\dot{\mathbf{J}} = E_c \left(\frac{\mathbf{J}}{J_c}\right)^n - xB_a\omega\cos(\omega t) = \mathbf{f}(\mathbf{J}, t) \tag{2.22}$$

2.2.3 Singularity and refinement

Since Brandt's method requires a grid with square cells, it is necessary a very thin mesh. In order to get an accurate Q without a very refined mesh it is possible to consider bigger cells, which are also divided in square subcells as it is explained in [42].

The analytical expression is

$$Q_{i,j} = \int\int_{S_i} \mathrm{d}x_i \mathrm{d}y_i \int\int_{S_j} \frac{\ln((x_i - x_j) + (y_i - y_j))}{4\pi} \mathrm{d}x_j \mathrm{d}y_j \tag{2.23}$$

This allows us to consider the shape factor of each cell at the same time as the singularities are avoid.

Equation (2.23) can be approximated by

$$Q_{i,j} = \sum_{n=1}^{N_s} \sum_{m=1}^{N_s} Q(\mathbf{r}_i - \mathbf{dr}_m, \mathbf{r}_j - \mathbf{dr}_n) \tag{2.24}$$

where N_s is the number of subcells and $\mathbf{dr}_m$ and $\mathbf{dr}_n$ the coordinates of the subcells relative to the cells coordinates.

2.3 Numerical solution method

Equation (2.22) can be formulated as a general initial value problem of the form

$$\mathbf{M}\dot{\mathbf{J}} = \mathbf{f}(\mathbf{J}, t)\,, \qquad \mathbf{J}(t_0) = \mathbf{y}_0$$

In order to solve it, in principle any numerical method could be applied. However, the efficiency of every method varies depending of the characteristics of the ODE to solve. It is therefore necessary to know which type of problem we are dealing with and then apply the appropriate method.

In this section it will be shown that due to the high non-linearity, equation (2.22) belongs to a group of ODEs named "stiff" for which it is known explicit methods are not

efficient. Therefore a implicit scheme has to be used. In particular, Rosenbrock method will be presented as a effective method to solve the stiff problem studied here.

2.3.1 "Stiff" problem

Although there is a general intuitive meaning, there is not a precise definition of "stiffness". In general, an ODE system is called a stiff ODE system when explicit methods can not solve them.

For high applied fields such that the superconductor is saturated, the problem becomes more stiff and difficult to solve. The expected current and field profiles in such case for an infinite slab given by Bean's critical state model are shown in figure 2.2. When the magnetic field applied parallel to the slab is increased, it starts to penetrate in the superconductor and the current has two possible values: J_c in the penetrated region and zero in the rest. When the field raises to H_p the conductor is fully penetrated and therefore the current flows over the whole cross section. If the applied field continues increasing also the total field in the superconductor increases, whereas the current remains equal.

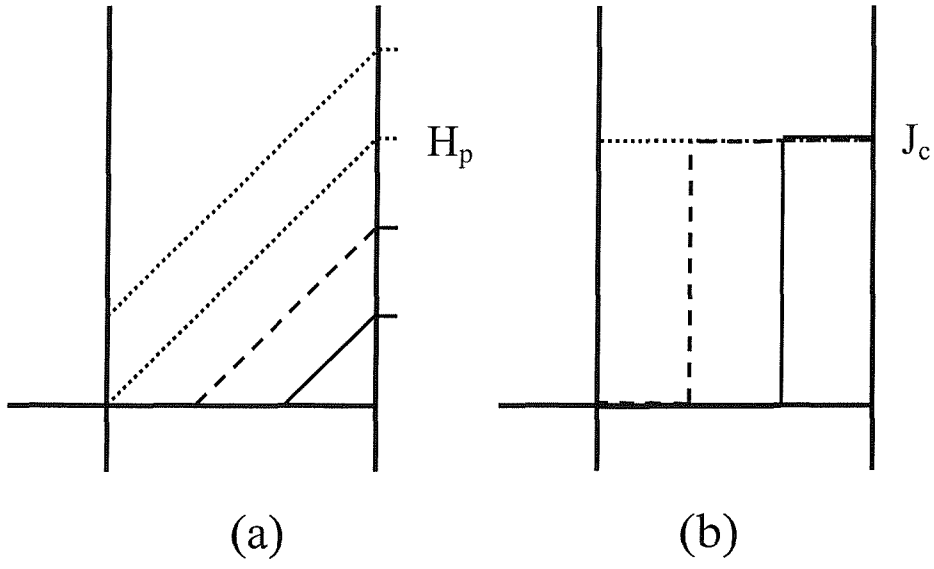

Figure 2.2: Internal magnetic field (a) and current density (b) for Bean's model.

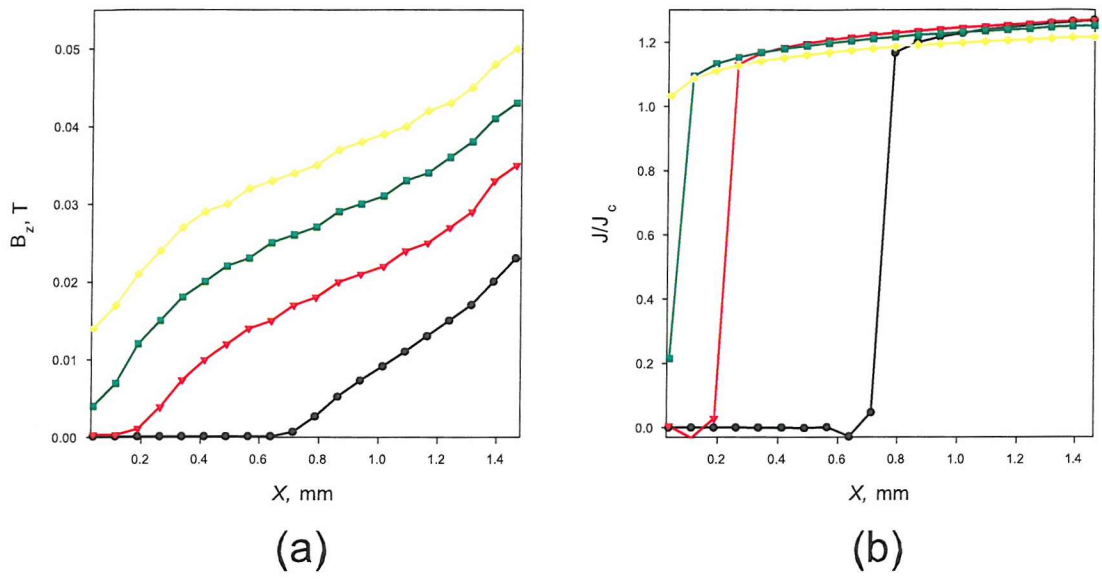

Figure 2.3: Profile of the current (a) and the magnetic field (b) inside a rectangular superconductor in an applied field $B = 0.5\, sin(2\pi 50t)$.

The solution of Brandt's equation presents a similar behavior as it is shown in Figure 2.3. The example is for a superconductor with rectangular cross section ($2a = 3 \cdot 10^{-3}$ m and $2b = 10^{-4}$ m) in a applied field $B = 0.04 \sin(2\pi 50t)$. The $E - J$ relation is given by $n = 21$, resulting in a very non-linear equation. Similarly to Bean's model observe the almost invariant profile of J ($\dot{J} \approx 0$) after the field has completely penetrated the superconductor.

To show the effects of "stiffness" let's apply an explicit method to a particular superconductor example. Consider a superconductor with rectangular cross section ($2a = 3 \cdot 10^{-3}$ m and $2b = 10^{-4}$ m), in an applied field $B = 0.01 \sin(2\pi 50t)$. For the $E - J$ relation the exponent is $n = 21$. Then equation (2.22) results

$$\mathbf{M}\dot{\mathbf{J}} = 10^{-4} \left(\frac{\mathbf{J}}{2 \cdot 10^8} \right)^{21} - 0.1 \cdot 50 \cos(50t) x \tag{2.25}$$

First, the equation was solved using a simple step-forward integration method as it was done in [10]. From an initial condition $J(\mathbf{r}, t_0)$ the evolution of the current it is calculated in successive time steps as $J_{n+1} = J_n + h \cdot \frac{\partial J}{\partial t}(\mathbf{r}, t_{n-1})$ where h is the distance between consecutive steps. To obtain the convergence during a complete cycle time of

N	Tol	Steps	Rejected steps	Accepted steps	Aver. time step size
15	10^{-4}	19678	148	19531	5.20×10^{-7}
15	10^{-6}	19412	16	19396	5.18×10^{-7}
20	10^{-4}	35441	447	34994	2.9×10^{-7}
20	10^{-6}	34613	12	34610	2.9×10^{-7}
25	10^{-4}	57719	2631	55088	1.8×10^{-7}

Table 2.1: Results for (2.25) using DOPRI5 for $0 \leq t \leq 0.0005$.

the applied field, the maximum step size possible was found $h = 3 \cdot 10^{-9}$. This means that the solution converged extremely slow, a lot of steps were required and therefore the method became impractical.

In contrast to the simple step-forward integration, lets try now with another explicit method this time with step size control, in order to avoid the extremely slow convergence. The method chosen is the solver DOPRI5, a explicit Runge-Kutta method of order (4)5 due to Dormand & Prince and implemented by E. Hairer and G. Wanner [16]. We integrated during the first quarter of the cycle time $0 \leq t \leq 1/4f$ using the same value for the relative and absolute tolerances $Rtol = Atol = Tol$. Table 2.1 shows the results for different tolerances and grid points. Observe that the number of steps used increases with the grid points due to stability reasons required for thinner meshes. Notice that the time step size is independent of the tolerance, in fact for smaller Tol the number of steps required is bigger, which means that the interval selection is regulated in order to control the stability more than the precision. Since the problem is very stiff and the method is not stiff accurate then the time step size has to be reduced to 10^{-7} which is still a very slow convergence.

The solver DOPRI5 includes a process to detect stiffness based in the observation that where a non-stiff code finds stiffness the product of the step size with the dominant eigenvalue of the Jacobian lies near the border of the stability domain of the method. This mechanism is useful in order to say when a method is not suitable and a implicit scheme is required. Figure 2.4 shows $h\lambda/3.25$ where h is the time step, λ is the estimated eigenvalue and 3.25 is the approximate distance of the frontier of the stability domain to the origin. Observe that the value of $h\lambda$ is approximately 3.25 for almost the whole interval of integration, and exactly 3.25 when the step size reaches the minimum values restricted by stability. Notice that the step size starts to increase just before the applied field reaches the peak, and decreases again after the peak field. Observe that setting a

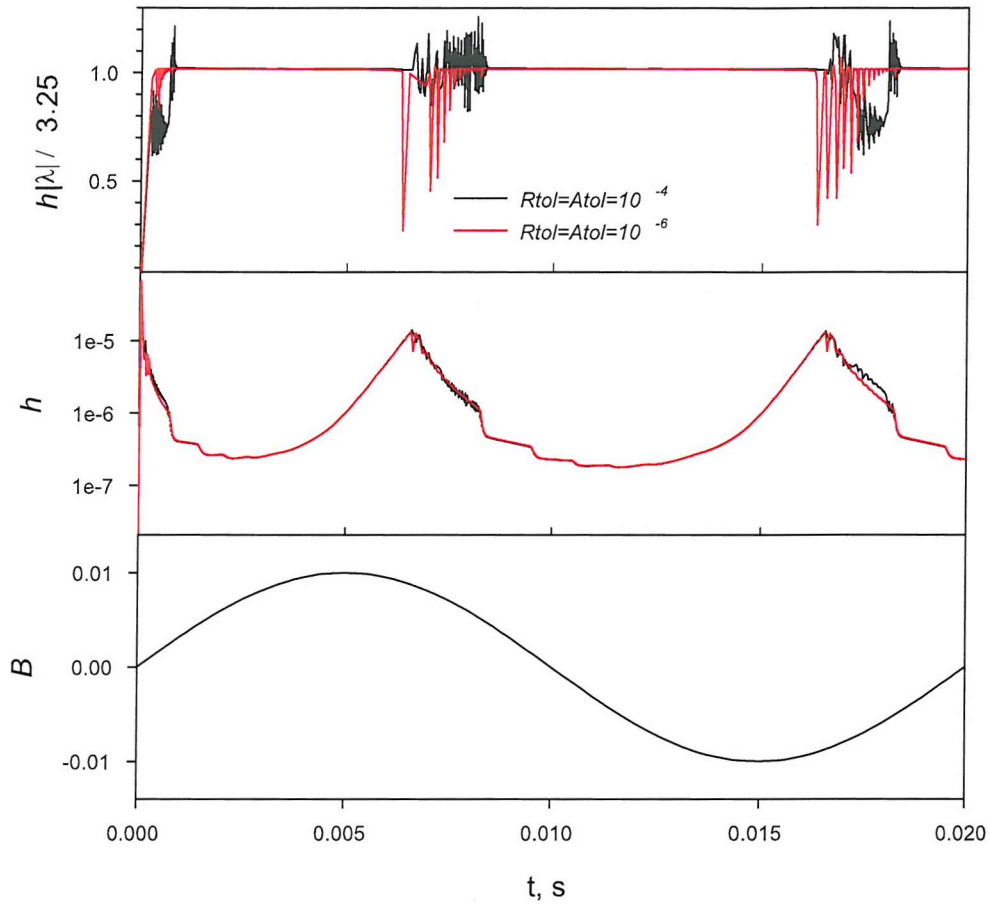

Figure 2.4: Stiffness detection with DOPRI5.

smaller tolerance improves the stability but the step size does not change significantly.

As it was said before, the problem becomes more stiff as the amplitude of the applied field is higher and the superconductor is saturated. Table 2.2 shows the step size required solving the equation when the applied field amplitude is $B_a = 0.5\,\mathrm{T}$. Notice the high increment of the number of steps required comparing with results in table 2.1.

2.3.2 Numerical methods for Stiff ODEs

Solvers for ODE systems include Runge-Kutta methods and multisteps methods [17]. Among the Runge-Kutta there are explicit and implicit methods. As it was shown in previous section explicit schemes have the advantage of being easier to implement but

N	Tol	Steps	Rejected steps	Accepted steps	Aver. time step size
15	10^{-4}	471400	44	471356	4.257×10^{-8}
15	10^{-6}	469537	13	469524	4.26×10^{-8}

Table 2.2: Results for (2.25) with $B_a = 0.5$ using DOPRI5 for $0 \leq t \leq 0.005$.

poor stability properties which leads to very strict restrictions on the time step chosen. Implicit schemes have the advantage of being efficient but require much numerical effort and therefore being more suitable for small matrices. However there is a group of "semi-implicit" methods named Rosenbrock methods [17], which give good responses and do not need such computational effort. Since they are not implicit they are simpler to understand and to implement. This methods have been tested in many physical problems as in [27], [35], [31], [30] where they were found to be efficient in terms of stability and computational time. Also, Rosenbrock methods are inserted in well-known calculation software like Mathcad or Matlab as stiff solvers.

Next sections will describe the Rosenbrock method and later numerical results will be presented showing its performance in solving the ODE obtained with Brandt't formulation.

2.3.3 Rosenbrock method

For an implicit non-autonomous differential equation $\mathbf{M}\dot{\mathbf{y}} = \mathbf{f}(\mathbf{y}, x)$,the solution found by an s-stage Rosenbrock method is given by

$$\mathbf{y_1} = \mathbf{y_0} + \sum_{i=1}^{s} b_i \mathbf{k}_i \tag{2.26}$$

where $\mathbf{k}_i$ are calculated solving s linear equations

$$\begin{aligned} \mathbf{M}\mathbf{k}_i = {} & h\mathbf{f}(x_0 + \alpha_i h, \mathbf{y_0} + \sum_{j=1}^{i-1} \alpha_{i,j}\mathbf{k}_j) + \gamma_i \sum_i h^2 \mathbf{f'}_x(x_0, \mathbf{y_0}) \\ & + h\mathbf{J}(x_0, \mathbf{y_0}) \sum_{j=1}^{i} \gamma_{i,j}\mathbf{k}_j \qquad i = 1, \ldots s \end{aligned} \tag{2.27}$$

where $\mathbf{J} = \frac{\partial \mathbf{f}}{\partial y}$ is the Jacobian and $\mathbf{f'}_x = \frac{\partial \mathbf{f}}{\partial x}$.

The coefficients α_i, γ_i, are given by

$$\alpha_i = \sum_{j=1}^{i-1} \alpha_{i,j} \qquad \gamma_i = \sum_{j=1}^{i} \gamma_{i,j}$$

α_{ij}, γ_{ij} and b_i are fixed constants problem independents. They are chosen in order to satisfy the stability and order conditions. The method is of order p if the local error satisfies $\mathbf{y}(x_0 + h) - \mathbf{y_1} = O(h^{p+1})$.

To reduce the number of matrix-vector multiplications required each time step, the equation can be transformed. Taking

$$u_i = \sum_{j=1}^{i} \alpha_{i,j} \qquad \gamma_i = \sum_{j=1}^{i} \gamma_{i,j}\mathbf{K_j} \qquad i = 1 \ldots s$$
$$(a_{ij}) = (\alpha_{ij})(\gamma_{ij})^{-1}$$
$$(m_1 \ldots\ldots m_s) = (b_1 \ldots\ldots b_s) \cdot (\gamma_{i,j})^{-1}$$
$$(C_{ij}) = diag(\gamma_{11}^{-1} \ldots\ldots \gamma_{ss}^{-1}) - (\gamma_{ij})^{-1}$$

Then the equations become

$$\left(\frac{1}{h\gamma_{ii}}\mathbf{M} - \mathbf{J}(x_0, \mathbf{y}_0)\right)\mathbf{u}_i = \mathbf{f}(x_0 + \alpha_i h, \mathbf{y_0} + \sum_{j=1}^{i-1} a_{i,j}\mathbf{u_j}) + \gamma_i h \mathbf{f}'_x(x_0, \mathbf{y}_0) \qquad (2.28)$$
$$+ \mathbf{M}\sum_{j=1}^{i-1} \frac{C_{ij}}{h}\mathbf{u}_j \qquad i = 1 \ldots s$$
$$\mathbf{y}(x_0 + h) = \mathbf{y}_0 + \sum_{i=1}^{s} m_i \mathbf{u}_i \qquad (2.29)$$

2.3.4 Implementation of Rosenbrock formulas

Since stiffness appears in many physical problems, typical mathematical calculation softwares as Mathcad or Matlab have built-in functions for numerically solving ODEs with accuracy for stiff systems. Among the stiff solvers Mathcad has a function using Rosenbrock method called STIFFR. To call this function requires as input arguments an n-

element vector-valued function containing the first derivatives of the unknown functions and a function which returns the n by $(n+1)$ matrix whose first column contains derivatives and whose remaining rows and columns form the Jacobian matrix for the system of differential equations. A disadvantage of this implementation is that the differential equation can not be solved in implicit form. Therefore Brandt equation is expressed as in (2.21), it is necessary the inversion of the kernel Q, and the Jacobian becomes a full matrix.

Matlab has a built-in solver for stiff problems based on a Rosenbrock method, ODE23S, a modified Rosenbrock formula of order 2. Although this function has an option for solving the equations in implicit form, is formulated in a low order 2, only suitable for stiff problem where lower accuracy is acceptable.

In order to avoid the disadvantages of the implementations in both softwares, a more efficient solver found from literature, RODAS, was inserted in our own library to solve Brandt's equations.

2.3.4.1 ODE solver RODAS

RODAS of Hairer and Wanner [17] is the code in Fortran of a Rosenbrock method with $s = 6$ of order 4. It takes the parameter $\gamma_{ii} = \gamma$ for all i given in equation (2.27) so only one factorization has to be done each time step. The constant coefficients required in the formulas are chosen in order to obtain a stiffly accurate and A-stable method.

For the error estimation and the step size prediction it uses the embedded third order solution. Then two solutions of the form (2.29) are computed, the one of order 4 (2.29), and a lower order estimation $\hat{y}$ with other coefficients $\hat{b_i}$,

$$\hat{\mathbf{y}} = \mathbf{y_0} + \sum_{i=1}^{s} \hat{b_i} \mathbf{k}_i \tag{2.30}$$

The calculation of the embedded solution does not require extra cost since it uses the same coefficient $\mathbf{k_i}$ calculated for the four order solution. The only difference are the fixed coefficients $\hat{b_i}$ which are chosen such that both methods are stiffly accurate and the embedded solution is third order.

Then the error formula using both solutions is

$$err = \sqrt{\sum_{i=1}^{n} \frac{1}{n}(\frac{\mathbf{y} - \hat{\mathbf{y}}}{sk_i})} \tag{2.31}$$

with

$$sk_i = Atol + Rtol \max\left(|\mathbf{y_i}|, |\mathbf{y_{0_i}}|\right) \tag{2.32}$$

Atol and *Rtol* denote the relative and absolute error tolerances. Normal values are $Atol = Rtol = 10^{-5}$

If $err > 1$ the step is rejected, then a new step size h is calculated as

$$h_{new} = h/fac \tag{2.33}$$

and the solution is recomputed in the same point. The parameter fac is obtained as

$$fac = \max\left\{fac2, \min\left(fac1, \sqrt[4]{err}\right)\right\} \tag{2.34}$$

with $fac1$ and $fac2$ defined such that

$$fac2 \leq h/h_{new} \leq fac1 \tag{2.35}$$

If the step is accepted, $err < 1$, the process continues with a new size time step. In this case, it will be calculated by the Predictive controller of Gustafsson,

$$fac_{gus} = \max\left\{fac2, \min\left\{fac1, \frac{h_{n-1}}{h_1}\sqrt[4]{\frac{err_{n+1}^2}{err_n}}\right\}\right\} \tag{2.36}$$

and

$$h_{new} = h/max(fac, fac_{gus}) \tag{2.37}$$

If the dimension of the system is large, the computational cost is high because at each time step it is required: an evaluation of the Jacobian and the derivative, 6 matrix-vector multiplications, 6 function evaluations, and 6 linear system solutions.

Most of the computing time is spending for solving the linear systems specially for the factorization of the matrix $\left(\frac{1}{h\gamma}\mathbf{M} - \mathbf{J}\right)$ once per step. For this task the routine LIN-SOL-SELF was inserted in the solver RODAS.

LIN-SOL-SELF is a routine of the *IMSL Fortran 90 MP Library*. It solves a system of linear equations $\mathbf{Ax} = \mathbf{b}$, where $\mathbf{A}$ is self-adjoint matrix. It needs the whole matrix instead to use the advantage of a symmetric matrix. The routine computes the factorization of $\mathbf{A}$ using Aasen's method.

Usual techniques to reduce the computational cost for the linear algebra were tried : to approximate several steps with the same jacobian, or to use the sparsity of the matrix. Despite the jacobian is a diagonal matrix, changes considerably each time step. Also, the matrix $\mathbf{M}$ is full so none of the solutions proposed have given good results.

2.3.4.2 Performance of the code

A more efficient code is possible tuning the parameters $fac1$ and $fac2$ used to calculate the new step size (formulas (2.34),(2.36)). Depending on their value, the step size computed and the number of rejected steps vary and therefore the computing time. Some results are displayed in Table 2.3 and Table 2.4 obtained solving the problem in a grid 20×20 for $B_a = 0.1$ T. Observe that reducing the tolerance to 10^{-5}, the number of steps increases. As $fac2$ is chosen close to 1 and $fac1$ not very "small" ($\simeq 5$) then the step size does not change often and the number of rejected steps decreases considerably. That is a good strategy to reduce computational time as far as the approximately constant h is not very small, otherwise would take a lot more number of steps.

	Total steps	**Rejected steps**	**Accepted steps**
$fac1 = 5, fac2 = 0.9$	1265	187	1078
$fac1 = 5, fac2 = 0.2$	Impossible to solve		
$fac1 = 5, fac2 = 0.99$	1590	50	1540
$fac1 = 7, fac2 = 0.9$	1261	185	1076
$fac1 = 9, fac2 = 0.9$	1261	185	1076

Table 2.3: Results for $Rtol = Atol = 10^{-4}$.

	Total steps	Rejected steps	Accepted steps
$facl = 5, fac2 = 0.2$	1888	446	1442
$facl = 5, fac2 = 0.9$	2049	331	1718
$facl = 2, fac2 = 0.9$	2060	351	1609
$facl = 2, fac2 = 0.5$	1950	548	1402
$facl = 2, fac2 = 0.2$	1950	548	1402

Table 2.4: Results for $Rtol = Atol = 10^{-5}$.

Observe in table 2.5 the results obtained for different values of the tolerance. A difference with the explicit method presented in previous section, the number of steps increases with the tolerance in order to control the precision required. Figure 2.5 shows the solution at some grids points during the total cycle time. Notice how the time step size is relaxed at some time intervals, which are the intervals where the current J has a constant value. The minimum size of time step taken was $\approx 2 \cdot 10^{-6}$ whereas for the same problem with the direct integration and with the explicit Runge-Kutta the step size was found $\approx 10^3$ and 10^1 times smaller respectively.

	Total steps	Rejected steps	Accepted steps	Time (s)
$Rtol = 10^{-4}$	1074	50	1024	37.5
$Rtol = 10^{-5}$	1840	106	1734	63.14
$Rtol = 10^{-6}$	2793	145	2648	97.56
$Rtol = 10^{-8}$	8788	365	8423	303

Table 2.5: Results for different values of $Rtol$.

To compare the performance of RODAS and the solver STIFFR of Mathcad software some results are presented in table 2.6 for partial penetration ($B_a = 0.01\,\mathrm{T}$) and total

	Stiffr	Rodas
$B_a = 0.01\mathrm{T}$	2280	1013
$B_a = 0.04\mathrm{T}$	4930	2360

Table 2.6: Time in seconds for solving a complete cycle of the applied field.

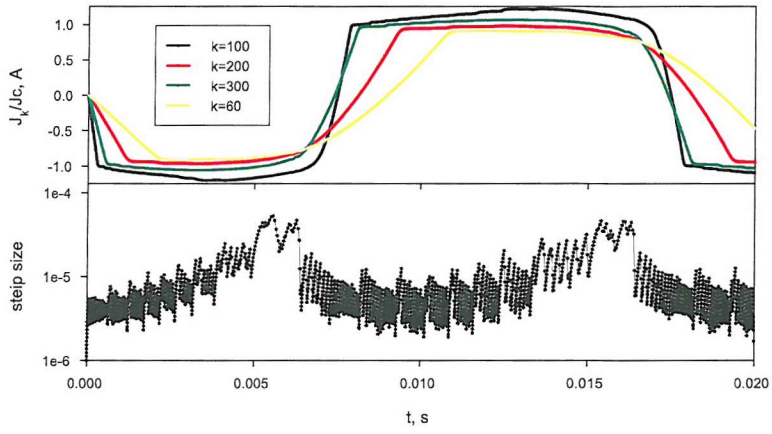

Figure 2.5: Solution for some components of the current and step sizes calculated by Rosenbrock method each time step.

penetration ($B_a = 0.04\,\mathrm{T}$) of the superconductor. Although both solvers produced similar approximations of the solution as it is observed in figure 2.6, the computational time required is about double using Mathcad in both cases. Apart from possible differences due to the compiler dependence, the higher computational time for STIFFR is probably due to the fact that STIFFR cannot solve ODEs in implicit form and therefore increasing the linear algebra costs.

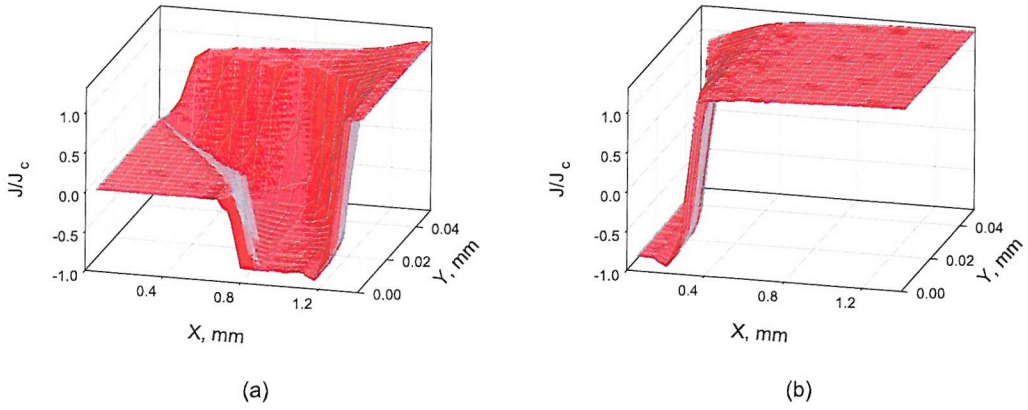

Figure 2.6: Profiles of the current density at $\omega t = 2\pi$ in applied fields with amplitudes $B_a = 0.01\,\mathrm{T}$ (a) and $B_a = 0.04\,\mathrm{T}$ (b) calculated with STIFFR (red) and RODAS (gray).

2.4 Results, comments and comparisons

In this section numerical results computed solving equation (2.22) with Rosenbrock solver RODAS will be shown.

From the solution for J, the magnetic field components B_x and B_y were rapidly calculated as spatial derivatives of A, which is obtained by equation (2.8).

All the results presented are for superconductors with rectangular cross sections in an applied magnetic field $B = B_0 sin(2\pi ft)$ with the frequency $f = 50$Hz. The critical current density is assumed to be $J_c = 2 \cdot 10^8 \mathrm{Am}^{-2}$.

Results will be shown only for a quarter of the total rectangular cross-section $[0, a] \times [0, b]$ in a grid of 20×20 points.

In figures 2.7, 2.8 current and magnetic field profiles are presented for superconductors of width $2a = 0.003\,\mathrm{m}$ and length $2b = 0.0001\,\mathrm{m}$. The exponent of the $E - J$ power law was set $n = 21$. Four situations from the cycle time were selected to show the results: when the applied field reaches the positive and negative peaks ($\omega t = \pi/2$ and $\omega t = (3/2)\pi$) and when the field returns to zero after the peaks ($\omega t = \pi$ and $\omega t = 2\pi$).

Partial penetration is observed in figure 2.7 for a magnetic field amplitude $B_0 = 0.01$T. The field does not fill the total cross section. At the peak of the applied field, (figure 2.7.(a)), the central part is current free and $J \approx J_c$ in the rest. When the applied field is removed, currents still remain trapped, there is current reversing in the outer zone as it is seen in figure 2.7.(b). The same evolution of the field and the current are observed as the field decreases to a negative peak field and returns to the initial value (figures 2.7.(c),2.7.(d)) to complete the field cycle. Notice that there is a similar situation to Bean critical state model along the thickness with total penetration in the outer parts and partial penetration in the interior. A difference with the concentric contours of the current for rectangular conductors described in [25], it is observed here that the lines separating the zones of different values of the current form contours which meet at $y = b$ and $x = 0$.

At larger amplitudes a slightly different situation is obtained. For $B_0 = 0.04\,\mathrm{T}$ (figure 2.8) the field soon penetrates the total cross section and continues increasing over the whole superconductor with the same pattern until it reaches the maximum value at $\omega t = \pi/2$. There is not a current-free zone and J is almost equal to J_c in the whole superconductor (figure 2.8.(a)). When the applied field is decreased, current in

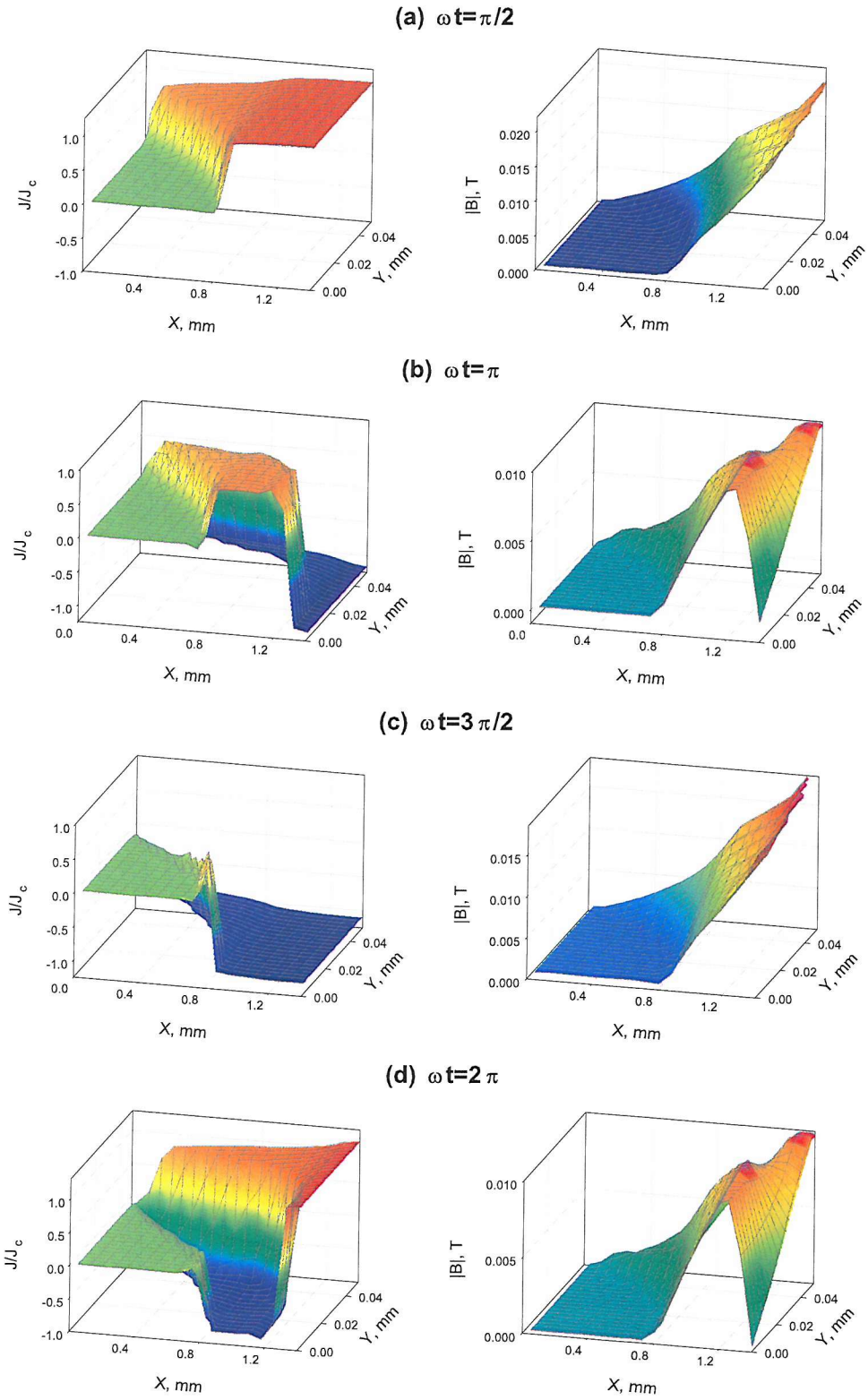

Figure 2.7: Current and field profiles for $B_a = 0.01\,\mathrm{T}$.

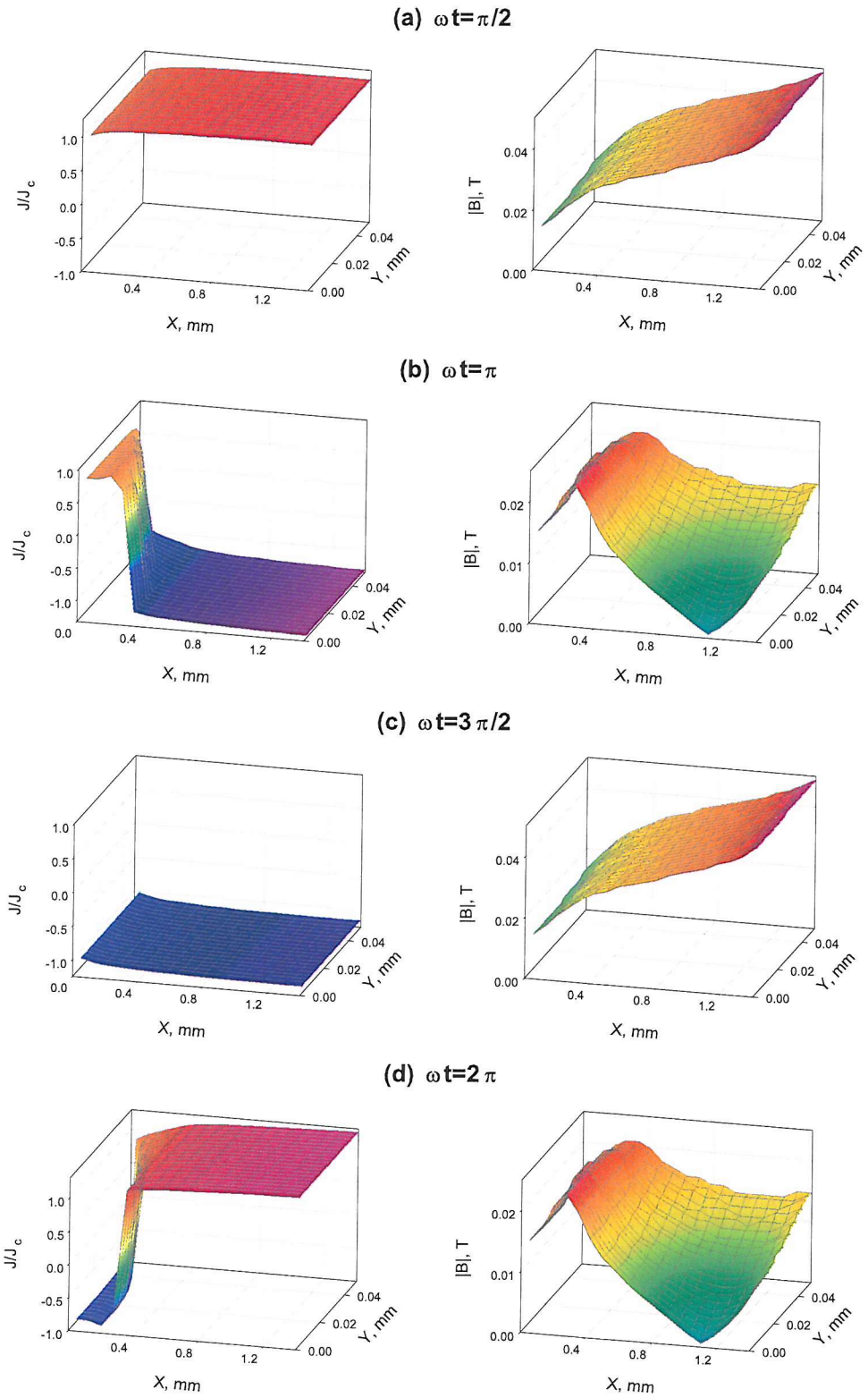

Figure 2.8: Current and field profiles for $B_a = 0.04\,\mathrm{T}$.

		$\mathbf{B_a} = 0.01\,\mathrm{T}$	$\mathbf{B_a} = 0.04\,\mathrm{T}$
$\mathbf{Tol} = 10^{-4}$	**Steps**	2686	6501
	Rejected steps	158	367
	Time (s)	659.3	1585.91
$\mathbf{Tol} = 10^{-5}$	**Steps**	3703	8703
	Rejected steps	210	453
	Time (s)	921	2090.4
$\mathbf{Tol} = 10^{-6}$	**Steps**	5624	13017
	Rejected steps	266	588
	Time (s)	1379.7	3321.5

Table 2.7: Results using RODAS for $0 \leq t \leq 0.02$.

opposite direction appears in the outer part then J changes abruptly from J_c to $-J_c$ (figure 2.8.(b)). Similar profiles are found as the field decreases to the negative peak and returns to zero (figures 2.8.(c) and 2.8.(d)).

Respect to the performance of RODAS (figure 2.9), it is observed for both, low and high B_a, that the step sizes become higher as the superconductors become more penetrated, remaining at the same level beyond full penetration field, and, as the applied field has been decreased smaller steps sizes are required (figure 2.9.(a) and (c)). The average step size used for solving the total penetration case is smaller in comparison with partial penetration. Therefore for $B_a = 0.04\,\mathrm{T}$ the method needs a higher number of steps, approximately double than that for $B_a = 0.01\,\mathrm{T}$, to complete the cycle time as it is indicated in table 2.7. Also notice that the number of steps increases with reducing the tolerance as it is expected for a stable solver.

Compared to DOPRI5 method (figure 2.9.(b)), the step sizes for RODAS vary less along the whole cycle time. The average step size is about 10 times higher for RODAS during the whole cycle time. Observe that during the first quarter both methods show a different behavior. Whereas the step size becomes higher with increasing the field for RODAS, for DOPRI5 the step size starts decreasing. Since we saw in figure 2.4 that the differential equation is very stiff during the first quarter, we can say that the step size required by RODAS is no restricted by stiffnes, but probably decreases due to the sharp changes in the current density profiles from 1 to -1 as the field starts to decrease.

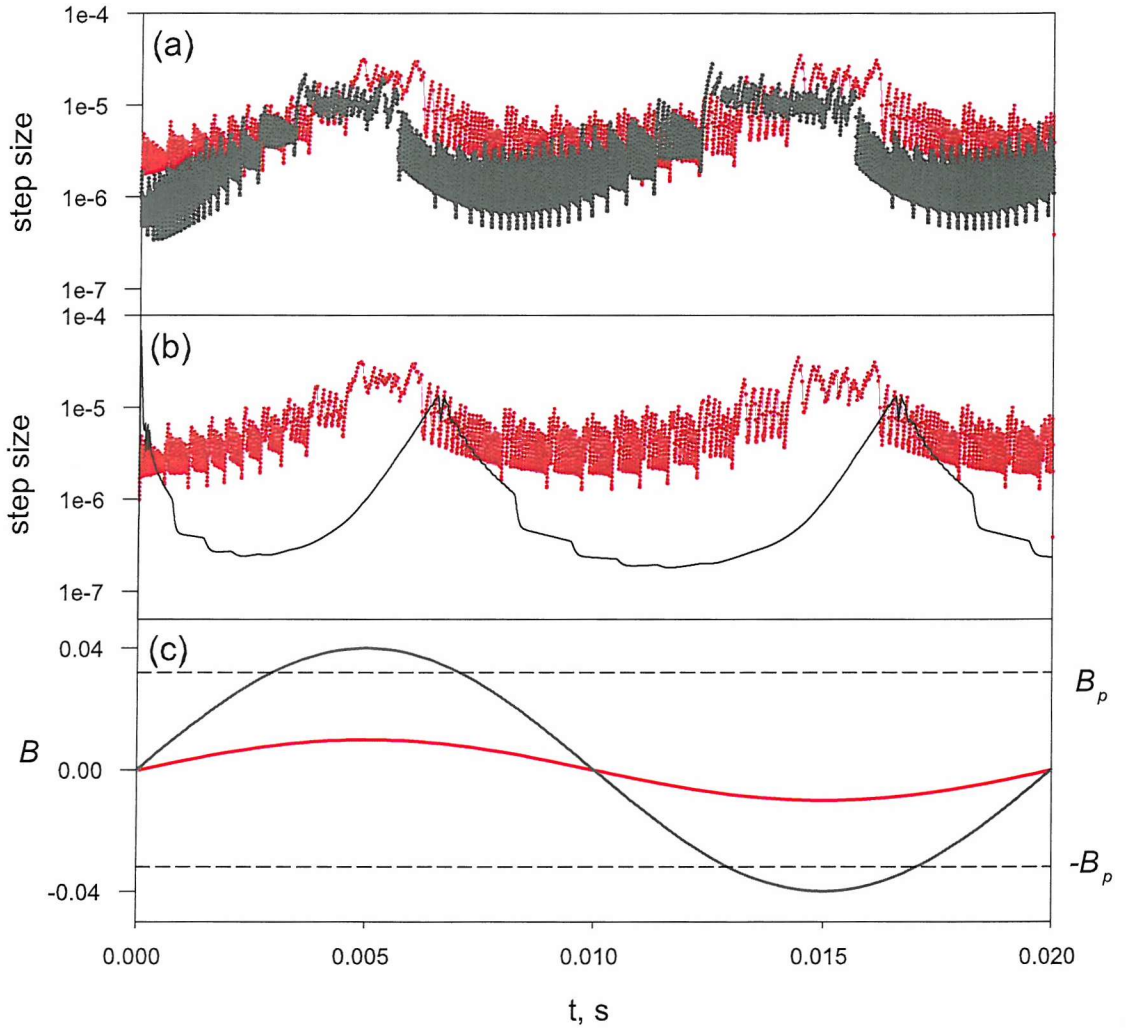

Figure 2.9: Step size required for RODAS with $Tol = 10^{-6}$ in an applied field $B_a = 0.01\,\mathrm{T}$ (red) and $B_a = 0.04\,\mathrm{T}$ (grey) (a). Comparison between RODAS (red) and DOPRI5 (black) for $B_a = 0.01\,\mathrm{T}$ is shown in (b). Applied sinusoidal magnetic field with amplitude $B_a = 0.01\,\mathrm{T}$ (red) and $B_a = 0.04\,\mathrm{T}$ (grey) (c).

2.4.1 Results for different n-values of the $E - J$ power law.

Since the non-linearity affects to the stiffness of the problem, it is interesting to calculate some results for different n-values in the $E - J$ law (figure 2.10) in order to show the differences in the current and field distributions and the performance of the code.

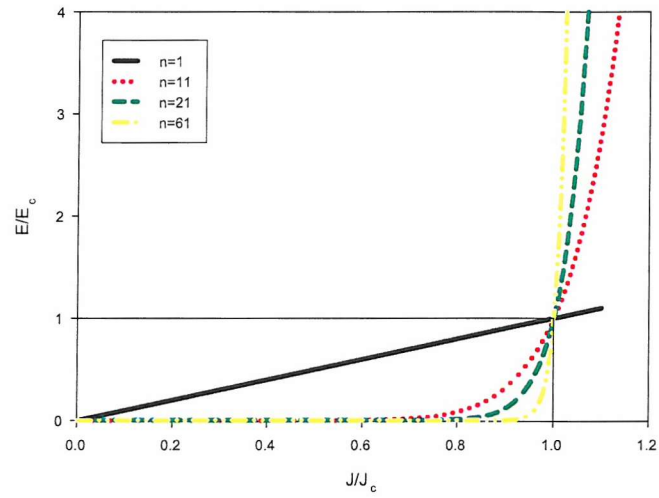

Figure 2.10: $E - J$ power law for different n-values.

Figure 2.11 shows the current and field profiles obtained for $n = 5$, 21, and 61. Observe the profile of the current density when $n = 5$ (figure 2.11.(a)). It reaches the maximum value in the zone close to the edges where is $\approx 1.48 J_c$, and decreases smoothly to zero towards the current-free region. When $n = 21$ (figure 2.11.(b)), the maximum value of J is slightly over J_c ($J \approx 1.1 J_c$). And for $n = 61$ (figure 2.11.(c)) $J = J_c$ in the penetrated part and $J = 0$ in the non-penetrated region with a sharp change to pass for one value to the other similarly to Bean's model which is the case when $n = \infty$. Observe in the field profiles the dependence of the penetration depth on n.

Computational results are seen in table 2.8 and in figure 2.12. As it is expected for problems very "stiff", $n = 61$, the number of rejected steps increases significantly since the time step sizes required during the integration have to be small in order to keep stability (figure 2.12.(c)). The average time step size is 1.1×10^{-5} for $n = 5$, about double of the value 5×10^{-6} when $n = 21$ and about four times the average size

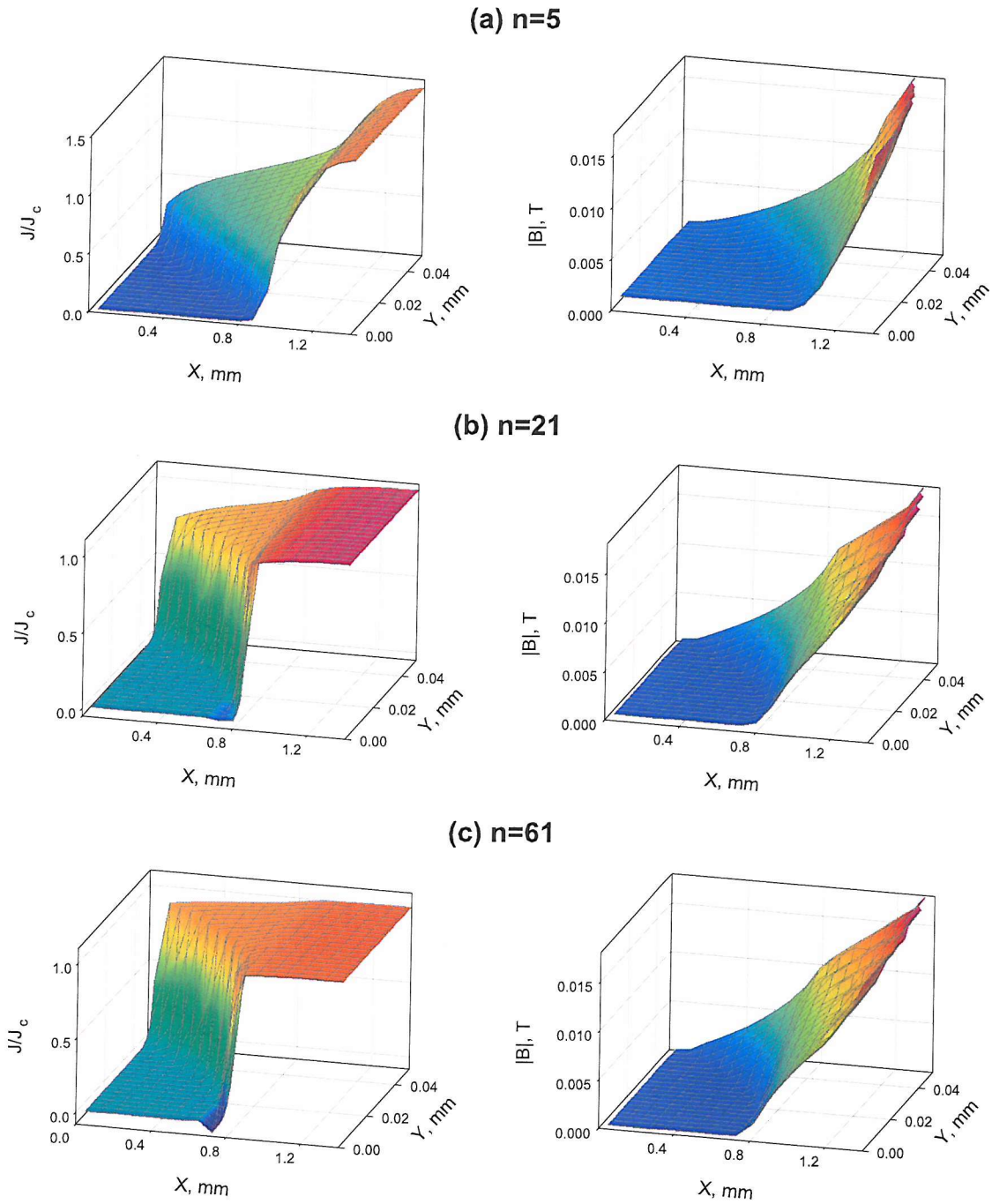

Figure 2.11: Current density and field profiles at $\omega t = \pi/2$ for $n = 5$ (a), $n = 21$ (b) and $n = 61$ (c).

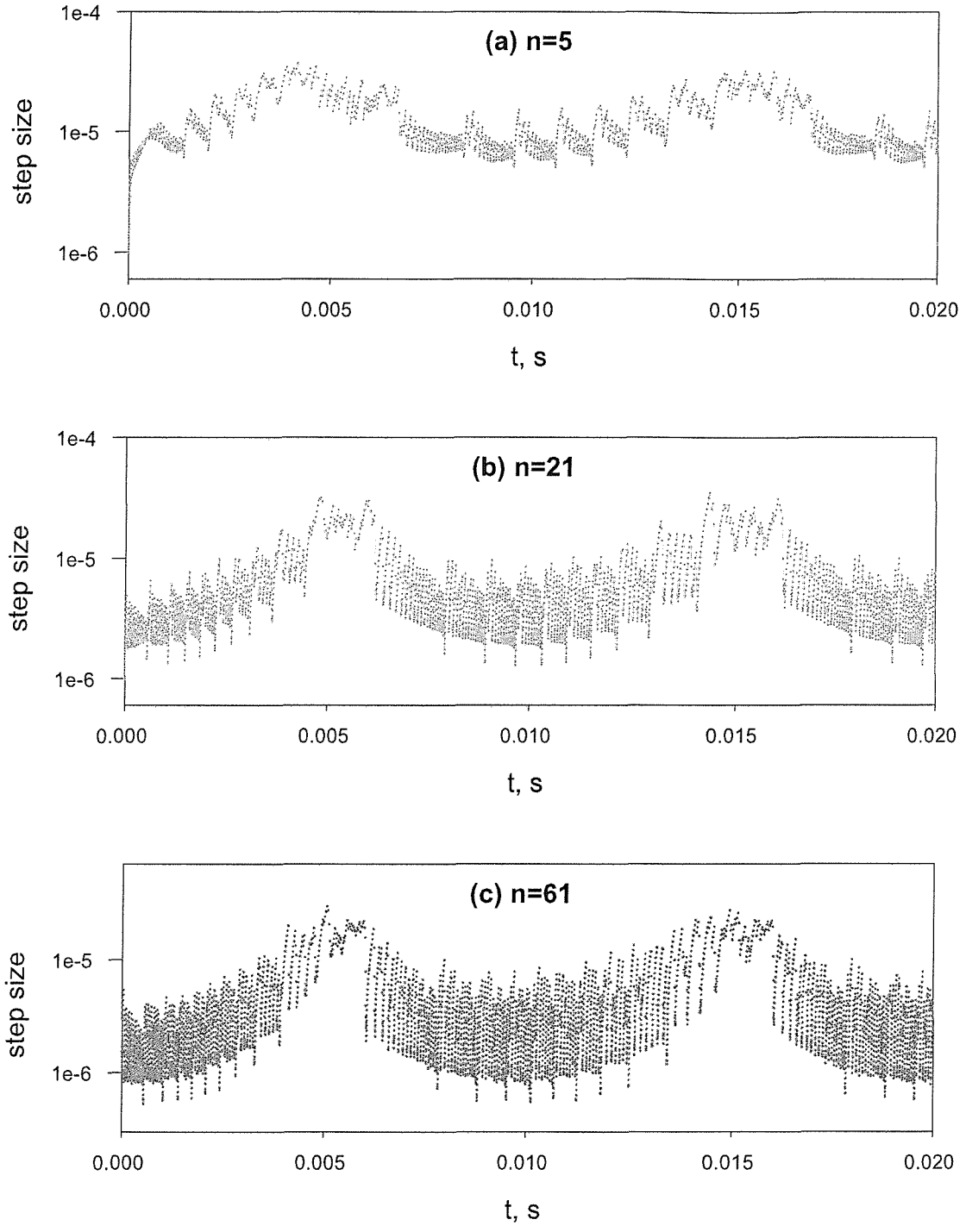

Figure 2.12: Step size required for different n-values.

	Total steps	Rejected steps	Accepted steps	Time (s)
$n = 5$	1891	64	1827	461
$n = 21$	4221	231	3990	1013
$n = 61$	6349	334	6015	1583

Table 2.8: Results for different n-values of the $E - J$ law.

3.32×10^{-6} for $n = 61$.

2.4.2 Results for different geometries

In this section Brandt's formulas were solved for superconductors with different aspect ratio (a/b). The width was set $2a = 0.002\,\mathrm{m}$. Three configurations were considered: the strip ($2b = 0.0001\,\mathrm{m}$), the square ($2b = 0.002\,\mathrm{m}$) and the slab ($2b = 0.02\,\mathrm{m}$).

Figure 2.13 shows current and field profiles for the three geometries at different amplitudes of the applied field such that in all the three cases at the first peak $B \approx B_p$, being B_p the field of total penetration when there is not current-free region. As it is expected for the strip, due to demagnetization effects the low field amplitude $B_0 = 0.03\,\mathrm{T}$ is enough to fully penetrate the superconductor, value close to $B_p = 0.032\,\mathrm{T}$ given by the theoretical formula shown in [10] for superconductors with $b \ll a$. For the slab (figure 2.13.(c)) B_a was set equal to 0.32 T, value higher than the theoretical prediction for total penetration $B_p = 0.25\,\mathrm{T}$ giving in [10] for $b \gg a$. Observe in figure 2.13.(c) that at the peak field the slab is already full penetrated since the density current J is almost J_c for the whole cross section and the field is slightly bigger than zero at the center of the superconductor. Similar situation is seen in figure 2.13.(b) for the square superconductor with $B_a = 0.24\,\mathrm{T}$, whereas from theoretical formula it was calculated $B_p = 1.18\,\mathrm{T}$.

The different behavior of strips and slabs are clearly seen in the profiles of $|B|$. For the strip geometry $|B|$ does not vary much along the thickness a difference with the square and slab. Another difference observed is due to the demagnetization effect found in the square and more evident in the strip where the value of the field in the edge is higher that the applied one reaching values of $B_a \approx 0.04\,\mathrm{T}$. However for the slab the magnetic field is equal to the applied field as it is expected for this geometry. The non-linearity of the field profile in the strip is clearly observed (figure 2.13.(a)) in contrast with the constant slope of the field profile for the slab (figure 2.13.(c)).

Due to the non-linearity observed for the strip profiles is it expected more difficulty

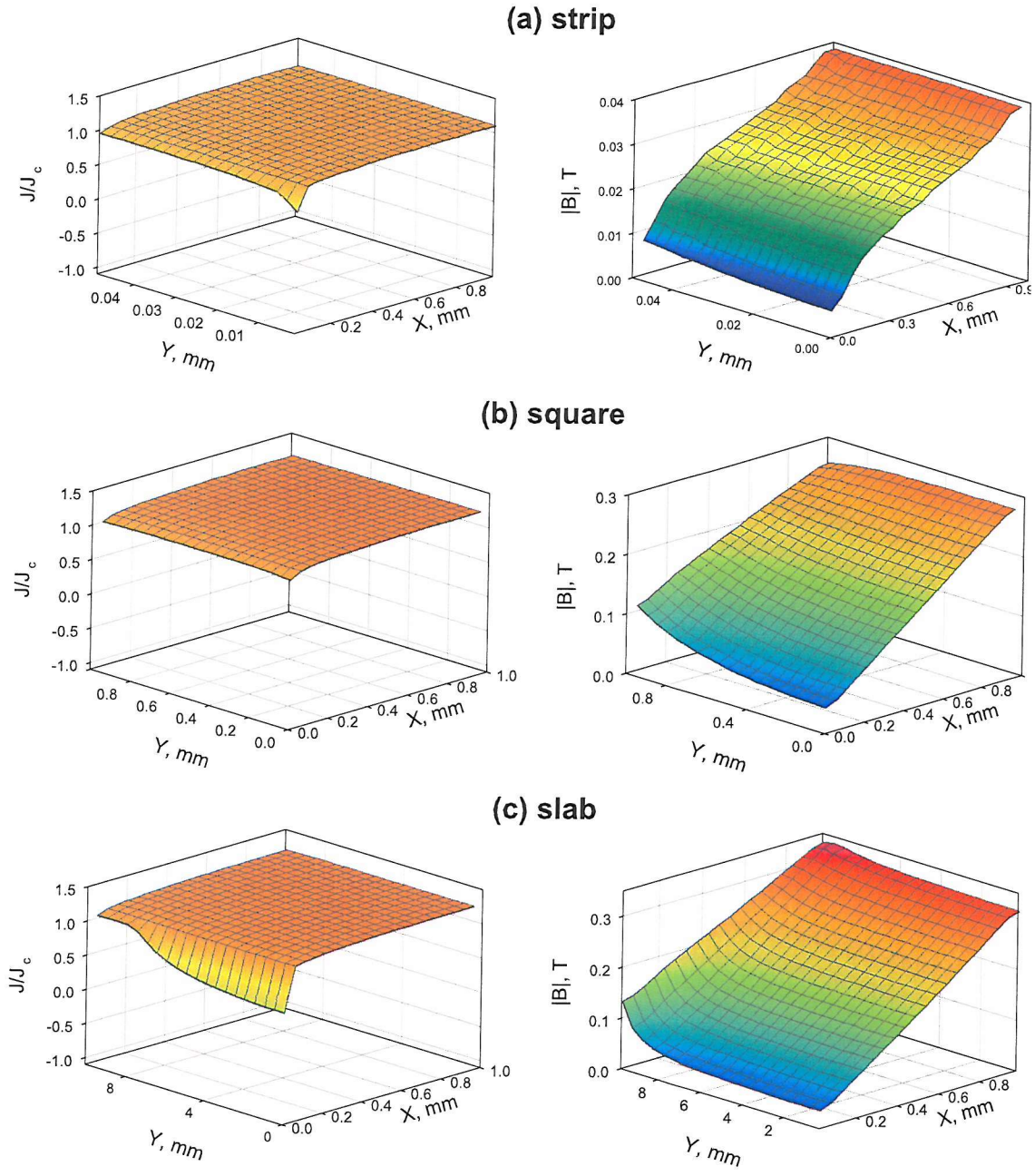

Figure 2.13: Current density and filed profiles for $b/a = 0.05$ (a), 1(b), 10(c) at $\omega t = \pi/2$.

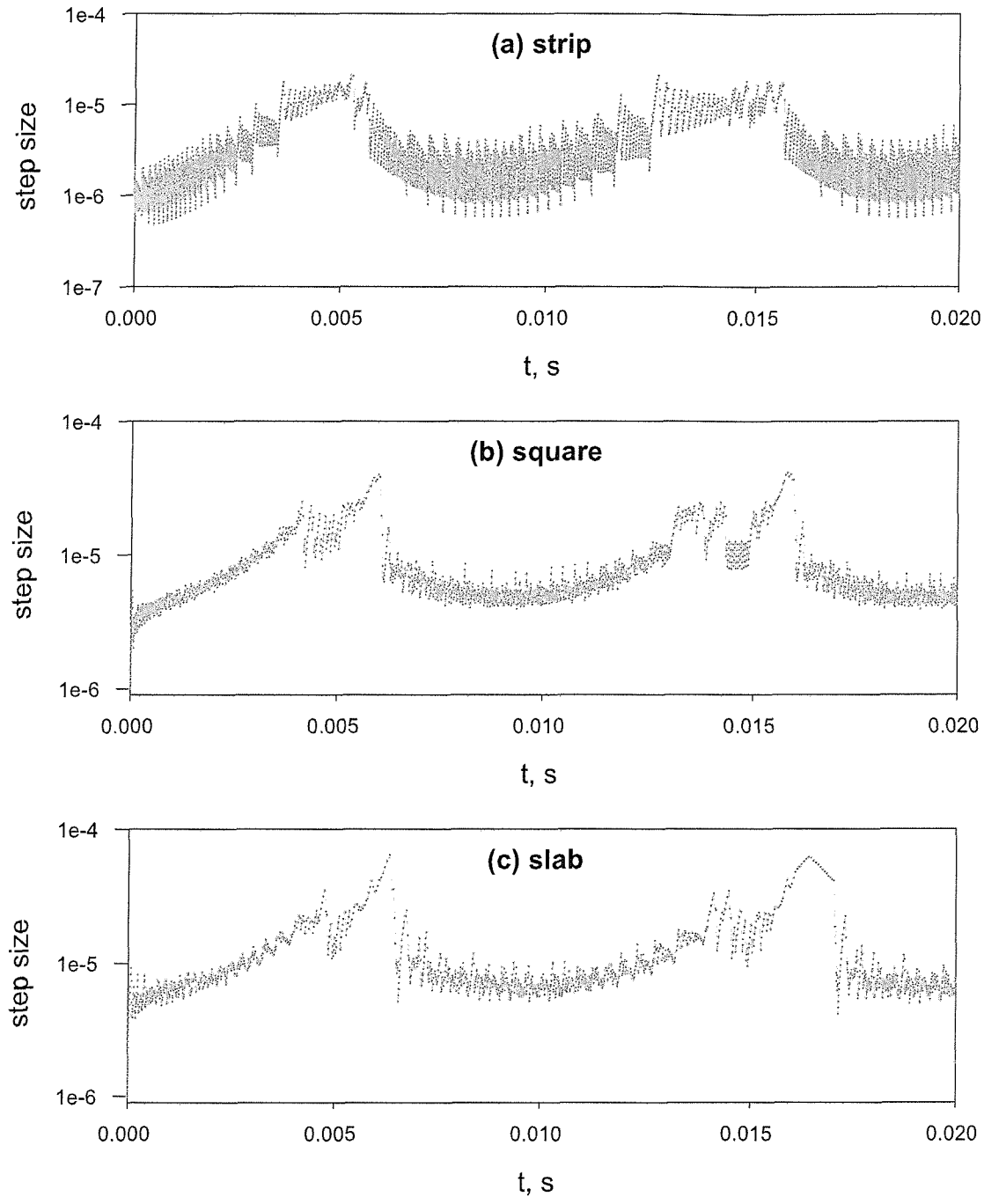

Figure 2.14: Step size required for Rosenbrock with $Tol = 10^{-6}$ for different applied field amplitudes.

	Total steps	Rejected steps	Accepted steps	Time (s)
$a/b = 20$	8509	448	8061	2100
$a/b = 1$	2936	109	2827	777
$a/b = 0.1$	2110	59	2051	563

Table 2.9: Results for different geometries.

for RODAS in order to maintain the stability of the integration for this geometry. That is proved in table 2.9 where the results indicate that a higher number of steps is required as the aspect ratio (a/b) increases, about four times more for the strip than for the slab which is quite considerable in terms of computational speed. Figure 2.14 represents the step sizes h taken along the integration interval. In accordance with the results displayed in table 2.9, it was found an average value of $h = 9.8 \cdot 10^{-6}$ for the slab, $h = 7.1 \cdot 10^{-6}$ for the square and $h = 2.4 \cdot 10^{-6}$ for the strip geometry.

2.5 Conclusion

A numerical method for the solution of 2D Brandt's equations for modelling superconductors with rectangular cross sections was described in this chapter. Due to the high non-linearity of the $E - J$ power law inserted in Brandt's formulation, the resulting differential equation is stiff.

The solver RODAS for stiff ODEs was presented and compared with other solvers. RODAS is based on the semi-implicit Rosenbrock method of order 4. Being simpler than other stiff solvers as implicit Runge-Kutta methods, it was found to be very efficient in terms of accuracy and computational costs and compared to other implementations of Rosenbrock methods.

Possible improvement of the method is to utilize an adaptive mesh such that the number of grid points is reduced in the part of the superconductor cross-section where the current remains constant the whole cycle time. For that, the integral kernel Q of the Brandt's equation must be changed, taking into account the different area of each cell.

At the end of the chapter, some current and field profiles were shown in different situations. Stiffness was found "stronger" in geometries with $b \ll a$, for fully penetration situations and for high n-values of the $E - J$ power law.

Chapter 3

Implementation of linear systems solvers in Flux3D

3.1 Introduction

In chapter 4, superconductors are modelled using Flux3D, which is a finite element method software package for electromagnetic calculations developed by CEDRAT. Flux3D has a special superconductor module for handling non-linear $E - J$ power-law.

The numerical computation is performed with the $\mathbf{T} - \Phi$ formulation, which uses the electric vector and the magnetic scalar potentials and whose general state equations are

$$\begin{aligned} \nabla \times \mathbf{H} = \mathbf{J} &= \nabla \times \mathbf{T} \\ \mathbf{H} &= \mathbf{T} - \nabla\Phi \\ \nabla \times \mathbf{E} = -\dot{\mathbf{B}} &= -\frac{\partial}{\partial t}\left(\mu_0 \left(\mathbf{T} - \nabla\Phi\right)\right) \end{aligned} \tag{3.1}$$

The solution of (3.1) is calculated for all the nodes on the FEM mesh at each time step. When $\mathbf{E}$ is calculated using non-linear characteristics such as the power-law for superconductors, Newton-Raphson method is required to obtain the solution, which consists in solving a series of linear systems until converges to the solution.

One of the difficulties found during the calculation process was the cost required to solve each linear system at each Newton-Raphson step. The method utilized, Bi-conjugated Gradient with Incomplete Gauss factorization (IGBCG) [21], is expensive

in terms of computing time and for ill-conditioned matrices can diverge easily. Tricks like increasing the number of time steps or changing the coefficient of relaxation for the Newton-Raphson method were helpful in order to obtain the convergence in some problems, but failed in others cases. Hence to continue with calculations in Flux3D it was concluded that new linear system solvers should be implemented.

In modelling of superconductors, the high non-linearity of the superconducting law leads to particularly ill-conditioned matrices. The problem accentuates as more difficult geometries or thinner meshes are included and therefore robust linear systems solvers are needed.

Two new iterative solvers, the preconditioned Generalized Minimal Residual method (GMRES) [29] and the preconditioned Biconjugated gradient stabilized method (Bi-CGStab) [37] were tested and compared with IGBCG. Both new methods were found to be robust and show better performance than IGBCG.

With the introduction of a preconditioner before solving the iterative process the convergence can be reached easily and the total computational cost reduced. Incomplete LU factorizations with variations were implemented as preconditioner for the new solvers [28]. It has been observed that for having a good method the main task is to find an effective preconditioned.

In the first part of the chapter the solvers are presented. Then performance of each method in superconductor's problems are compared. Finally, the solvers are tested in other transient magnetic problems modelled with Flux3D software [18].

3.2 Overview of linear systems solvers for sparse matrix

Methods to solve linear systems are classified in 2 groups: direct and iterative methods [44]. Direct methods give the exact solution after a finite number of operations. Although they are robust, when large systems are being solved the growing errors can become so large and so the results obtained are unsatisfactory. In addition, sometimes, a sparse matrix becomes full matrix when the factorization is done and then the storage requirement becomes unacceptable. There are some direct methods that avoid this using permutation of rows and columns in order to reduce the fill in.

Iterative methods start with an approximate solution and using a recurrence formula

calculate another approximations. This formula is applied again successively until the successive sequence converges to the solution. Iterative methods are easier to implement and for 3D simulations are recommended since they do not require too much memory comparing with direct schemes. The inconvenient of these methods is that when the matrix is not well conditioned the convergence is slow or not reached.

One of the techniques in order to improve the convergence of iterative methods is to use a preconditioner and apply the iterative formula to the new better-conditioned matrix. Experience has demonstrated that a good preconditioner is the key to an effective iterative solver. A typical one for general problems is based on incomplete factorization LU. The elimination is performed on A, but entries outside a certain sparsity pattern or below a cut-off numerical value are simply discarded during the factorization. The approximate LU factors then define the new system matrix. In that sense, iterative solvers can be considered as a union between direct and iterative methods.

For linear systems generated by FEM modelling in 3D, the matrix dimension is very high and therefore direct methods are not applicable due to the storage requirements. Among the iterative methods two solvers have been chosen to be tested and compared with IGBCG:

1. GMRES, Generalized Minimum Residual from Y.Saad [29], and
2. BiCGStab, Bi-conjugated gradient stabilized from H.A. Van Der Vorst [37].

Recent reports consider both methods to be the most suitable for bad conditioned problems with a similar performance.

3.3 Iterative solvers tested

The aim of the methods presented here is to obtain the solution of a linear system of the form $Ax = b$ where A is $N \times N$ matrix and b and x are vectors of dimension N.

3.3.1 Preconditioners

In order to accelerate the iterative process Preconditioners are used. The idea of "preconditioning" consists on transforming the original linear system into another one with the same solution but which is easier to solve by an iterative method. If the matrix M is the preconditioner which approximates A , then the transformed system, $M^{-1}Ax = M^{-1}b$ (left preconditioner) or $AM^{-1}(Mx) = b$ (right preconditioner) has the same solution as the original system but the properties are more favorable. The preconditioners used with

the solvers presented in this chapter are briefly described next.

LDU preconditioner for IGBCG:

The Gauss incomplete factorization is the preconditioner used for IGBCG method [13]. It uses the same principle of a full LDU factorization , but , in order to save the sparsity of the matrix it only computes the elements corresponding to the non-zero structure of A. It consists on calculating a matrix $M = LDU$, where L,D,U are approximations of the lower triangular ,diagonal and upper triangular matrices computed by the full LDU factorization algorithm.

Ilut preconditioner:

The simple Ilut preconditioner is based in an incomplete LU factorization of the original matrix, that is taking $M = LU$ where L and U are triangular matrices, with a dual dropping strategy. This allows us to keep the sparsity of the matrix and control the storage requirements. The dual dropping strategy of Ilut consists on two steps. Suppose we are in step k of the factorization. First all the elements calculated which value is less than a tolerance chosen Tol are dropped. Then only the largest $Lfil$ elements in the row k of L are kept and the same for the row k of U. The $Lfil$ limits the number of elements of the preconditioned matrix. Storage cost is now known in advance.

It is difficult to find the best values of the parameters for a particular problem. Tol depends on the value of the elements and level of fill, $Lfil$, can be chosen like $nnz/n+1$, where nnz is the number of non-zero coefficients and n the number of equations but it is not always the best choice.

Observe in tables 3.1 and 3.2, how the preconditioner affects to the solver. As Tol decreases, less coefficients are dropped, the factorization will be more accurate, then the method will converge faster reducing time inverted in the iterative process but increasing the time for the factorization. Therefore the optimal choice of Tol and $Lfil$ is when the increment of preconditioning time by using smaller tolerances or larger levels of filling is compensated with the reduction of the time required by the iterative solver. Notice in Table 3.2 how the execution time for performing the Ilut factorization increases with $Lfil$. At the same time the execution time for Gmres decreases as it could be expected, however observe that at $Lfil = 80$ it requires more steps than for lower values of $Lfil$. It is not always clear which are the best parameters for the preconditioner in order to transform the matrix into one with good conditioning properties and therefore accelerate the convergence. Generally, "low" $Lfil$, and "high" Tol, are not good proposals.

Tol	Ilut time (s)	Gmres time (s)	Precision	Iters	Storage for Ilut
0.0001	6	70	$9.89 \cdot 10^{-8}$	349	4795449
0.00001	8	66	$9.85 \cdot 10^{-8}$	348	4838205
0.000001	11	67	$9.98 \cdot 10^{-8}$	332	4851249

Table 3.1: Results for a system with 30307 equations and 1752105 non-zeros, using Gmres (80) +Ilut (Tol, 40) for different values of Tol.

$Lfil$	Ilut time (s)	Gmres time (s)	Precision	Iters	Storage for Ilut
20	3	135	$9.89 \cdot 10^{-8}$	815	2464163
30	4	82	$9.90 \cdot 10^{-8}$	454	3640719
40	6	70	$9.89 \cdot 10^{-8}$	349	4795449
60	8	84	$9.88 \cdot 10^{-8}$	349	7025163
80	11	91	$9.95 \cdot 10^{-8}$	382	9144861

Table 3.2: Results for a system with 30307 equations and 1752105 non-zeros, using Gmres (80) +Ilut (0.0001,Lfil) for different values of $Lfil$.

It is difficult the comparison of iterative solvers because of their dependence on a large number of parameters. Also, they depend on the preconditioner used, and the same preconditioner can work poorly for a set of parameters but it can give good performance for different ones.

3.3.2 Solvers

The iterative methods tested in this work belong to the group of "projection methods" based on the "Krylov subspaces".

A projection method for solving the linear system $Ax = b$ is a method which seeks an approximate solution x_m from an subspace $x_0 + K_m$ of dimension m by imposing the condition, $b - Ax_m \perp L_m$, where L_m is another subspace of dimension m. x_0 represents an arbitrary initial guess of the solution.

A Krylov subspace method is a method for which the subspace K_m is the Krylov subspace $K_m(A, r_0) = span\{r_0, Ar_0, A^2r_0, \ldots A^{m-1}r_0\}$, for $r_0 = b - Ax$. Depending on the choice for L_m there are different Krylov subspace methods.

3.3.2.1 GMRES

The Generalized Minimum Residual Method (GMRES) is a projection method based on taking $K_m = K_m(A, v_0)$ and $L_m = AK_m$ where K_m is the m-th Krylov subspace with $v_0 = r_0/\|r_0\|$.

Gmres minimizes the norm of the residual $\|b - Ax_m\|$ in K_m to obtain the m-th approximation to the solution x_m. The Krylov subspace is made orthogonal by the Gram-Schmidt procedure, known as an Arnoldi process when applied to a Krylov subspace.

Algorithm for GMRES:

1. Set an initial guess x_0.
2. Arnoldi method.

   Compute residual $r_0 = Ax_0 - b$, $\beta = \|r_0\|$, $v_1 = r_0/\beta$

   Define a matrix H_m with dimension $(m+1) \times m$. Set $H = 0$

   For $i = 1, 2 \ldots m$ do
   $\omega_i = Av_i$
   For $j = 1, 2 \ldots i$ do
   $H_{j,i} = (\omega_i, v_j)$
   $\omega_i = \omega_i - h_{j,i}v_j$
   end do
   $h_{i+1,i} = \|\omega_i\|$
   if $h_{i+1,i} = 0$, set $m = i$ and go to 3
   $v_{i+1} = \omega_i/h_{i+1,i}$
   end do
3. Solve GMRES minimization problem
   - Compute y_m such that minimizes $\|\beta e_1 - H_m y\|$
   - $x_m = x_0 + V_m y_m$

All the vectors computed in the orthogonal sequence have to be retained. This supposes a lot of memory requirements and computer time when m becomes large. The

usual way to overcome this limitation is by restarting the iteration. After a number of iterations fixed (im), the accumulated data are cleared and the intermediate approximations are used as the initial data for the next im iterations. This is repeated until convergence is achieved.

Algorithm for Restarted GMRES (im):

1. Set an initial guess x_0
2. **Arnoldi method.**
3. Solve GMRES minimization problem and compute new x_m
4. **Restart**
   If satisfied stop else $x_0 = x_m$ and go to 2.

There are many possible variations of the restarted Gmres. A very "small" value of im can result in a very slow convergence or even no convergence (see table 3.3). But a larger value involves excessive work and uses a lot of storage. Exactly, the space required for Gmres (im) is given by $(N+3)\times(im+2)+(im+1)\times im/2$ where N is the dimension of the system. For the tests in problems with superconductors it was found that with $im = 80$, Gmres converges easily.

im	Gmres time	Precision	iters
20	54s	$9.6 \cdot 10^{-8}$	457
40	8s	$7.4 \cdot 10^{-8}$	70
60	6s	$8.3 \cdot 10^{-8}$	55
80	6s	$8.3 \cdot 10^{-8}$	55

Table 3.3: Results for Gmres(im) with Ilut(130,10^{-6}).

3.3.2.2 BCG

The Biconjugated Gradient method (BCG) is a Kyrlov subspace method with

$$L_m = span\left\{\omega_0, A^{\mathrm{T}}\omega_0, (A^{\mathrm{T}})^2\omega_0, \ldots (A^{\mathrm{T}})^{m-1}\omega_0\right\}$$

The vector ω_0 is arbitrary, provided $(r_0, \omega_0) \neq 0$, but is often chosen to be equal to $r_0/\|r_0\|$.

A difference with GMRES, instead to one orthogonal sequence of the residuals, the BCG method builds two mutually orthogonal sequences of residuals without providing a minimization. Although the length of these sequences can become large, only a small number of vectors need to be kept in memory.

Algorithm for BCG:

1. Compute residual $r_0 = Ax_0 - b$
   Choose $\tilde{r}_0$ such that $(r_0, \tilde{r}_0) \neq 0$
2. Set $p_0 = r_0$, $\tilde{p}_0 = \tilde{r}_0$
3. For $i = 0, 1, \ldots$ until convergence do
   $\alpha_i = (r_i, \tilde{r}_i)/(Ap_i, \tilde{p}_i)$
   $x_{i+1} = x_i + \alpha_i p_i$
   $r_{i+1} = r_i - \alpha_i A p_i$
   $\tilde{r}_{i+1} = \tilde{r}_i - \alpha_i A^{\mathrm{T}} \tilde{p}_i$
   $\beta_i = (r_{i+1}, \tilde{r}_{i+1})/(r_i, \tilde{r}_i)$
   $p_{i+1} = r_{i+1} + \beta_i p_i$
   $\tilde{p}_{i+1} = \tilde{r}_{i+1} + \beta_i \tilde{p}_i$
   end for

3.3.2.3 BiCGStab

The Bi-Conjugate Gradient Stabilized method from H.A. Van Der Vorst [37], was developed to improve the convergence of BCG.

BiCGStab produces iterates which residuals vectors are calculated of the form $r_j = \psi_j(A)\phi_j(A)r_0$ in which $\phi_j(t)$ is the residual polynomial associated with the BCG algo-

rithm and $\psi_j(t)$ is a new polynomial which is defined recursively at each step with the goal of "stabilizing" the convergence behavior of the original algorithm.

Algorithm for BiCGStab :

1. Compute $r_0 = b - Ax_0$ for an initial guess x_0, $\tilde{r}_0$ arbitrary.
2. $p_0 = r_0$
3. For $i = 0, 1, \ldots$ until convergence do
   $\alpha_i = (r_i, \tilde{r}_0)/(Ap_i, \tilde{r}_0)$
   $s_i = r_i - \alpha_i Ap_i$
   $\omega_i = (As_i, s_i)/(As_i, As_i)$
   $x_{i+1} = x_i + \alpha_i p_i + \omega_i s_i$
   $r_{i+1} = s_i - \omega_i As_i$
   $\beta_i = \frac{(r_{i+1}, \tilde{r}_0)}{(r_i, \tilde{r}_0)} \times \frac{\alpha_i}{\omega_i}$
   $p_{i+1} = r_{i+1} + \beta_i(p_i - \omega_i Ap_i)$
   end for

3.3.3 Storage requirements

A important point to have into account for comparing numerical methods is their storage requirements. This can be calculated in advance by knowing the size of the matrix.

Knowing the parameters:

N= Number of equations, and

NNZ= Number of non-zero elements of the matrix.

the number of reals needed in each method is calculated with the formulas presented in the following table,

	Symmetric case	Non-symmetric case
IGBCG	$5 \times N + 2 \times NNZ$	$7 \times N + 4 \times NNZ$
Gmres +Ilut	$2(2Lfil+1)N + 3N + NNz + (n+3)(im+2) + (im+1)im/2$	
Gmres(80)+Ilut	$(4Lfil+87)N + 2NNZ + 3486$	
BiCGStab	$8N + (Lfil+1) \cdot N + 3N$	

Clearly, as it will be shown in the tests, unless the dimension of the matrix is "large" and the $Lfil$ chosen for the preconditioner very "small", Gmres will take more memory space.

3.4 Superconductor Problem

The difficulty found in the solving process of Flux3D for modelling superconductors, is due to the highly non-linear $E-J$ property, $E = E_0 (J/J_c)^n$, which leads to linear systems with ill-conditioned matrices which are difficult to solve. Newton-Raphson method is applied each time step and at each iteration of Newton-Raphson a linear system is solved . All this together means a very long calculation process. A fast and robust linear system solver becomes very important.

3.4.1 Description of the tested problems

In order to test the solvers, they were applied to two different problems with superconductors.

Problem 1

This model, shown in figure 3.1, consists of 2 parallel long slabs with a normal matrix between them in a sinusoidal applied field $B = B_0 sin(2\pi ft)$ with $\omega = 10\,\mathrm{Hz}$ and $B_a = 0.7\,\mathrm{T}$. The non-linear $E-J$ power law for the superconductors is given by the parameters: $n = 21$, $J_c = 2 \cdot 10^8\,\mathrm{Am}^{-2}$, and $E_c = 0.001\,\mathrm{Vm}^{-1}$.

Problem 2

The second model (Figure 3.2) represents several superconductor filaments in a silver matrix. The non-linear property is given by $n = 16.8$, $J_c = 1.61 \cdot 10^8\,\mathrm{Am}^{-2}$, and $E_c = 0.001\,\mathrm{Vm}^{-1}$. A current source $I = 5.92\sin(2\pi 50t)$ is imposed.

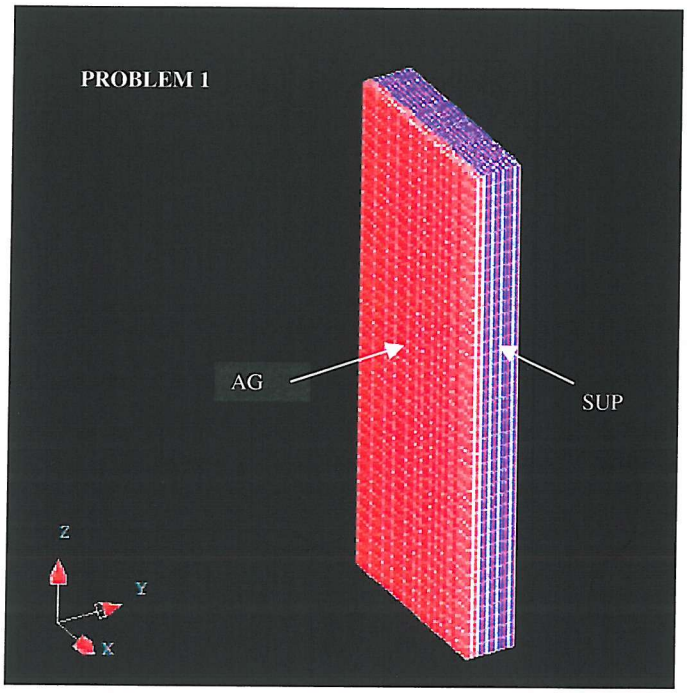

Figure 3.1: Geometry and mesh of problem 1.

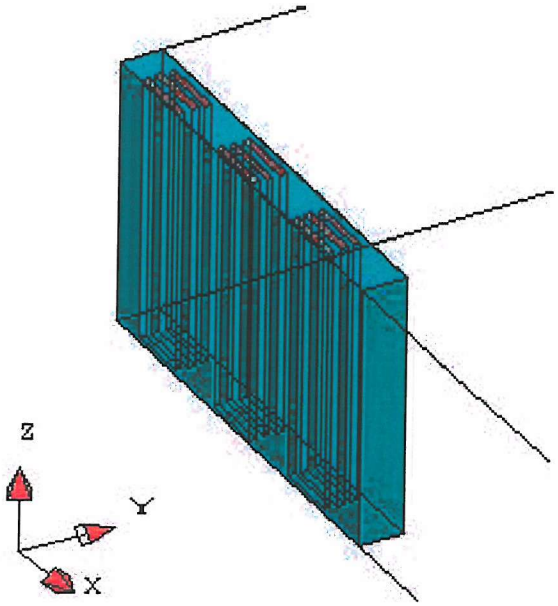

Figure 3.2: Geometry of problem 2.

3.4.2 Results and comments

Since the problems are non-linear, each time step the Newton-Raphson method is applied and therefore the consequent linear systems have to be solved. As examples two of them were chosen of each problem (System 1 and System 2).

The characteristics of the matrix for Problem 1 are:

- Dimension: 37703
- Number of non-zeros in the matrix: 2579157

The results obtained are presented in the next table:

	System 1		System 2	
	Storage ($N^o real \cdot 10^6$)	**Time**(s)	**Storage** ($N^o real \cdot 10^6$)	**Time**(s)
IGBCG	8.148	1430	8.148	Diverges
GMRES	23.591	184	23.591	320
BiCGStab	10.161	173	10.161	129

Characteristics of the matrix for Problem 2:

- Dimension:29739
- Number of non-zeros in the matrix:1441607

The results found were:

	System 1		System 2	
	Storage ($N^o real \cdot 10^6$)	**Time**(s)	**Storage** ($N^o real \cdot 10^6$)	**Time**(s)
IGBCG	5.144	8379	5.144	Diverges
GMRES	10.653	780	10.653	720
BiCGStab	22.194	857	22.194	773

Observe that there are linear systems in both problems which could not be solved using IGBCG. For all the other cases, GMRES and BiCGStab have converged much

faster than IGBCG. It is clear then the better performance of the solvers GMRES and BiCGStab for superconducting problems, despite the disadvantage of higher memory requirements.

3.5 Results for transient electromagnetic problems

Apart from the superconducting problems, the new solvers were tested in other transient electromagnetic problems solved with Flux3D. In some of them the matrices arisen in the solving process are very bad conditioned, whereas other ones were not so difficult to solve but they were used to compare the performance of the different solvers in terms of computational speed and storage requirements.

The results in table 3.4 show the performance of the three methods in solving the linear system of the first time step. When the problem is not linear the results correspond to the second iteration of Newton-Raphson process.

In terms of computational time, it is observed that when the matrix of the system A is symmetric IGBCG is faster, however for non-symmetric matrices both GMRES and BiCGStab converge sooner, a fact which becomes more evident as the size of the linear system increases (test 9 and test 10). Respect to the memory requirements, notice that IGBCG uses less memory size in all the problems.

In conclusion, we can say that for linear systems with symmetric matrices the three solvers are robust being IGBCG more convenient in order to save memory space. With non-symmetric matrices, although all the methods reach the convergence, GMRES and BiCGStab do it easily.

		Storage ($N^o real \cdot 10^3$)	**Time**(s)
Test 1 Non-sym	**IGBCG**	2296	15
	GMRES	3014	13
	BiCGStab	1633	19
Test 2 Non-sym	**IGBCG**	2420	6.5
	GMRES	3028	6
	BiCGStab	2275	7
Test 3 Non-sym	**IGBCG**	1919	7
	GMRES	2403	6
	BiCGStab	1753	7
Test 4 Sym	**IGBCG**	4909	24
	GMRES	9459	28
	BiCGStab	6515	26
Test 5 Non-sym	**IGBCG**	2955	52
	GMRES	8042	11
	BiCGStab	3097	12
Test 6 Sym	**IGBCG**	4519	24
	GMRES	9828	30
	BiCGStab	4379	36
Test 7 Sym	**IGBCG**	3855	20
	GMRES	8279	25
	BiCGStab	5666	28
Test 8 Non-sym	**IGBCG**	4500	67
	GMRES	9272	89
	BiCGStab	5013	75
Test 9 Non-sym	**IGBCG**	8148	1430
	GMRES	23591	184
	BiCGStab	10161	173
Test 10 Non-sym	**IGBCG**	5144	8379
	GMRES	10653	780
	BiCGStab	22194	857

Table 3.4: Results for 10 different test of transient magnetic problems.

3.6 Conclusion

The purpose of the tests presented is this chapter was to compare different linear systems solvers, Gmres, IGBCG and BiCGStab, in terms of computation time and memory requirements for problems modelled with a FEM software.

For the problems with superconductors, Gmres and BiCGStab resulted to be more effective since IGBCG not always converges. For problems in 3D transient electromagnetic problems in which all the three solvers converge, it was observed that whereas Gmres and BiCGStab give better results in terms of solving process time, are less effective with respect to the memory space requirements. Only in particular cases when the matrix is symmetric IGBCG has faster convergence.

The performance of the linear systems solvers are strongly influenced by the preconditioner used. A good performance of the solvers Gmres and BiCGStab in problems where IGBCG fails, is the outcome of a good election of the parameters used for the preconditioner Ilut. For each problem there is an optimal level of fill and tolerance which is difficult to predict. Sometimes the linear system can only be solved with a big level of fill, increasing considerably the memory space used.

In conclusion, the results of the tests shown in this chapter have proved the robustness of Gmres and BiCGStab solvers for 3D transient electromagnetic problems, being more effective than IGBCG solving systems with non-symmetric matrices.

Chapter 4

3D modelling of coupling in AC magnetic field using Flux3D

4.1 Introduction

In presence of an ac magnetic field, the movement of vortices in the superconductor produces energy dissipation, that is, hysteresis losses. In order to reduce them, the superconductor is divided into fine filaments embedded in a normal matrix. Such strategy is only effective providing that the filaments are uncoupled. Filament coupling in long lengths conductors is prevented by twisting the filaments at a short pitch [38].

Loss reduction in twisted multifilamentary superconductors is not achieved if the filaments are coupled easily. The coupling phenomenon is influenced by parameters such as the changing rate of the magnetic field, the metal matrix resistivity, the critical current density, and the size and geometry of the filaments.

It is known qualitatively that for a very small ramp rate of the applied field, $\dot{B} \approx 0$, the filaments behave independently. But as $\dot{B}$ increases to a very high value, $\dot{B} \rightarrow \infty$, the induced voltage in the normal matrix allows all the current to cross from one filament to the other and the superconductors are acting as a single larger one. Figure 4.1 shows the corresponding field profiles to both limiting cases.

Theoretical quantitative prediction of this effect is limited to the case of two fully penetrated slabs and under the assumptions of the critical state model [41]. For studying more complicated geometries involving finite dimensions, and for magnetic fields only

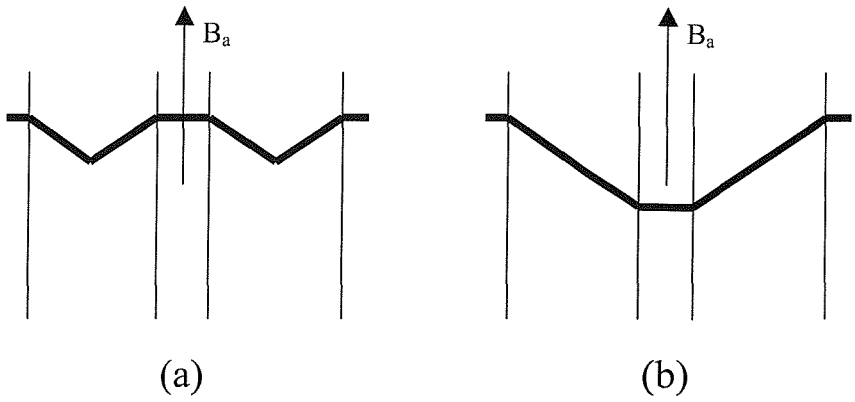

Figure 4.1: Sketch of the magnetic field profiles of two filaments uncoupled (a) and fully coupled (b).

partially penetrating the superconductor, an accurate 3D model is necessary. Numerical models based on the finite element method, FEM, has been widely used for calculation of field and current distributions [3, 34].

In this chapter the FEM software Flux3D [18] was used to model the coupling effect between finite superconductors due to the presence of an ac magnetic field. First a brief description of the FEM is given, followed by detailed results for strip and slabs geometries in an sinusoidal magnetic field, in order to show the capability of the FEM to calculate the coupling effect. An approximation of the critical coupling field $\dot{B}_c$ is obtained for both geometries, and compared with existing theoretical models. Finally, the coupling phenomenon is investigated in superconductors of different geometries in an applied field with constant ramp rate.

4.2 FEM modelling

Thank to the rapid progress on computing power, modelling using the finite element techniques is nowadays a common task for 2D and 3D electromagnetic calculations. FEM for modelling superconductors has been developed by some authors [3], and inserted in commercial packages as Flux3D [18].

Results shown in this chapter have been obtained using Flux3D. The basic 2D model in Flux2D for superconductivity was modified with new formulations later introduced into the 3D model developed for Flux3D. This model allows the introduction of more

complicated geometries and characteristics like the non-linear $E - J$ power law.

The 5 steps followed in order to model a problem in Flux3D are: description of the geometry, mesh, physical properties description, solving processor and analysis of the results.

4.2.1 Geometry and mesh

The model studied consists on two slabs/strips with normal matrix between them, and two more slabs/strips, one on the top and another at the bottom. The cross section is shown in figure 4.2. Due to the symmetries respect to the main planes, XY, YZ and ZX, only one eight of the total volume will be considered reducing the mesh size and therefore the computational costs to solve the problem. In figure 4.2 the right upper quarter modelled is enclosed by short dashed red lines. Then two volumes of superconductor material and one of normal conductor are built, all of them inside a volume representing the air region. Defining parameters and geometrical transformations building the geometry is an easy task in Flux3D. To take into account the exterior it is sufficient to describe an air box of a size important enough so that the effect of the infinite assimilation is negligible. There is also the possibility to describe an "infinite box" which links the open domain with a closed one by a spatial transformation and giving better approximations.

In order to mesh the studied domain in finite elements the whole box was constructed using eight volumes in order to have different meshes in each of them. Finer ones were used for the parts close to the boundaries of the superconductor, and bigger size meshes for the unchanging parts. For the superconductor, the matrix and the air volumes close to them a mapped mesh extruded was used along the length of the superconductor. Then the volumes are composed of hexahedrons and their faces in rectangles. The extrusion mesh is advantageous since allows to take into account thin geometries without increasing the number of elements much. For the remaining parts, it was used an automatic mesh which creates triangles covering the faces and the volumes are divided in tetrahedrons. Figures 4.3 and 4.4 show the geometry and the meshes chosen.

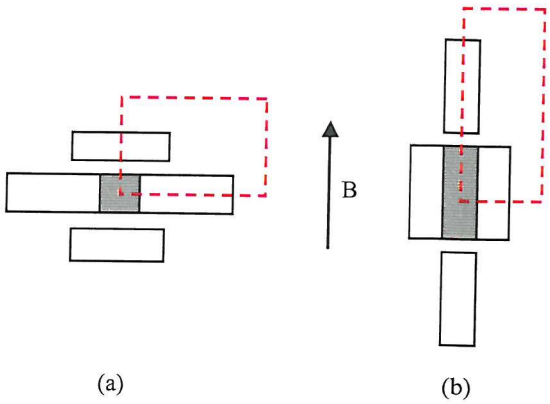

Figure 4.2: Sketch showing the cross-section of the geometry used for modelling strips (a) and slabs (b). The area enclosed by red dashed lines represents the region used for calculations in Flux3D.

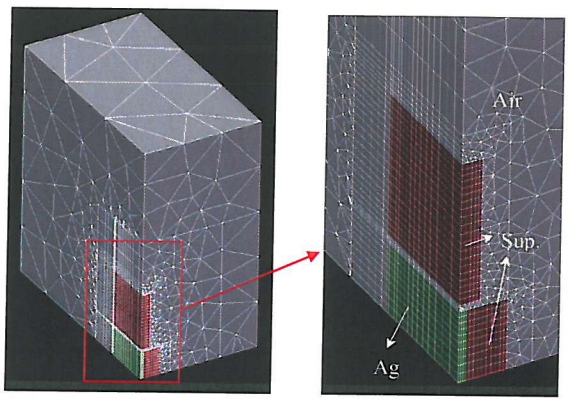

Figure 4.3: Geometry and mesh for modelling slabs with Flux3D.

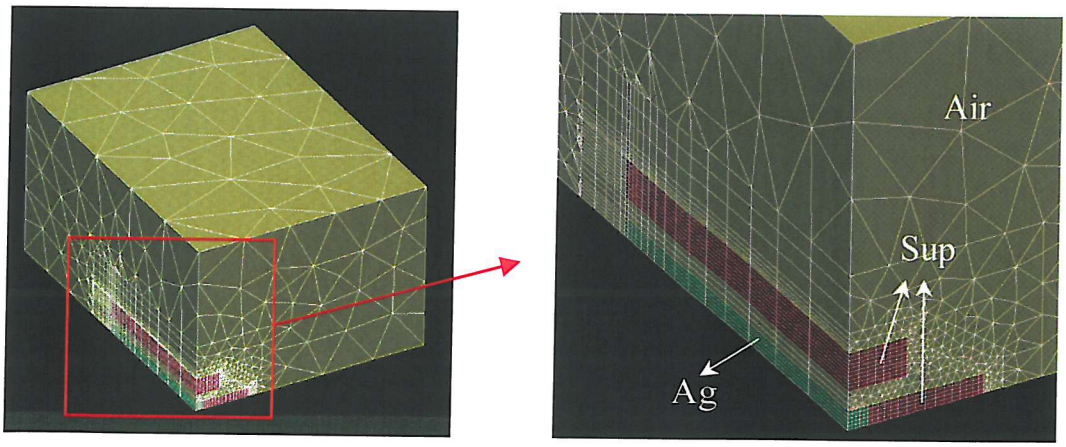

Figure 4.4: Geometry and mesh for modelling strips with Flux3D.

4.2.2 Physical properties

The constitutive equations are assigned to the different materials, which are associated to different regions created associating different volumes of the geometry.

For the superconducting material, the $B - H$ property is described in Flux3D by $\mathbf{B} = \mu_0\mathbf{H}$ which is a good approximation of type-II superconductors when $H \geq H_{c1}$. The $E - J$ relation inserted is the non-linear $E - J$ power law $\mathbf{E} = E_c \left(|\mathbf{J}|/J_c\right)^n \frac{\mathbf{J}}{J_c}$. The normal metal is defined by $\mathbf{E} = \rho_m\mathbf{J}$.

As boundary condition it was imposed a field varying in time over the entire modelled device in the z direction.

The numerical method is based on solving Maxwell equations. There are different ways to formulate them [36]. The $A - V$ formulation uses Ampere's law as a state equation which is expressed as

$$\nabla \times \frac{1}{\mu_0}\nabla \times \mathbf{A} = \sigma(\mathbf{E}) \cdot \mathbf{E}$$

with

$$\mathbf{E} = -\frac{\partial \mathbf{A}}{\partial t} - \nabla V.$$

The $\mathbf{T} - \Phi$ formulation consists on taking electromagnetic potentials $\mathbf{T}$ and Φ as state variables. $\mathbf{T}$ is the electric vector potential, $\mathbf{J} = \nabla \times \mathbf{T}$, and Φ the scalar magnetic potential, $\mathbf{H} = \mathbf{T} - \nabla\Phi$. Then the equations became

$$\begin{aligned} \nabla \times \mathbf{H} = \mathbf{J} &= \nabla \times \mathbf{T} \\ \mathbf{H} &= \mathbf{T} - \nabla\Phi \\ \nabla \times \mathbf{E} = -\dot{\mathbf{B}} &= -\frac{\partial}{\partial t}\left(\mu_0\left(\mathbf{T} - \nabla\Phi\right)\right) \end{aligned}$$

The $\mathbf{T} - \Phi$ formulation is used in Flux3D. It has a better convergence behavior since it uses $E(J)$ characteristics instead of $J(E)$, which is particularly suited for Newton-Raphson iteration, implemented in Flux 3D.

4.2.3 Solving process

The solving process consists on two main tasks:

- Integration of the sub-matrices and the sub-vectors belonging to each element and assembly through the non-linear finite element system.
- Solving of this non-linear system using Newton Raphson method.

Newton-Raphson is an iterative method to solve non-linear equations $f(x) = 0$. It builds a succession of linear systems until converges to the solution. From a given x_0 the next steps are calculated as:

$$x_{i+1} = x_i - \frac{f(x_i)}{f'(x_i)} \tag{4.1}$$

In order to improve the method a coefficient of relaxation is introduced.

To solve those linear systems generated in (4.1), different iterative numerical methods can be used in Flux3D for symmetric and nonsymmetric matrices respectively. Detailed explanation about numerical methods to solve the linear equations is given in chapter 3.

4.3 Results for sinusoidal B

The results presented in this section were calculated with the models described in previous section (figures 4.3 and 4.4) with the physical properties given by the parameters: $J_c = 2 \times 10^8\,\mathrm{Am}^{-2}$, $E_c = 10^{-3}\,\mathrm{Vm}^{-1}$ and $n = 21$. The resistivity of the normal matrix is $\rho = 10^{-8}\,\Omega\mathrm{m}$. The calculations were performed for an external sinusoidal applied field, $\mu_0 H = \mu_0 H_a \sin(\omega t)$, perpendicular to the superconductor.

Since the main interest is in the coupling between the superconductors, it will be shown the result only for the two superconductors in parallel joined by the normal matrix. Due to the symmetries respect to the main planes, only a quarter of the total model will be represented (See figure 4.2). For the profiles in the whole model, have into account that they are symmetric for the magnetic field and antisymmetric for the current.

4.3.1 Slab

Consider finite slabs of width $a = 3\,\mathrm{mm}$, height $b = 10\,\mathrm{mm}$ and length $l = 20\,\mathrm{mm}$. The width of the normal matrix between them is $w = 0.5\,\mathrm{mm}$. The amplitude of the applied

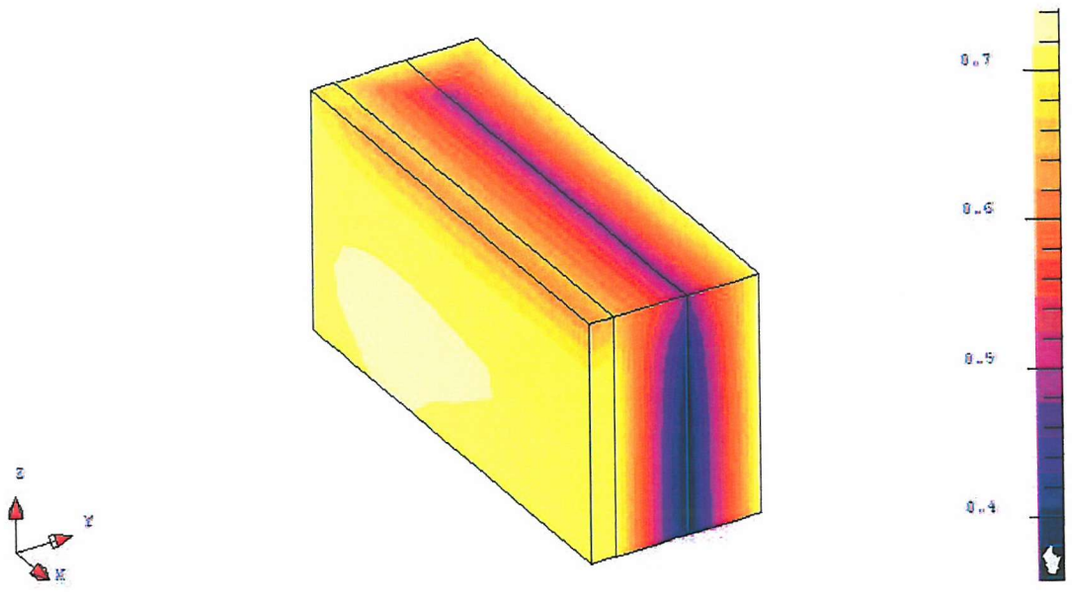

Figure 4.5: Magnetic field in slabs at $\omega t = \pi/2$ for $\mu_0 H_a = 0.7\,\mathrm{T}$ and $f = 1\,\mathrm{Hz}$.

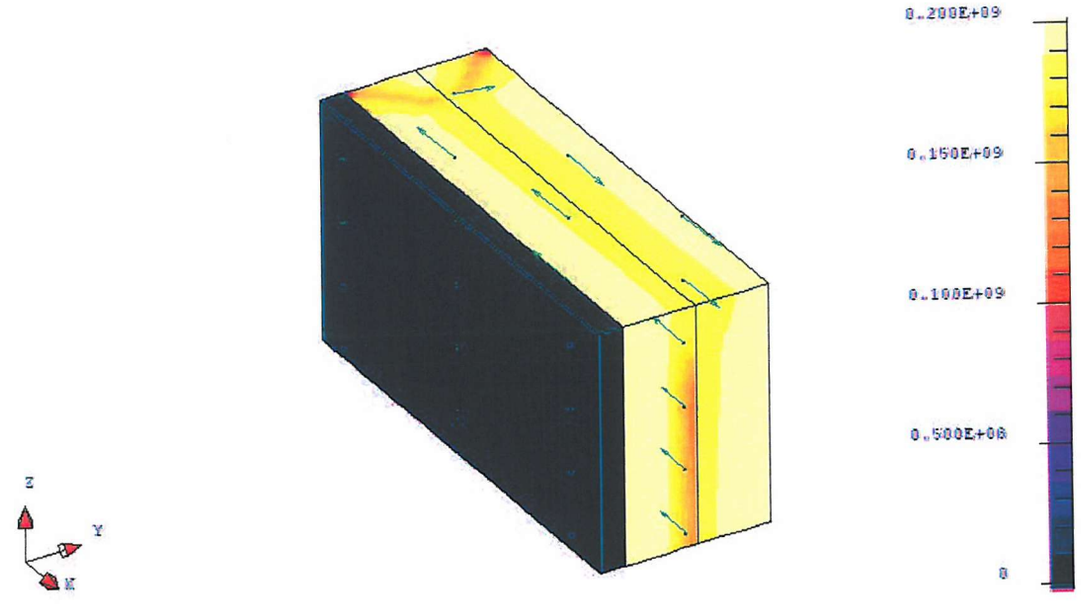

Figure 4.6: Induced current in slabs at $\omega t = \pi/2$ for $\mu_0 H_a = 0.7\,\mathrm{T}$ and $f = 1\,\mathrm{Hz}$.

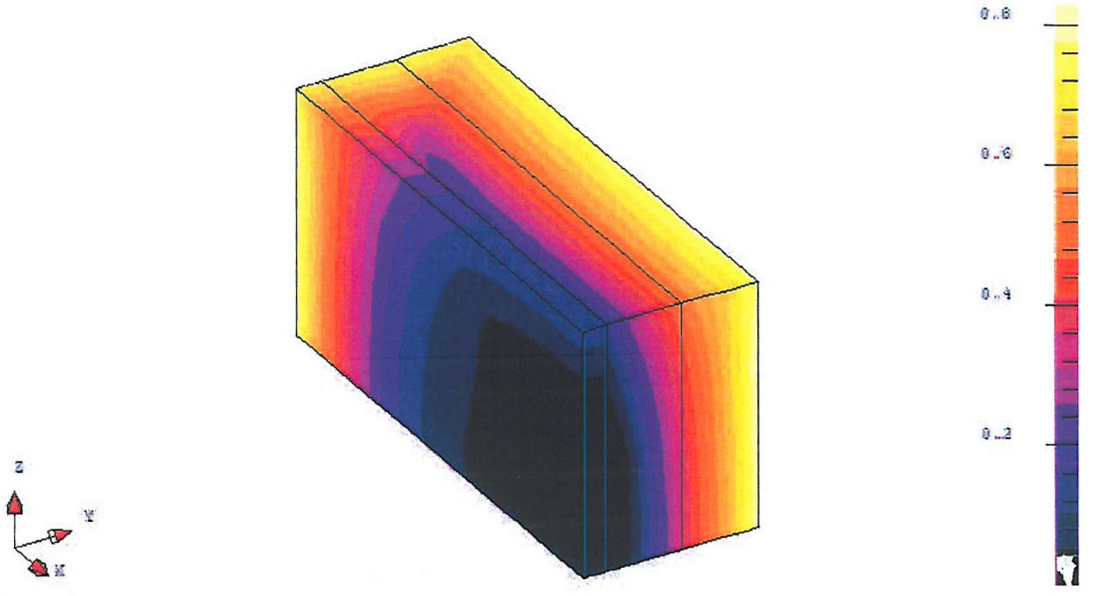

Figure 4.7: Magnetic field in slabs at $\omega t = \pi/2$ for $\mu_0 H_a = 0.7\,\mathrm{T}$ and $f = 200\,\mathrm{Hz}$.

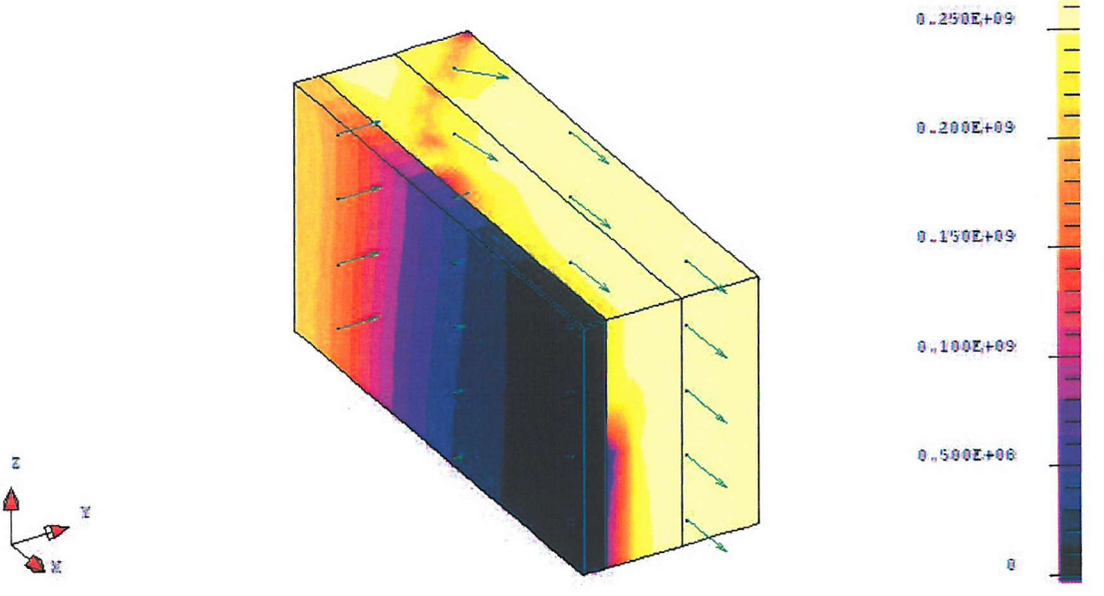

Figure 4.8: Induced current in slabs at $\omega t = \pi/2$ for $\mu_0 H_a = 0.7\,\mathrm{T}$ and $f = 200\,\mathrm{Hz}$.

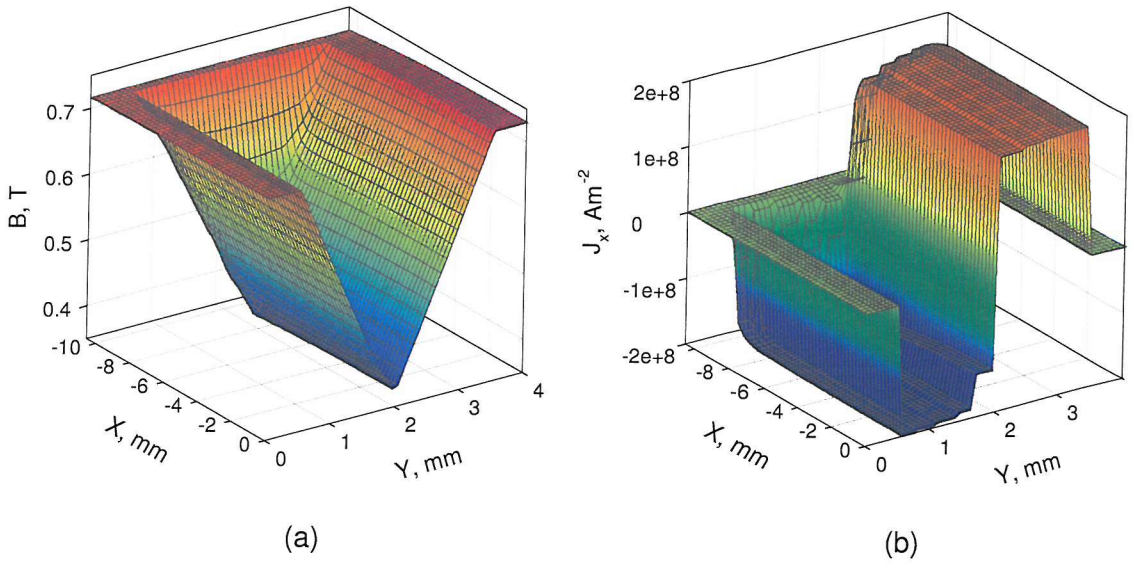

Figure 4.9: Magnetic field (a) and induced current (b) in slabs at $\omega t = \pi/2$ for $\mu_0 H_a = 0.7\,\mathrm{T}$ and $f = 1\,\mathrm{Hz}$.

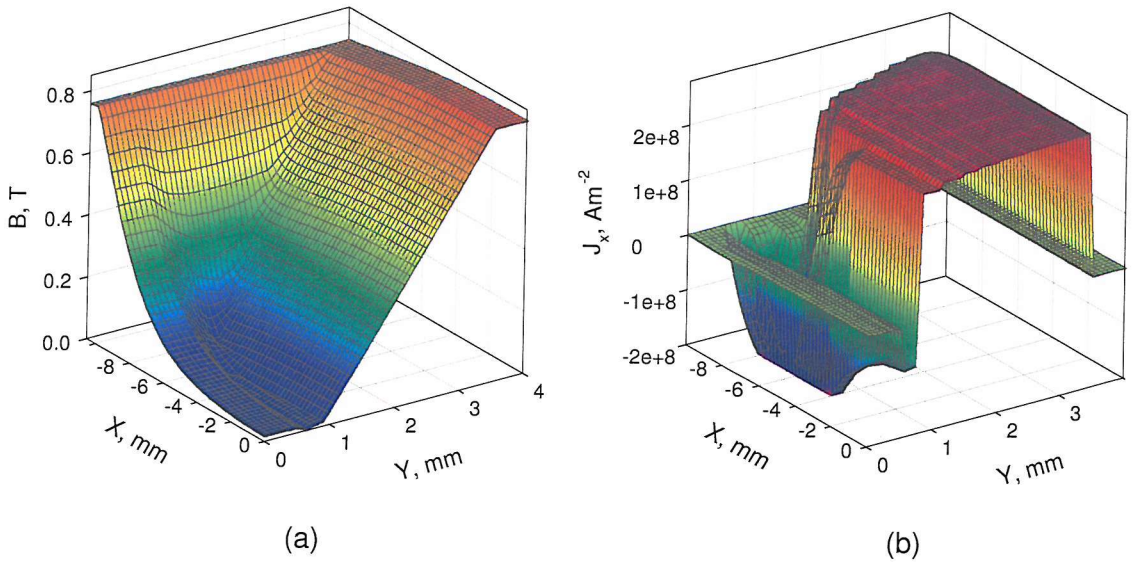

Figure 4.10: Magnetic field (a) and induced current (b) in slabs at $\omega t = \pi/2$ for $\mu_0 H_a = 0.7\,\mathrm{T}$ and $f = 200\,\mathrm{Hz}$.

field is $\mu_0 H_a = 0.7\,\mathrm{T}$.

Results in figures 4.5 and 4.6 show the field an current profiles respectively for a low frequency of the applied field, $f = 1\,\mathrm{Hz}$. Observe that the superconductor is fully penetrated by the applied field, hence the current is flowing through the whole device. The slabs are uncoupled and therefore the profiles for each one are similar to those for a single one, current flows around each superconductor as it is indicated with the arrows in the current profile (figure 4.6), and the field in the matrix is equal to the applied field (figure 4.5).

The situation is different for coupled slabs. Figures 4.7 and 4.8 are solutions for a higher frequency, $f = 200\,\mathrm{Hz}$. The current is now flowing in the same direction inside the superconductor, crossing the normal matrix and coming back through the other one. Then the two slabs behave as one superconductor (figure 4.8). Notice the field in the matrix region is now decreasing from the outer part to the center (figure 4.7).

The coupling effect can be seen in more detail restricting to the xy-plane the profiles of the field and the induced current along the conductor, as it is shown in figures 4.9 and 4.10. Figure 4.9 corresponds to the case of uncoupled slabs ($f = 1\,\mathrm{Hz}$). Notice that the field in both sides of the superconductor is equal to the applied field since there is not coupling currents crossing the matrix. The superconductors behave as 2 independent ones. These results for each superconductor isolated are similar to the predicted by Bean's model for infinite slabs [5]. The field in the superconductors decreases linearly form the borders to the middle with slope given by $\nabla \times H = J$. Increasing the frequency, the currents start to cross the matrix, shielding its interior from the magnetic field as it is shown in figure 4.10 for $f = 200\,\mathrm{Hz}$. Observe that the field in the normal matrix decreases from the exterior to the inner part (figure 4.10.(a)). Note that almost all the current is now flowing in the same direction through the superconductor. Only in the inner part there is a small portion of current returning (figure 4.10.(b)).

The decrease of the magnetic field in the normal matrix with increasing frequency is observed plotting the magnetic field along the y-axis as in figure 4.11. The field in the normal matrix region is constant, reducing with increasing the frequency and being almost zero for a very high frequency ($f = 160\,\mathrm{Hz}$). Observe in the superconducting part the linear profiles with constant slope similarly to Bean's model predictions (See section 1.5.2).

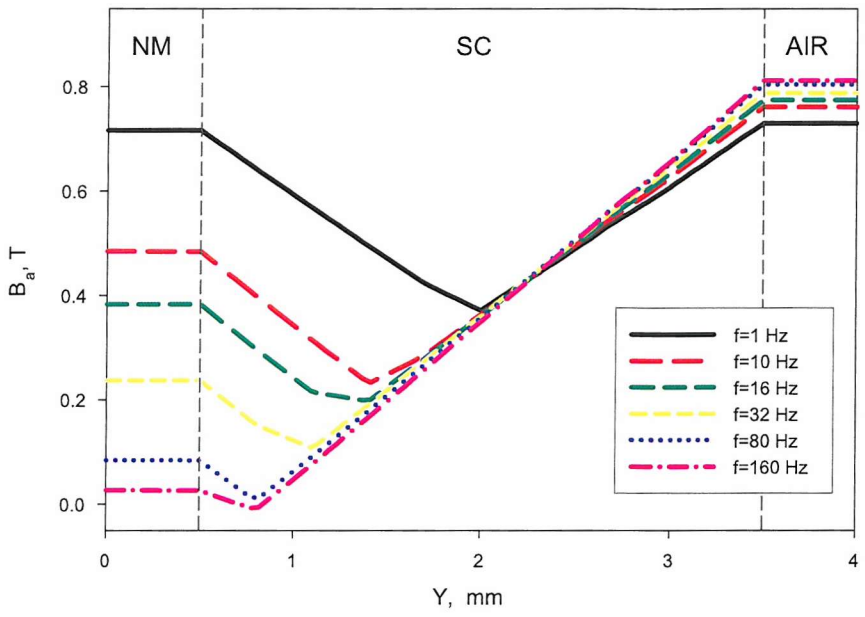

Figure 4.11: Magnetic field along y-axis for a slab at $\mu_0 H_a = 0.7\,\mathrm{T}$ and for different frequencies.

4.3.2 Strip

For studying the strip geometry consider superconductors of width $a = 3\,\mathrm{mm}$, height $b = 1\,\mathrm{mm}$, and length $l = 20\,\mathrm{mm}$ separated by a normal matrix of width $w = 0.5\,\mathrm{mm}$. The applied field has an amplitude $\mu_0 H_a = 0.7\,\mathrm{T}$ which is high enough to penetrate the strips completely at the peak field.

In perpendicular geometry demagnetization effects have to be taken into account. For the uncoupled example, figures 4.12 and 4.13 show the situation of two isolated strips similar to the one described for the slab. For a high frequency, $f = 160\,\mathrm{Hz}$, (figures 4.14 and 4.15) the superconductors are fully coupled with current flowing through the matrix and the inner part of the normal matrix shielded from the external field.

Observe in the field profile in the xy-plane (figure 4.16) the demagnetization effect. The field in the air and matrix regions increases as it approaches to the edges of the superconductor. Another difference observed respect to the slab is that the magnetic field increases in the borders from the back to the middle of the superconductor. In figure 4.16 it is seen that the field in the matrix decreases in the outer part but it

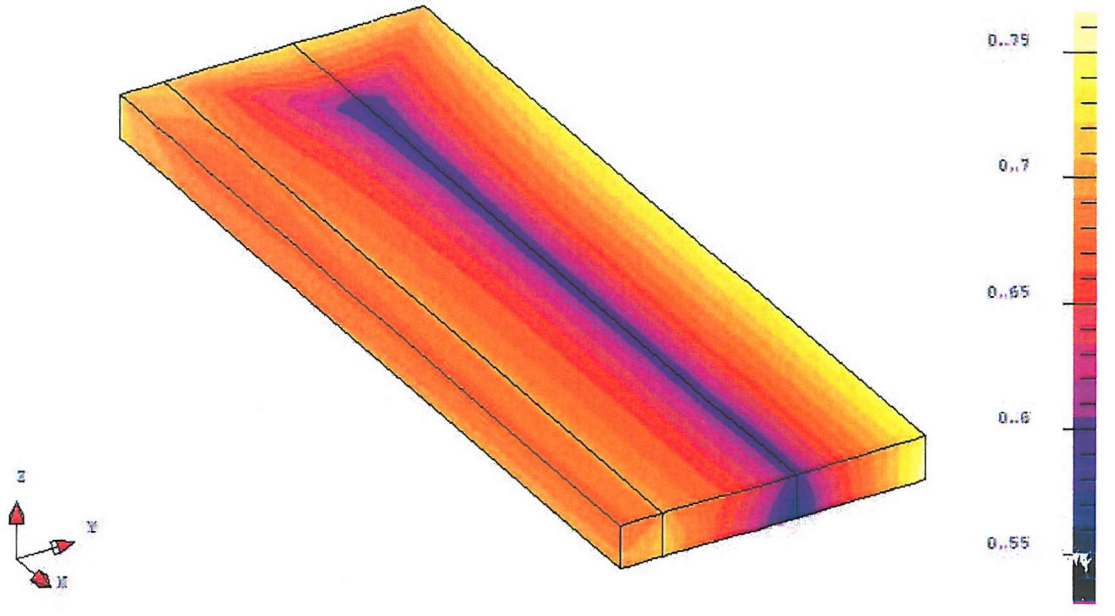

Figure 4.12: Magnetic field in strips at $\omega t = \pi/2$ for $\mu_0 H_a = 0.7\,\mathrm{T}$ and $f = 1\,\mathrm{Hz}$.

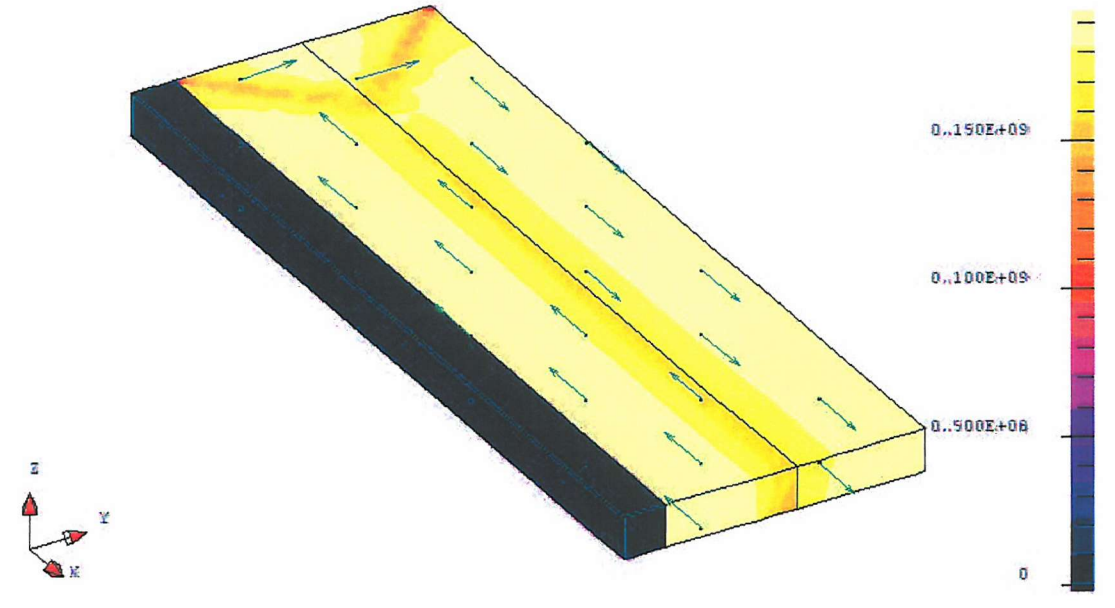

Figure 4.13: Induced current in strips at $\omega t = \pi/2$ for $\mu_0 H_a = 0.7\,\mathrm{T}$ and $f = 1\,\mathrm{Hz}$.

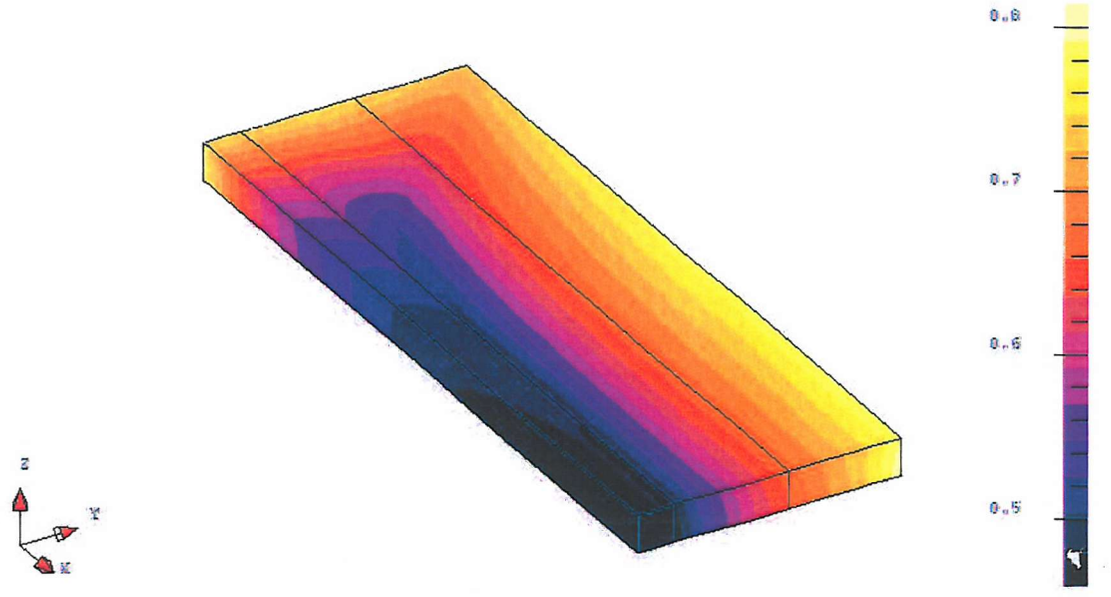

Figure 4.14: Magnetic field in strips at $\omega t = \pi/2$ for $\mu_0 H_a = 0.7\,\mathrm{T}$ and $f = 160\,\mathrm{Hz}$.

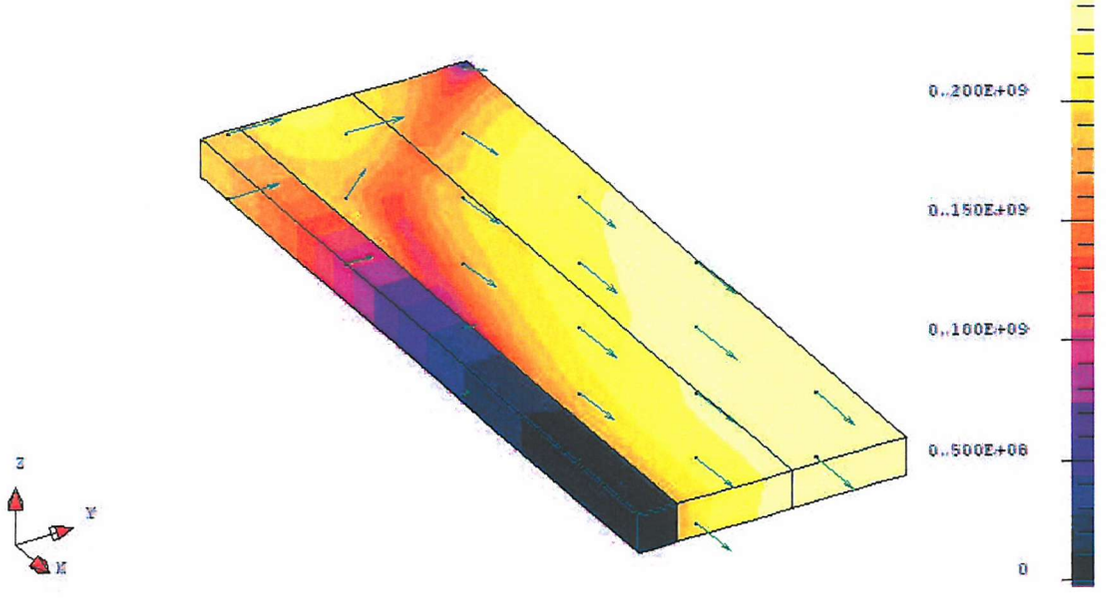

Figure 4.15: Induced current in strips at $\omega t = \pi/2$ for $\mu_0 H_a = 0.7\,\mathrm{T}$ and $f = 160\,\mathrm{Hz}$.

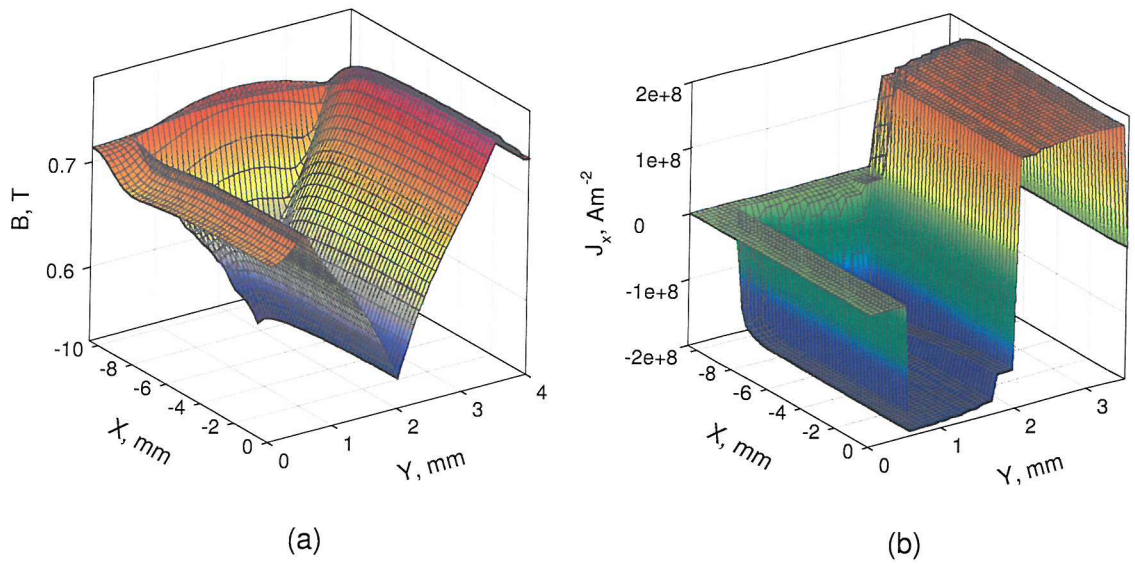

Figure 4.16: Magnetic field (a) and induced current (b) in strips at $\omega t = \pi/2$ for $\mu_0 H_a = 0.7\,\mathrm{T}$ and $f = 1\,\mathrm{Hz}$.

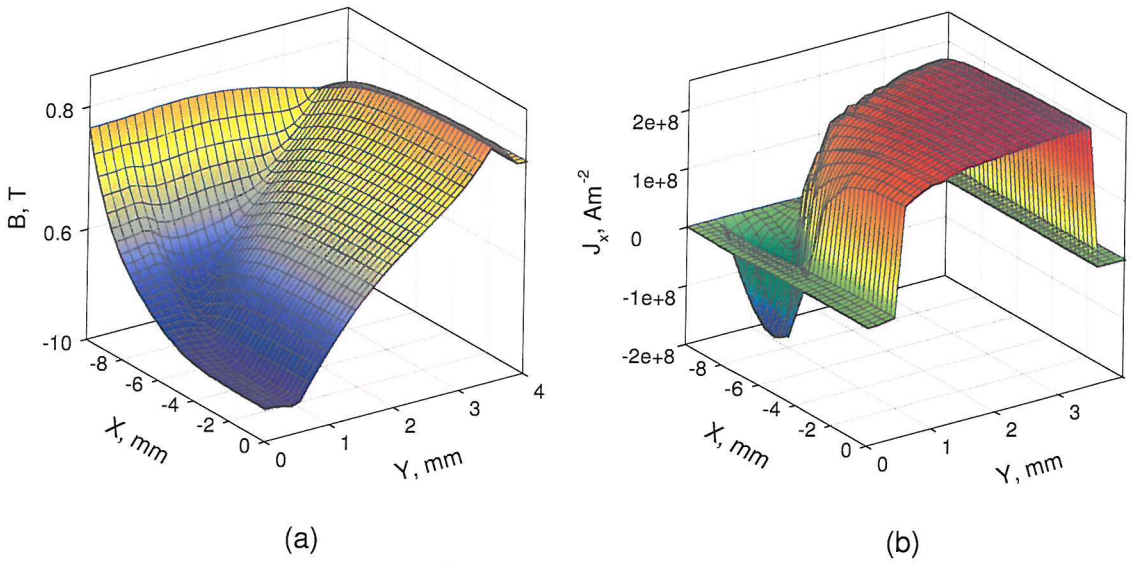

Figure 4.17: Magnetic field (a) and induced current (b) in strips at $\omega t = \pi/2$ for $\mu_0 H_a = 0.7\,\mathrm{T}$ and $f = 160\,\mathrm{Hz}$.

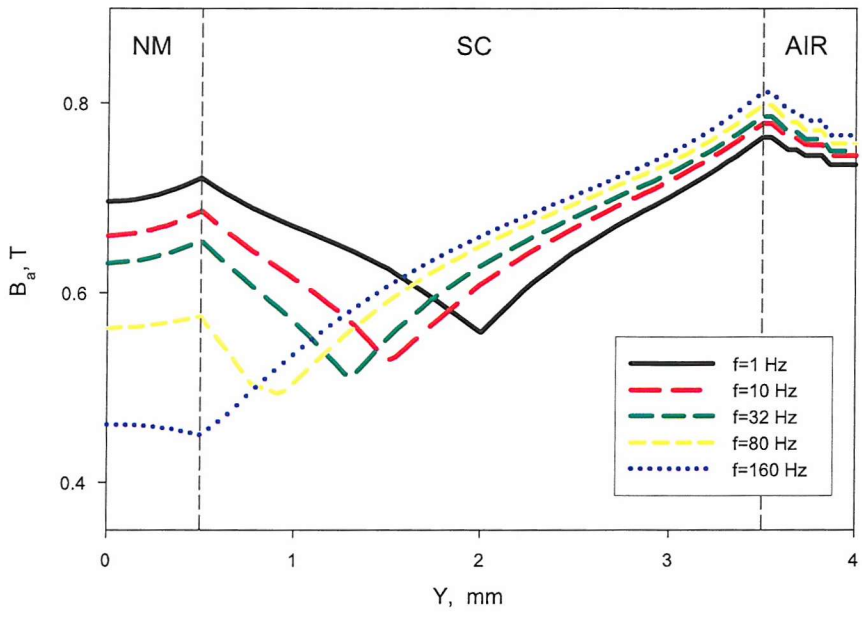

Figure 4.18: Magnetic field along y-axis for a strip at $\mu_0 H_a = 0.7$ and for different frequencies.

remains almost constant in the interior of the matrix region, a difference with the slab where the field decreases, due to coupling, gradually along the length.

The profile of the field along y-axis is shown in figure 4.18. The coupling increases with increasing frequency being the strips fully coupled for $f = 160\,\text{Hz}$ and the profile is similar to that of a strip of larger width $(2a + w)$. That is the reason of the higher value of the field in the right edge of the superconductor at high frequencies since it depends on the aspect ratio (a/b). Another particular characteristic of strips observed here is the non-linear profile of the field and its increment towards the edges of the superconductor similar to the analytical solutions given by Norris [25] for infinite long strips.

4.3.3 Evolution of the coupling current I_c

Although superconductors are made as filamentary composites to reduce hysteresis losses, with increasing f the coupling current between filaments raises considerably leading to high losses in the normal matrix. Therefore, for practical applications it is necessary to have a previous quantitative knowledge of the coupling phenomenon in order to develop strategies to keep the filaments uncoupled.

Numerical calculations are presented here for different frequencies of the sinusoidal applied field $\mu_0 H = \mu_0 H_a \sin(\omega t)$ including two different situations: small field amplitudes $\mu_0 H_a$ such that the superconductor is partially penetrated at the peak field ($\mu_0 H_a < \mu_0 H_p$), and for amplitudes higher that the total penetration field ($\mu_0 H_a \geq \mu_0 H_p$).

The coupling evolution through a whole field cycle time will be explained by examining two kind of quantities: the evolution of the coupling current calculated as $I_{coup} = \int_A \mathbf{J}_y(x, 0, z)\, \mathrm{d}A$, where A is the cross section of the normal matrix in the xz-plane, and the magnetic field integrated over the normal matrix region volume $B_m = \int_{V_m} \mathbf{B}_z(x, y, z)\, \mathrm{d}V_m$.

4.3.3.1 Slab

Results for the slab geometry are presented in figure 4.19 for partial penetration ($\mu_0 H_a = 0.1\mathrm{T} < \mu_0 H_p$). The amplitude of the coupling current (figure 4.19.(a)) increases with frequency as it is expected. At low frequencies the maximum coupling current is reached soon since is more determined by the decay of $\mathrm{d}B/\mathrm{d}t$, however, with increasing f the peak moves to the right becoming sinusoidal. Observe that for $f = 160\,\mathrm{Hz}$ the coupling current profile is in phase with the applied field, and its maximum corresponds to the total current flowing in the slab. The different amplitudes of the current profiles at different frequencies are observed in more detail in figure 4.19.(b). Notice that when the applied field returns to zero at $\omega t = \pi$ and $\omega t = 2\pi$ there is coupling current in the opposite direction.

The magnetic field in the normal matrix is represented in figure 4.19.(c). Observe that when the slabs are uncoupled at a low frequency, the field in the normal matrix follows a similar profile to the sinusoidal applied field one (shown in the figure with black line). Notice that its maximum value for $f = 1\,\mathrm{Hz}$ is higher than the amplitude of the applied magnetic field $\mu_0 H_a$ due to demagnetization effects. With increasing f the peak value reduces and moves to the right since the slabs become more coupled and the interior of the normal matrix is initially shielded from the external field, up to $\omega t = \pi/2$ and trapped upon field reductions. At $\omega t = \pi, 2\pi$, although the applied field has returned to zero there is still some field trapped in the matrix.
The field profile along y-axis is shown in figure 4.21 at $\omega t = \pi$ when the applied field has returned to zero. For low frequencies ($f = 1\,\mathrm{Hz}$) there is not coupling, hence the superconductors behave as two isolated ones and the field profile is equal in both edges

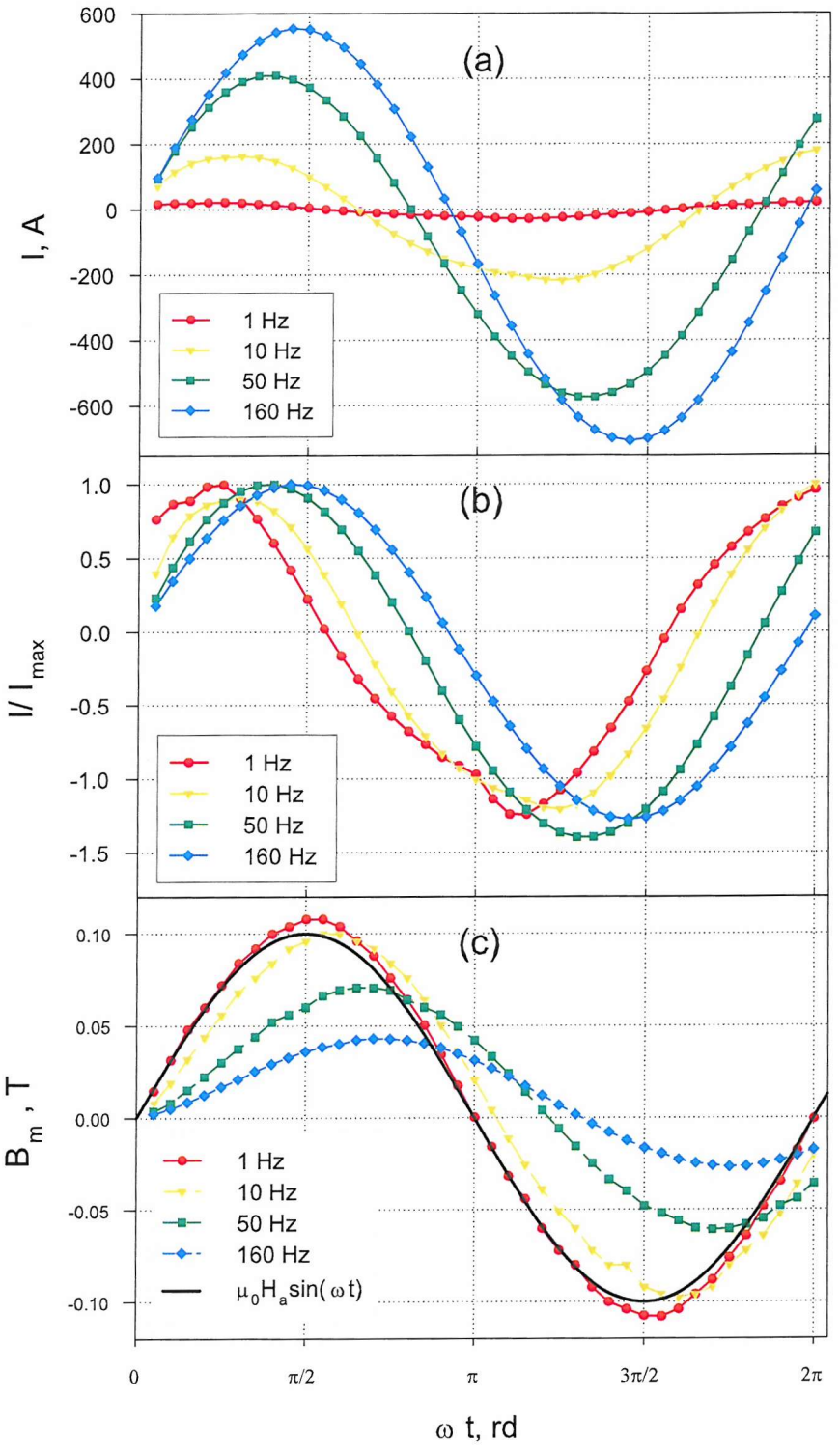

Figure 4.19: Coupling current (a) and magnetic field in the normal matrix (c) for a slab during a cycle time of an applied field of amplitude $\mu_0 H_a = 0.1\,\mathrm{T}$. For comparison at different frequencies, the coupling current is divided by its maximum (b).

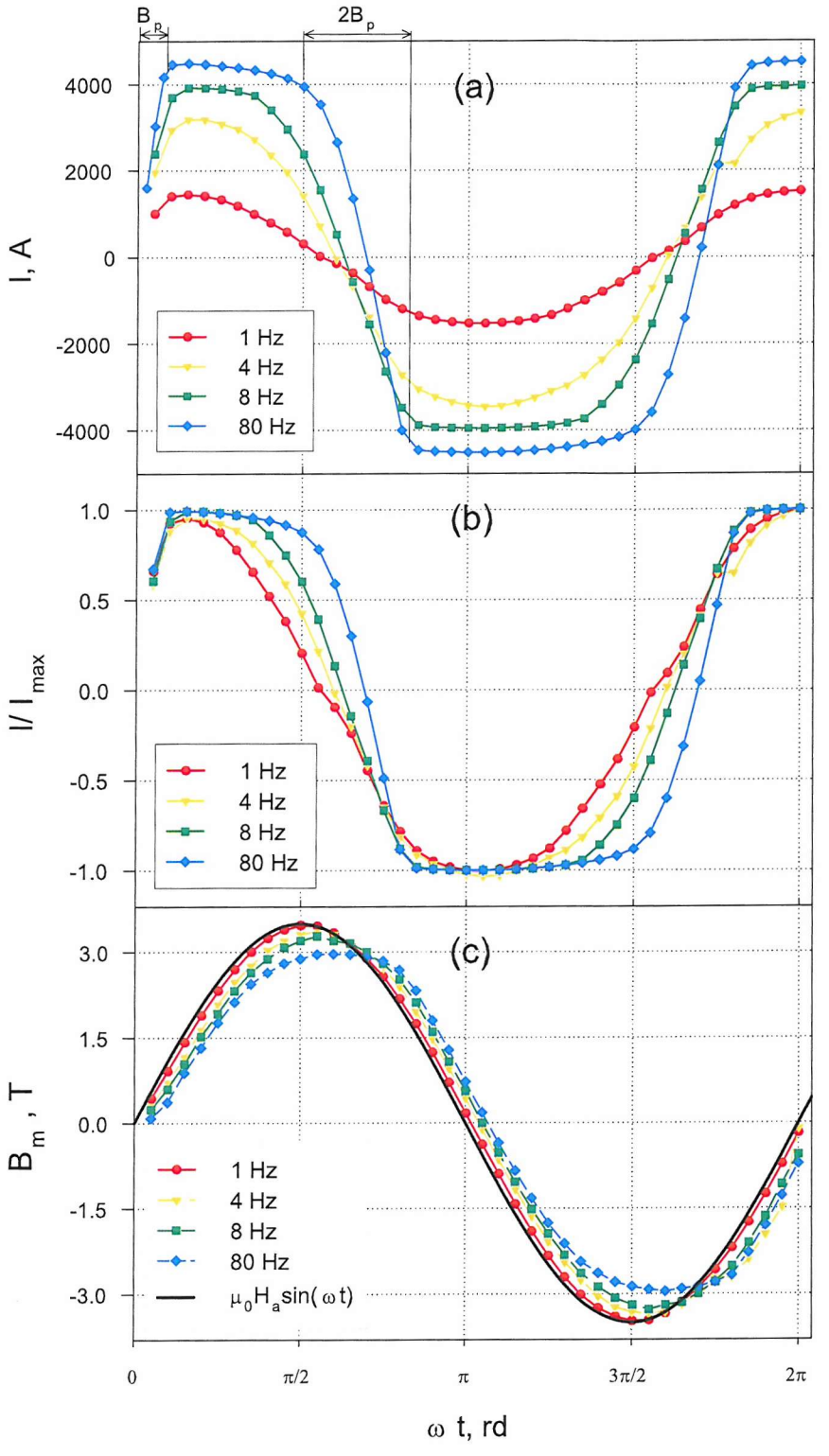

Figure 4.20: Coupling current (a) and magnetic field in the normal matrix (c) for a slab during a cycle time of the applied magnetic field of amplitude $\mu_0 H_a = 3.5\,\mathrm{T}$. For comparison at different frequencies, the coupling current is divided by its maximum (b).

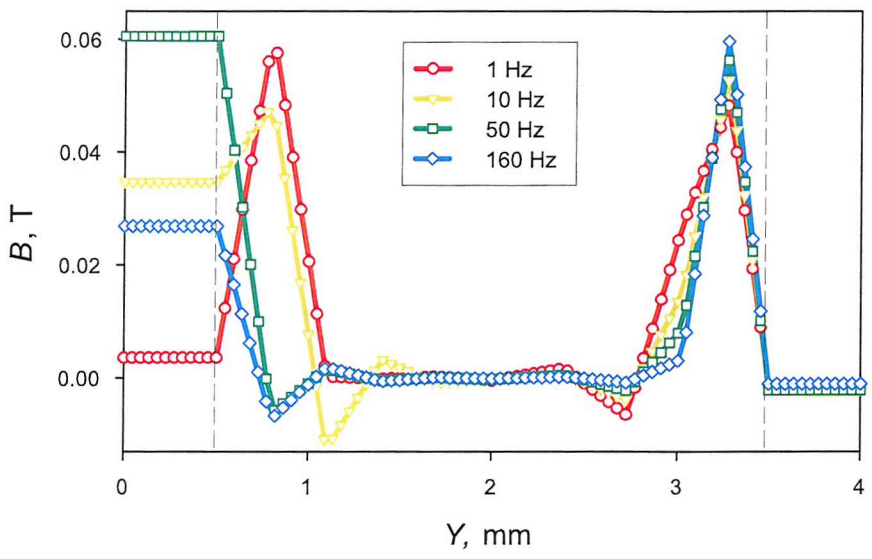

Figure 4.21: Magnetic field profiles along y-axis in the center of the slab at $\omega t = \pi$ for $\mu_0 H_a = 0.1\,\mathrm{T}$.

of the superconductor similar to the expected by Bean critical state model. However at higher f the field in the normal matrix does not return to zero since is trapped. Notice that the field in the matrix does not change monotonically with frequency.

For saturated slabs ($\mu_0 H_a = 3.5\,\mathrm{T} > \mu_0 H_p$) the results are shown in figure 4.20. Similarly to the partial penetration situation the coupling current increases with frequency. However the coupling current saturates quickly, and then decreases faster to the negative minimum upon field reduction. For very high frequencies, when the slabs are totally coupled, the coupling current reaches the maximum I_c at $\mu_0 H_a = \mu_0 H_p$ and continues almost constant until the field peak $\mu_0 H = \mu_0 H_a$ at $\omega t = \pi/2$. When the applied field is reduced, the coupling current decreases and reaches the minimum exactly when the applied field has been decreased $2\mu_0 H_p$ T.
At lower frequencies, the coupling current does not reach the maximum coupling current because the slabs are only partially coupled, and starts to decrease just after the peak determined by $\mathrm{d}B/\mathrm{d}t$. Notice that, although the peak of the coupling current moves to the right with increasing frequency, for very high values ($f = 80$) the coupling current saturates before. In figure 4.20.(b) observe that at $\omega t = \pi$ and $\omega t = 2\pi$ the coupling current is maximum a difference with the partial penetrated slabs.

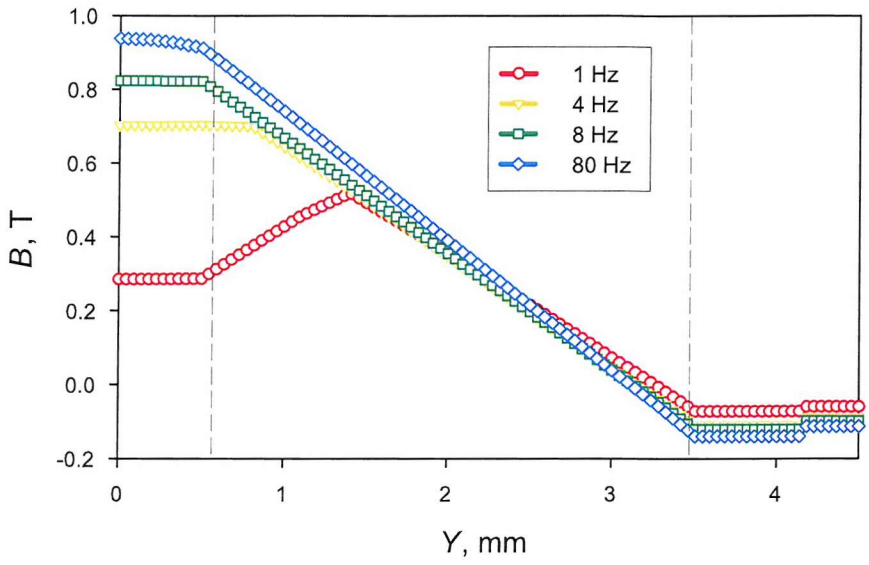

Figure 4.22: Magnetic field profiles along y-axis in the center of the slab at $\omega t = \pi$ for $\mu_0 H_a = 3.5\,\mathrm{T}$.

The field in the normal matrix is shown in figure 4.20.(c). As for the partial penetration situation, the field follows the same profile as the applied field for low frequencies, but as f is increased the peak is reached later and there is some field trapped at $\omega t = \pi, 2\pi$. A difference from the partial penetrated situation is that the profiles do not vary much for different f since after full penetration even for high fields the minimum field is $\mu_0 H_a - \mu_0 H_p$, and when the field decreases to zero again, the maximum trapped flux is $\mu_0 H_p$. Observe this fact in the field profile along y-axis at $\omega t = \pi$ (figure 4.22). Notice that the field in the normal matrix increases with frequency.

4.3.3.2 Strip

For the strip, the evolution of the coupling current at $B_a = 0.15\,\mathrm{T}$ is similar to the one for partially penetrated slabs as it is observed in figure 4.23. The coupling current increases with frequency becoming sinusoidal for higher f (figures 4.23.(a), 4.23.(b)). Respect to the field in the normal matrix, similarly to partially penetrated slabs at low frequencies the profile follows the same profile at the applied field and reduces with increasing f, being finite when the applied field reduces to zero.

The plot of the field along y-axis (figure 4.24) shows clearly the field trapped at $\omega t = \pi$. As a consequence of the demagnetization effect in strips the field in the right

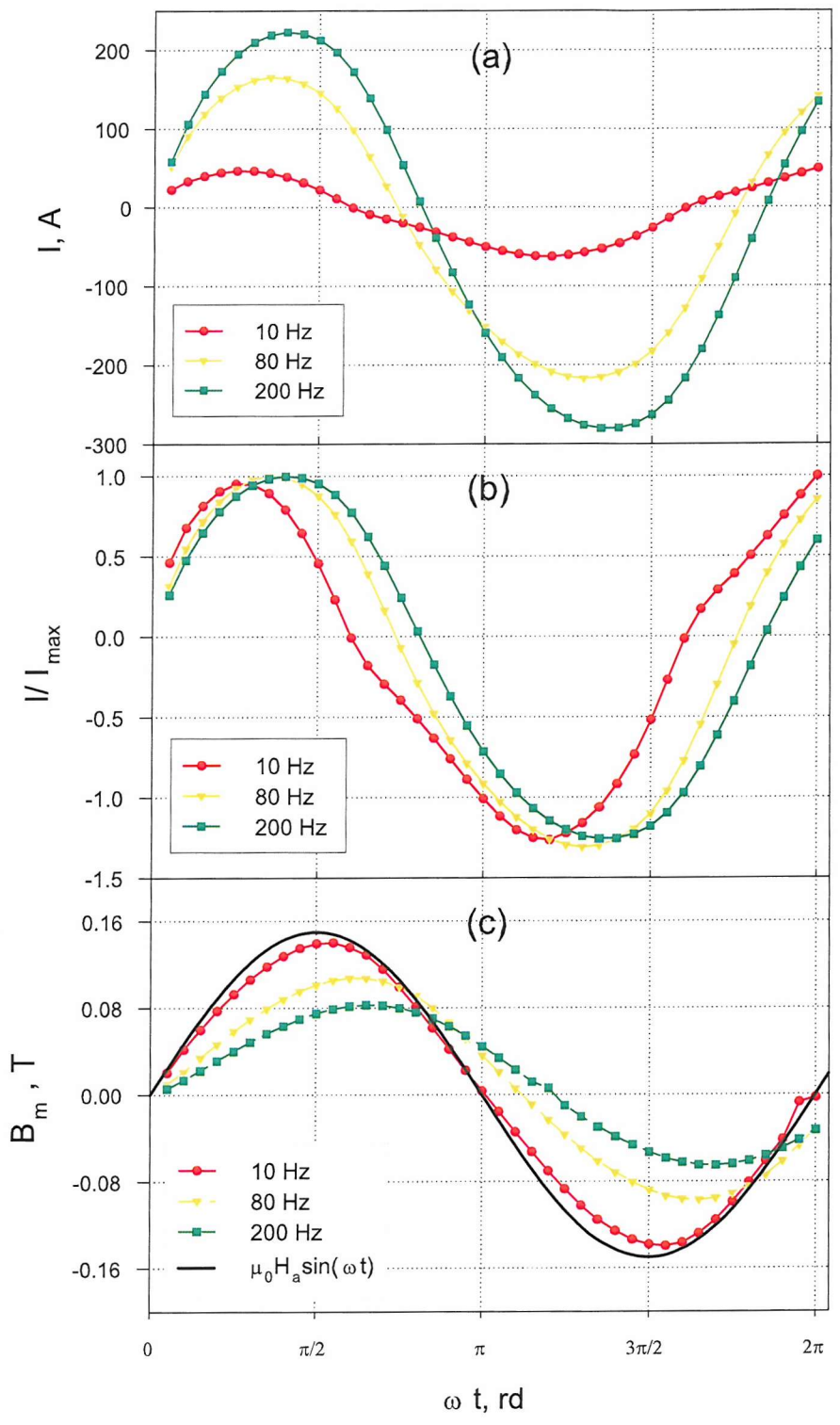

Figure 4.23: Coupling current (a) and magnetic field in the normal matrix (c) for a strip during a cycle time of the applied magnetic field of amplitude $\mu_0 H_a = 0.15\,\mathrm{T}$. For comparison at different frequencies, the coupling current is divided by its maximum (b).

edge is lower than the applied field. Observe that the field in the normal matrix increases with frequency and changes the slope at very high frequencies.

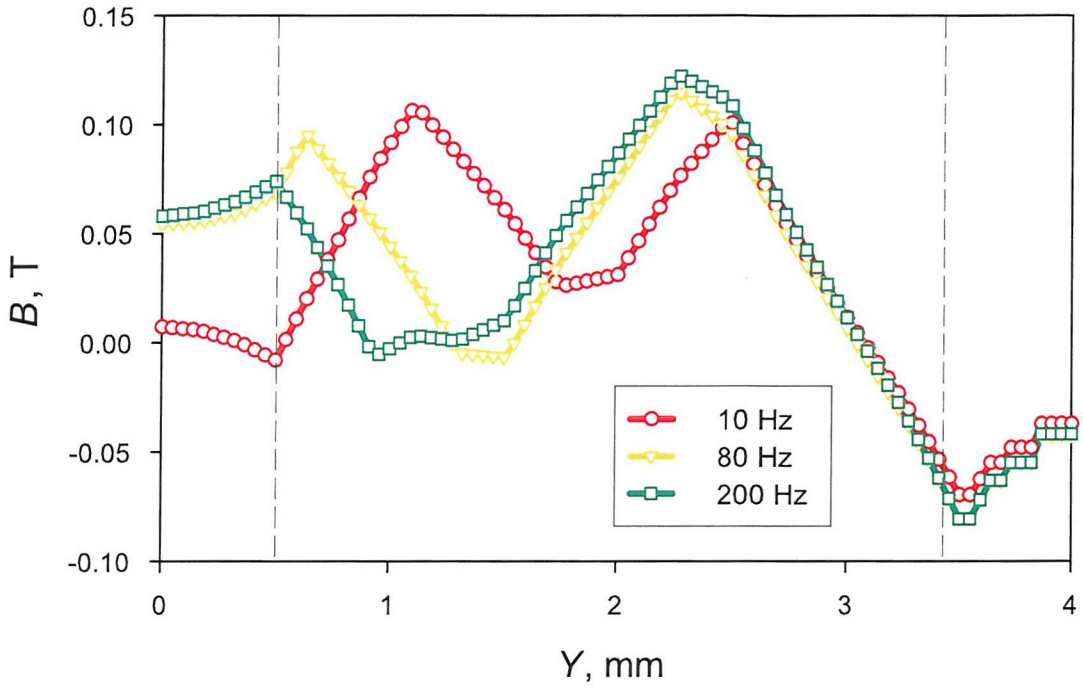

Figure 4.24: Magnetic field profiles along y-axis in the center of the strip at $\omega t = \pi$ for $\mu_0 H_a = 0.15\,\mathrm{T}$.

4.3.4 Coupling current and f_c

The only existing theory of the coupling effect is given for two saturated infinite slabs under the assumptions of Bean's model. For such geometry there is a critical ramp rate of the magnetic field $\dot{B}_c = 2a\rho J_c/l^2$ such that the superconductors are totally coupled [41].

For other geometries and in the case of partial penetrated superconductors numerical predictions are necessary. In this section a quantitative approximation of the coupling effect will be given for finite strips and slabs.

So far the evolution of the coupling current was analyzed during a whole cycle time and for different frequencies of the applied field. Now for a fixed ωt, the increment of

the coupling current with increasing frequency is observed in order to obtain the critical frequency f_c indicating the onset of coupling, for a given amplitude $\mu_0 H_a$.

The coupling current is shown as a function of f for different $\mu_0 H_a$ at $\omega t = \pi/4$ in figures 4.25.(a) and 4.26.(a) for the slab and strip respectively. Similarly for both geometries, for a given amplitude B_a the coupling current increases with increasing frequency and saturates when the superconductors are totally coupled and the maximum current flowing through the superconductor is crossing the matrix.

The critical frequency f_c may be considered as the frequency at which the coupling current curves change the slope to become flat. The peaks of the curves indicated by the arrows in figures 4.25.(b) and 4.26.(b) correspond to such values. Observe that for high fields the coupling starts before, that is, at a lower f. Notice that for strips the peak at the same field, $\mu_0 H_a = 0.3\,\mathrm{T}$, is reached later than for the slabs indicating that the coupling starts at a higher f.

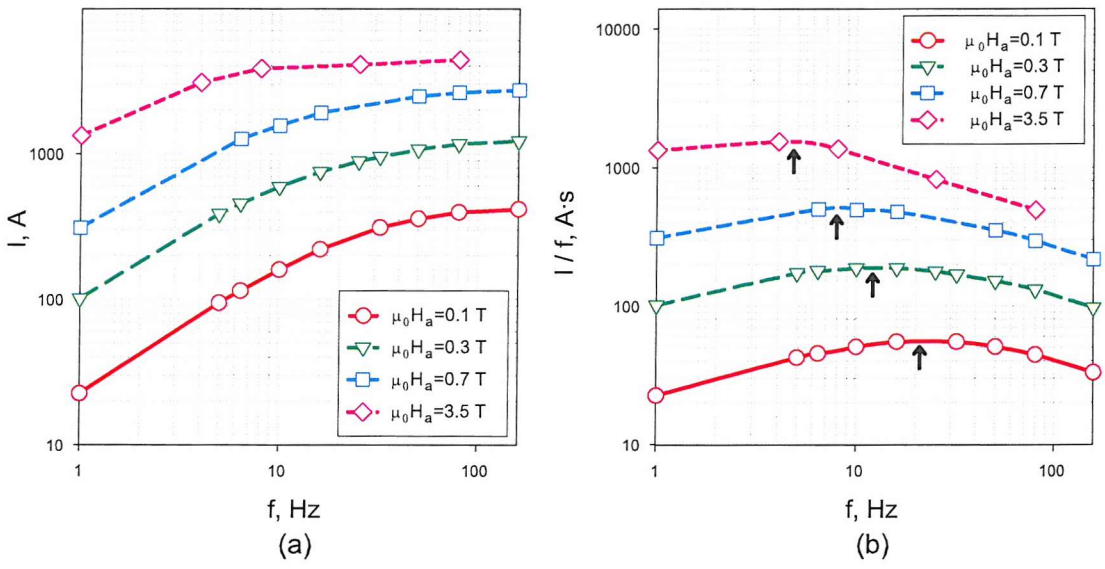

Figure 4.25: Coupling current for different frequencies (a) and approximated value of the critical coupling frequency f_c (b) for the slab geometry.

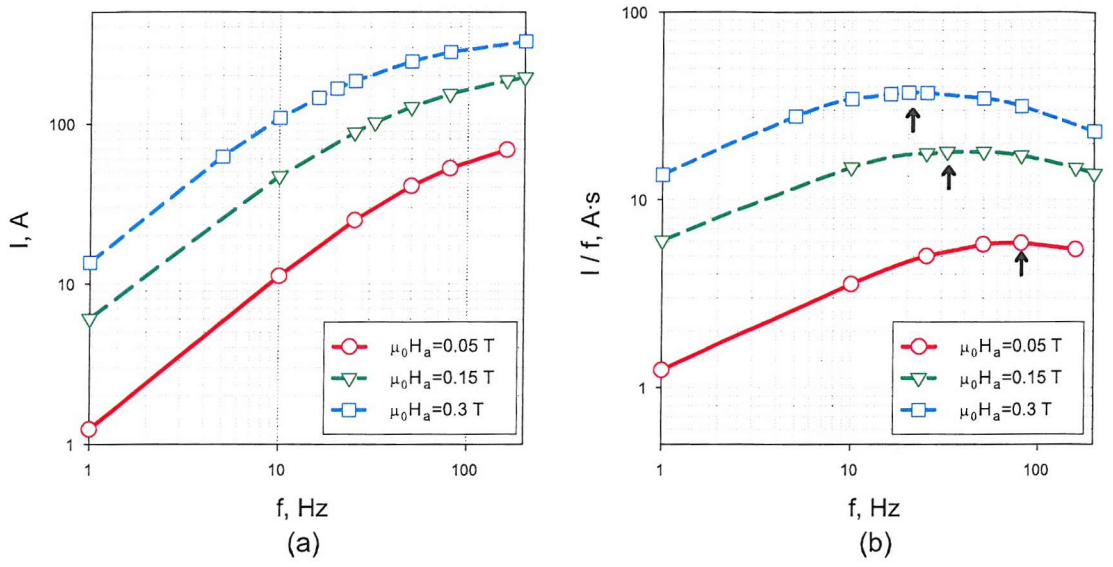

Figure 4.26: Coupling current for different frequencies (a), and approximated value of the critical coupling frequency f_c (b) for the strip geometry.

4.4 Constant ramp rate $\dot{B}$

As it was seen in previous section, in sinusoidal applied fields the evolution of the coupling current has to be analyzed having into account not only the change in time of B but also the variation of $\mathrm{d}B/\mathrm{d}t$, which makes it more complex. In this section the coupling effect between superconductors is studied when a external magnetic field is applied and raised with a constant ramp rate $\mu_0 H_a(t) = \mu_0 \dot{H}_a t$.

The model consists on 2 finite superconductors joined by a normal matrix. Three different geometries are considered : the slab, the strip and the square superconductor. The width of the superconductor is $2a = 1.4\,\mathrm{mm}$ and the length is $l = 8\,\mathrm{mm}$. For the slab the height is $b = 10\,\mathrm{mm}$ and for the strip is $b = 0.1\,\mathrm{mm}$. The width of the normal matrix is $w = 0.15\,\mathrm{mm}$. The physical properties are given by the parameters: $J_c = 10^8\,\mathrm{Am}^{-2}$, $E_c = 10^{-4}\,\mathrm{Vm}^{-1}$ and $n = 21$.

It is known by theory that superconductors with different aspect ratios (a/b) have different field and current profiles and therefore a different coupling behavior is expected. Figure 4.27 shows those differences due to the demagnetization effects in the field profiles along y-axis at $z = x = 0$. It is clear the non-linear profile of the field in the strip similar to that calculated analytically for infinite flat superconductors, and the linearity in the

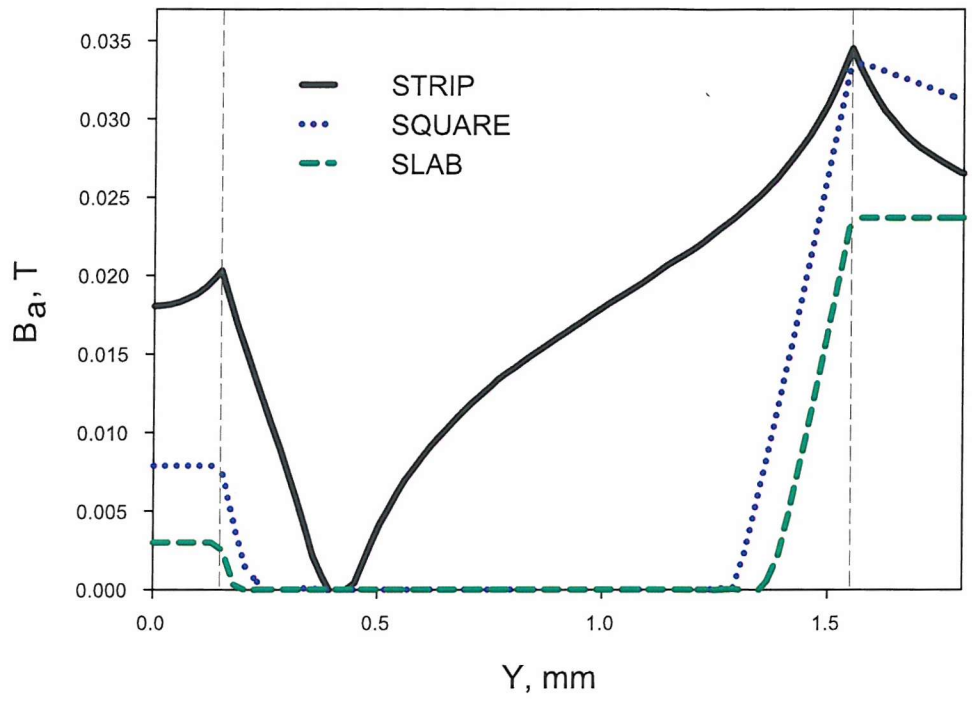

Figure 4.27: Magnetic field profiles in superconductors of different aspect ratio in an external field ramping at $\dot{B}_a = 10\,\mathrm{Ts}^{-1}$ to $\mu_0 H = 0.02\,\mathrm{T}$.

case of the slab analogous to the profiles of Bean's model for infinite slabs. In the slab geometry the magnetic field is equal in the whole air region whereas for the square and the strip the field increases at the superconductor's edges reaching a higher value for the strip. Another difference due to the different aspect ratios is the penetration depth. At $B_a = 0.02\,\mathrm{T}$ the strip is fully penetrated whereas the square is only partially penetrated and in the slab the penetrated area is even smaller.

Observe in figure 4.27 that the field in the normal matrix part has decreased more in the slab geometry than in the square or the strip, which are more penetrated at the same applied field and for the same ramp rate, indicating the influence of the penetration depth on the critical coupling field rate $\dot{B}_c$.

In order to obtain the critical coupling field rate $\dot{B}_c$, calculations were carried out increasing the applied field beyond full penetration at different ramp rates. In this section $\dot{B}_c$ is defined as the ramp rate for the onset of total coupling, that is, when all the current

flowing in one superconductor crosses the normal matrix.

$\dot{B}_c$ is plotted in figure 4.28 for the three geometries. The critical coupling field $\dot{B}_c$ in the slab (figure 4.28.(a)) increases linearly with the applied field to reach a maximum just before full penetration field. At higher fields beyond full penetration, $\dot{B}_c$ decreases to a constant value equal to $25\,\mathrm{Ts}^{-1}$.

For the square (figure 4.28.(b)) a similar profile is found. As for the slab, the peak ($\dot{B}_c = 400\,\mathrm{Ts}^{-1}$) is reached just before full penetration, and then decreases to a value $31\,\mathrm{Ts}^{-1}$ higher than that obtained for the slab at saturation fields.

Figure 4.28.(c) shows $\dot{B}_c$ for the strip. A difference with the other two geometries, $\dot{B}_c$ increases slowly with the applied field, and after total penetration reduces slightly to a constant value in contrast to the pronounced decrease for the other two geometries.

In order to compare the three cases in figure 4.28.d the curves are plotted all together as a function of the penetration depth. Observe that the strips couple faster al low fields, however when the superconductors are saturated, the critical field ramp rate is more than double of those for the square and the slab, which has the lowest $\dot{B}_c$.

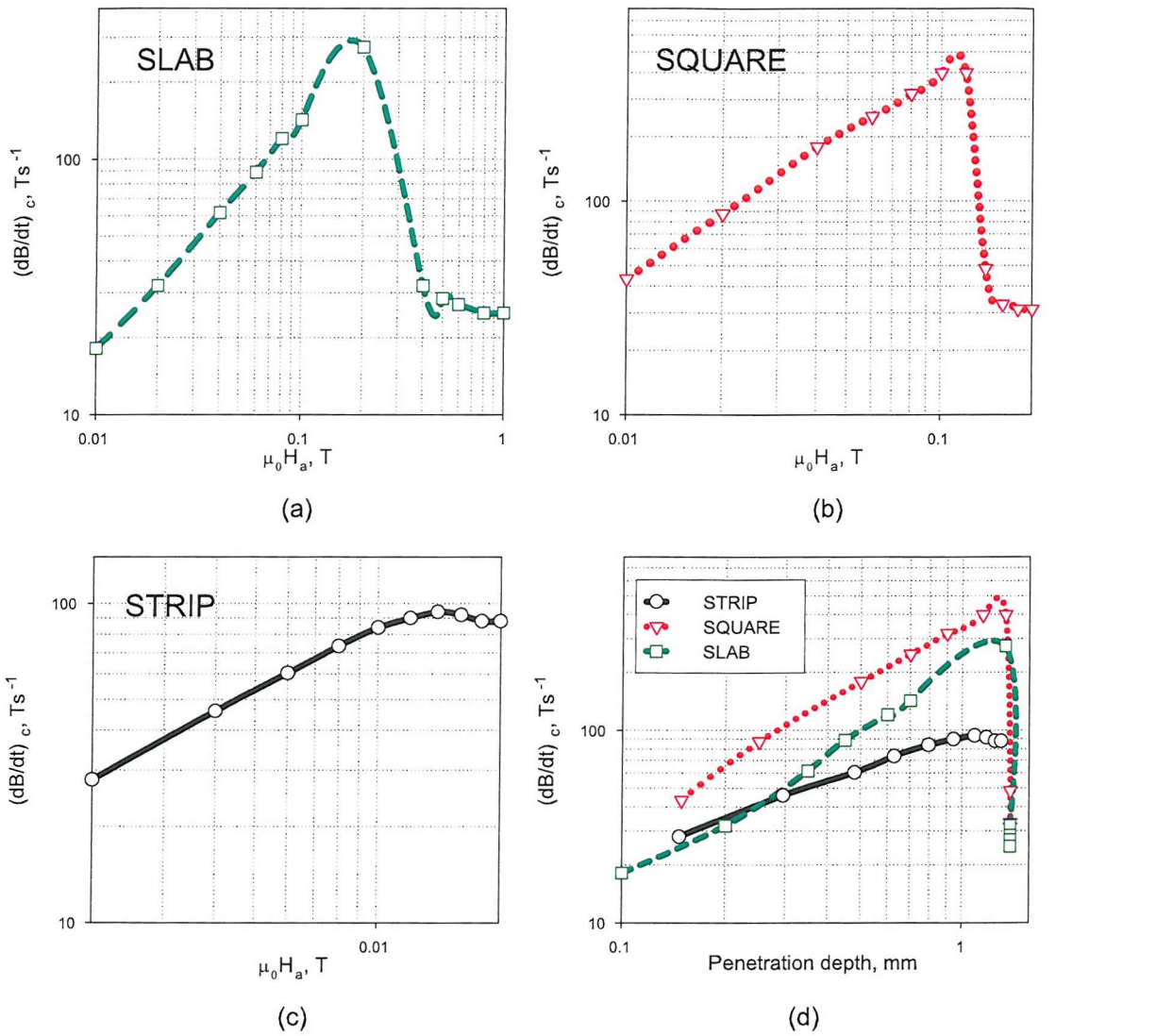

Figure 4.28: Critical coupling field rate $\dot{B}_c$ for slab (a) square (b) and strip (c) superconductors and as a function of the applied field. The corresponding $\dot{B}_c$ is shown in (d) as a function of the flux penetration depth.

4.5 Limitation to implementation of $E-J$ power law in Flux3D formulation.

In HTS the $\mathbf{J}(\mathbf{E})$ property can be described by the power law:

$$\mathbf{E} = E_c \left(\frac{|\mathbf{J}|}{J_c}\right)^{n-1} \frac{\mathbf{J}}{J_c} \tag{4.2}$$

The non-linear resistivity of the superconductor is given in Flux3D formulation by $\rho = \rho_1 + \rho_0$, where

$$\rho_1(|\mathbf{E}|) = \frac{1}{\sigma_1(|\mathbf{E}|)} \tag{4.3}$$

with

$$\sigma_1(|\mathbf{E}|) = \frac{J_c}{E_c^{1/n}} |\mathbf{E}|^{1/n-1} \tag{4.4}$$

and ρ_0 is a resistivity added to the resistivity ρ_1 in order to avoid $\frac{\partial|\mathbf{J}|}{\partial|\mathbf{E}|} = \infty$ for $|\mathbf{E}| = 0$. This additional resistivity ρ_0 may be interpreted from a physical point of view as the thermally activated resistance at 77 K.

The current density J is written as a function of the electric field E as

$$|\mathbf{J}| = \frac{|\mathbf{E}|}{\frac{E_c^{(1/n)}}{J_c} |\mathbf{E}|^{(1-1/n)} + \rho_0} \tag{4.5}$$

When $|\mathbf{E}| \approx 0$, then $|\mathbf{J}| \approx \frac{1}{\rho_0}|\mathbf{E}|$

and for $|\mathbf{E}| \gg 0$, $|\mathbf{J}| \approx J_c \left(|\mathbf{E}|/E_c\right)^{1/n}$

This $E-J$ relation is shown in figure 4.29 for different values of ρ_0. Notice that the value $\rho_0 = 10^{-13}$ is too large and for $\rho_0 = 10^{-14}$ and $\rho_0 = 10^{-15}$ the curves do not differ much.

The non-linear formulas in Flux3D are solved using the Newton Raphson method. For a good convergence of the iterative process is very important to choose an appropriate value of ρ_0. Solution for the magnetic field and density current are shown in figure 4.30 for different ρ_0 . The plots represent the profiles along the y-axis at $z = 0$ and $x = 0$. Observe the wrong profiles for large values of the resistivity $\rho_0 \approx 10^{-10}, 10^{-11}, 10^{-12}\,\Omega$m.

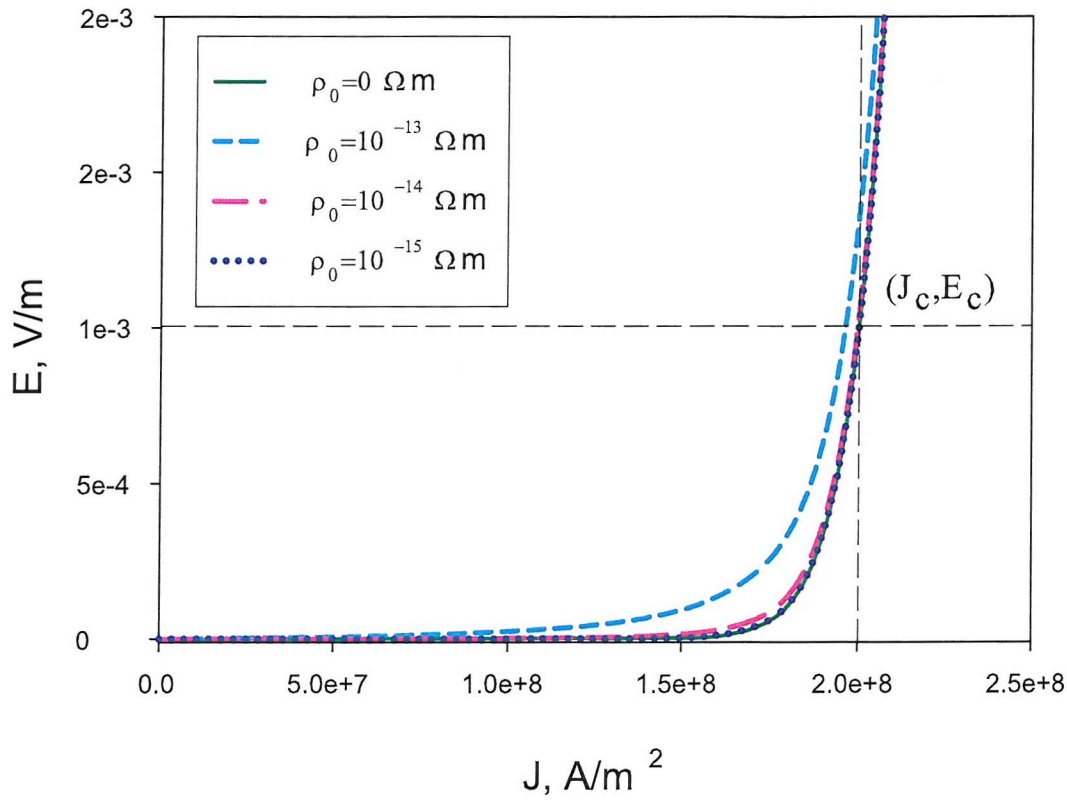

Figure 4.29: $E - J$ law with $J_c = 2 \times 10^8\,\mathrm{A/m^2}$, $E_c = 10^{-3}\,\mathrm{V/m}$ and $n = 21$, varying the initial resistivity ρ_0.

The value of ρ_0 depends on the parameters J_c, E_c and n of the material. The optimal value is determined by $\rho_0 \leq 10^{-2} E_c/J_c$ ([34]).

In old versions of flux3D the definition of $\mathbf{J}(\mathbf{E})$ is characterized by the conductivity instead the resistivity value $\sigma(|\mathbf{E}|) = \frac{1}{\rho(|\mathbf{E}|)}$. The initial conductivity is then required $\sigma_0(|\mathbf{E}|) = \frac{1}{\rho_0(|\mathbf{E}|)}$. In calculations with such characteristic $\sigma_0 = 10^9\,\mathrm{S/m}$ was enough for a good convergence. Observe in figure 4.30 that the result obtained for this value of σ_0 is similar to those calculated using the resistivity with $\rho_0 \ll 10^{-9}\,\Omega\mathrm{m}$.

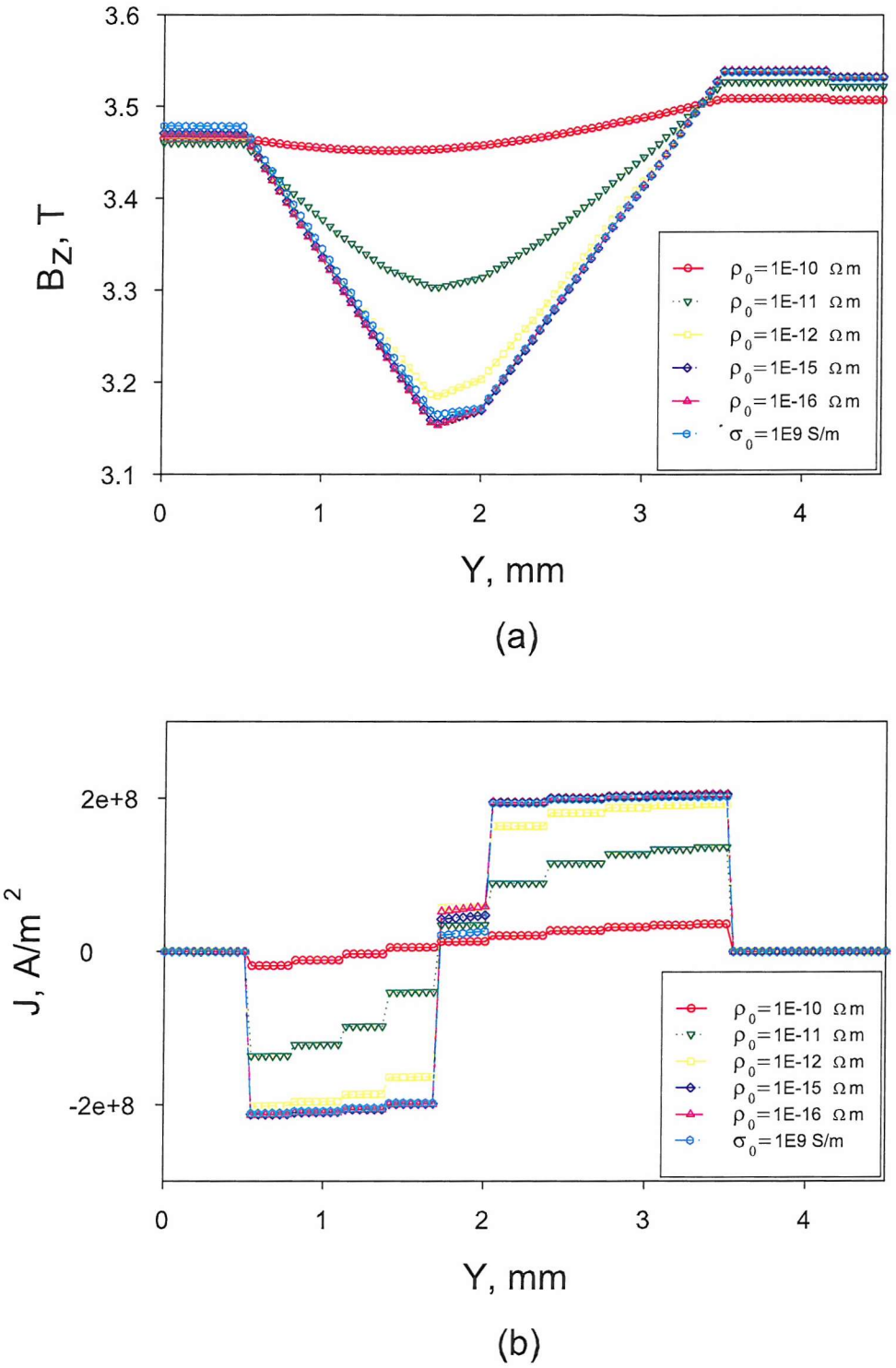

Figure 4.30: Influence of ρ_0 in the profile of the magnetic field (a) and current density (b) at $\omega t = \pi/2$ for $\mu_0 H_a = 3.5\,\mathrm{T}$ and $f = 1\,\mathrm{T}$.

4.6 Conclusion

In this chapter the FEM software Flux3D was utilized to model the coupling effect between superconductors when they are in presence of an external applied magnetic field.

Differences in the current and field profiles for slabs and strips due to demagnetization effects were found as expected, probing the capability of the FEM method for 3D modelling.

Under a sinusoidal magnetic field the increment of the coupling current with increasing the frequency f was observed. The evolution of the coupling current through a cycle time was explained for strips and slabs at different applied fields. An approximation to the critical coupling frequency f_c for the onset of coupling was given for different field amplitudes. It was observed in both slab and strip geometries, that increasing $\mu_0 H_a$ the coupling starts at a lower f .

At the end of the chapter the coupling effect was investigated for slabs, strips and square superconductors in an applied field with constant ramp rate. The critical coupling field $\dot{B}_c$ was given at different values of the applied field including from low penetration to saturation. For the slab and the square superconductor it was found a strong dependence of $\dot{B}_c$ on the applied field. For such geometries $\dot{B}_c$ increases with $\mu_0 H_a$ to a maximum at the field of total penetration $\mu_0 H_p$ and then decreases to a constant. However, in the strip $\dot{B}_c$ increases slower with $\mu_0 H_a$ and after having reached total penetration there is only a small decrease to a constant. Below partial penetration the strips couple before than the slab and square superconductors, however when they are saturated the total coupling starts before in the slabs.

Chapter 5

2D Modelling of coupling between superconductors of finite length

5.1 Introduction

Minimization of AC losses in high temperature superconductors is one of the main task required for their application in electric power devices. In order to reduce the hysteresis losses and have better stability properties, superconductors are made of thin filaments imbedded in a normal matrix. Such strategy is only effective if the filaments remain uncoupled when the applied field is changed at a sufficiently slow ramp rate. However when the ramp rate of the field is increased, the field penetrated into the matrix produces an emf which can drive the current through the normal matrix. There is a critical ramp rate of the applied field such that the emf is sufficient to drive the critical current of all the filaments across the normal matrix and, therefore, in terms of ac losses the multifilamentary superconductor behaves as a single larger one [38, 41].

In spite of conceptual understanding of the coupling phenomenon, theoretical prediction for critical coupling field rate is limited to the case of fully saturated infinite slabs where demagnetization effects are negligible, whereas quantitative solution for the coupling effect is lacking between partially penetrated superconductors or with finite geometrical dimensions.

In chapter 4, finite element method software Flux3D [15] is demonstrated to be successfully applied for such problems. However integrations methods with simpler formulations such as Brandt's formulation for 2D models (see chapter 2) would be desirable

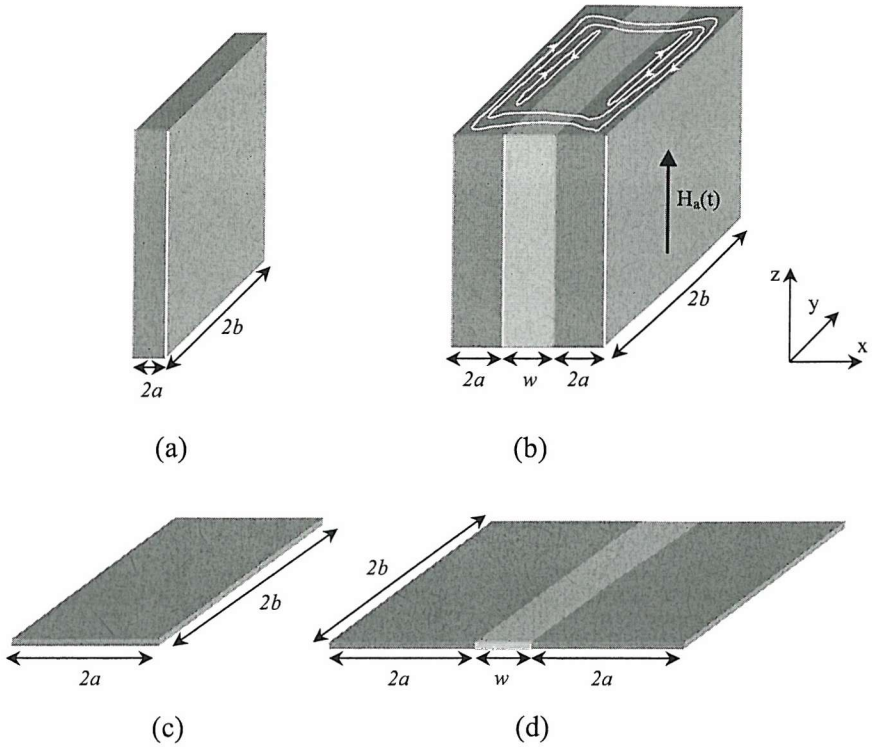

Figure 5.1: Geometry of the slab (a) and the thin disc (c). Model of a sandwich of two slabs (b) and two thin discs (d) with a normal matrix in between. The contour shown in (b) indicates the flow pattern of the induced current when the conductors are coupled.

for an easier and faster implementation. In this chapter extension of Brandt's formulation for the sheet current in thin finite superconductors [32, 8] is used to investigate the coupling effect. The formulation consists of the solution by time integration of a non-linear diffusion equation for the stream function of the induced sheet current g. In this way the 3D problem is reduced to a 2D problem and it is not necessary to take into account the boundary conditions.

The formulation is applied to the two limiting situations shown in figure 5.1, thin discs and infinite slabs, in order to obtain a quantitative understanding of the coupling between finite superconductors through a normal matrix (light grey region in figures 5.1.(b) and (d)). Results will be given not only for saturated superconductors but also, and for the first time, at applied fields that penetrate the superconductors only partially.

Calculations modifying some of the parameters such as the resistivity of the normal matrix, the critical density current or the distance between superconductors, were carried

out to investigate their influence in the coupling phenomenon. For all the cases an approximation of the critical field ramp rate $\dot{B}_c$ will be given.

At the beginning of this chapter, the formulation is explained and validated for isolated thin discs and infinite slabs. Then, the results for the coupling effect are discussed with the help of the field and current density profiles, comparing the two geometries and for different values of the parameters influencing the coupling effect.

5.2 Numerical formulation

The induced current in superconducting infinite slabs and thin discs of finite length in ac magnetic field is confined in the plane perpendicular to z along which the magnetic field is applied.

For an infinite slab, $\mathbf{J}(x,y)$ is independent of z since is the same everywhere along the direction of the applied field and can be expressed by a scalar function $g(x,y)$, the local magnetization, as

$$\mathbf{J}(x,y) = -\hat{\mathbf{z}} \times \nabla g(x,y) = \nabla \times \hat{\mathbf{z}} g(x,y) \tag{5.1}$$

The lines $g(x,y) = const$ are the streamlines of the current and div$\mathbf{J} = 0$ is guaranteed.

For a thin disc of thickness $d \ll a$, it is necessary to use the sheet current defined as $\boldsymbol{\sigma}(x,y) = \int_{-d/2}^{d/2} \mathbf{J}(x,y,z)\mathrm{d}z$. As $\boldsymbol{\sigma}(x,y)$ is independent of z, it can be expressed as $\boldsymbol{\sigma}(x,y) = -\hat{\mathbf{z}} \times \nabla g(x,y)$. When $d \to 0$, the sheet current density $\boldsymbol{\sigma}(x,y) = \mathbf{J} \cdot d = I/a \cdot d$ is finite and a defined critical sheet current density of $\sigma_c = I_c/a \cdot d$ for a given transport critical current I_c.

From Biot-Savart law the potential vector can be written for a current density $\mathbf{J}(x)$ as

$$\mathbf{H}(\mathbf{r}) = \mu_0^{-1} \nabla \times \left(\mu_0 \frac{1}{4\pi} \int \frac{\mathbf{J}(\mathbf{r}')}{|\mathbf{r} - \mathbf{r}'|} \mathrm{d}r' \right) = \frac{1}{4\pi} \int \nabla \frac{1}{|\mathbf{r} - \mathbf{r}'|} \times \mathbf{J}(\mathbf{r}') \mathrm{d}^2 r' \tag{5.2}$$

In the case of thin discs, the magnetic field at $\mathbf{r} = (x,y)$ generated by current loops lying in the xy-plane and centered at $\mathbf{r}' = (x',y')$ is obtained from (5.2) and (5.1) as

$$\begin{aligned}\mathbf{H}(\mathbf{r}) &= \frac{1}{4\pi}\int \nabla\frac{1}{|\mathbf{r}-\mathbf{r}'|}\times(\nabla'\times\hat{\mathbf{z}}g(\mathbf{r}'))\mathrm{d}^2r' \\ &= \frac{1}{4\pi}\int \nabla'\left(\hat{\mathbf{z}}g(\mathbf{r}')\cdot\nabla\frac{1}{|\mathbf{r}-\mathbf{r}'|}\right)-\hat{\mathbf{z}}g(\mathbf{r}')\left(\nabla'\cdot\nabla\frac{1}{|\mathbf{r}-\mathbf{r}'|}\right)\mathrm{d}^2r' \\ &= \hat{\mathbf{z}}\frac{1}{4\pi}\int g(\mathbf{r}')\cdot\left(\nabla\cdot\left(\nabla'\frac{1}{|\mathbf{r}-\mathbf{r}'|}\right)\right)\mathrm{d}^2r' \end{aligned} \tag{5.3}$$

Similarly for the infinite slab, from (5.2) and (5.1), the magnetic field at $\mathbf{r}=(x,y,0)$ generated by sheet current cylinders of infinite height along the z-axis is

$$\begin{aligned}\mathbf{H}(\mathbf{r}) &= \frac{1}{4\pi}\int \nabla\frac{1}{|\mathbf{r}-\mathbf{r}'|}\times(-\hat{\mathbf{z}}\times\nabla'g(\mathbf{r}'))\,\mathrm{d}^3r' \\ &= \frac{1}{4\pi}\int \nabla g\left(\hat{\mathbf{z}}\frac{(\mathbf{r}-\mathbf{r}')}{|\mathbf{r}-\mathbf{r}'|^3}\right)-\hat{\mathbf{z}}\left(\frac{(\mathbf{r}-\mathbf{r}')}{|\mathbf{r}-\mathbf{r}'|^3}\nabla g\right)\mathrm{d}^3r' \\ &= \frac{1}{4\pi}(-\hat{\mathbf{z}})\int\frac{(\mathbf{r}-\mathbf{r}')}{|\mathbf{r}-\mathbf{r}'|^3}\nabla g\,\mathrm{d}^3r' \\ &= \frac{1}{4\pi}(-\hat{\mathbf{z}})\int\int_{-\infty}^{\infty}\frac{(\mathbf{r}-\mathbf{r}')}{|\mathbf{r}-\mathbf{r}'|^3}\nabla g\,\mathrm{d}z'\,\mathrm{d}x'\mathrm{d}y' = -\frac{1}{4\pi}\hat{\mathbf{z}}\int(-2)\frac{\boldsymbol{\rho}-\boldsymbol{\rho}'}{|\boldsymbol{\rho}-\boldsymbol{\rho}'|^2}\nabla g\,\mathrm{d}^2\rho' \\ &= -\frac{1}{4\pi}\hat{\mathbf{z}}\int 2\nabla'\ln|\boldsymbol{\rho}-\boldsymbol{\rho}'|\nabla' g\,\mathrm{d}^2\rho' = \frac{1}{4\pi}\hat{\mathbf{z}}\int 2g(\boldsymbol{\rho}')\nabla'\nabla'\ln|\boldsymbol{\rho}-\boldsymbol{\rho}'|\mathrm{d}^2\rho' \\ &= \hat{\mathbf{z}}\int g(\boldsymbol{\rho}')\delta(\boldsymbol{\rho}-\boldsymbol{\rho}')\mathrm{d}^2\rho' \end{aligned} \tag{5.4}$$

where $\boldsymbol{\rho}=(x,y)$ and $\boldsymbol{\rho}'=(x',y')$

Therefore, we have obtained a relation between the stream function $g(x,y)$ of the induced current and the field distribution by a scalar function $Q(x,y,x',y')=Q(\mathbf{r},\mathbf{r}')$ as

$$H_z(\mathbf{r}) = H_a + \int_A Q(\mathbf{r},\mathbf{r}')\,g(\mathbf{r}')\,\mathrm{d}^2r' \tag{5.5}$$

Equation (5.5) can be inverted and therefore for a given field distribution the stream function can be found as

$$g(\mathbf{r}) = \int_A Q^{-1}(\mathbf{r},\mathbf{r}')\,[H_z(\mathbf{r}')-H_a]\,\mathrm{d}^2r' \tag{5.6}$$

with

$$Q(\mathbf{r},\mathbf{r}') = \begin{cases} \frac{1}{4\pi}\frac{1}{|\mathbf{r}-\mathbf{r}'|^3} & \text{thin disc} \\ \\ \delta(\mathbf{r}-\mathbf{r}') & \text{infinite slab} \end{cases} \tag{5.7}$$

The electric field is given by a non-linear resistivity $\mathbf{E} = \rho(|\mathbf{J}|)$ for the infinite slab and by the sheet resistivity $\mathbf{E} = \rho(|\boldsymbol{\sigma}|)$ in the case of the thin disc, but it can be expressed as a unified function of the stream function g,

$$\mathbf{E} = -\rho(|\nabla g|)\hat{\boldsymbol{z}} \times \nabla g(x,y) \tag{5.8}$$

Since $\dot{\mathbf{B}} = \hat{\boldsymbol{z}}\dot{B}_z = -\nabla \times \mathbf{E}$, then

$$\dot{B}_z = \nabla \cdot \rho(|\nabla g|)(\nabla g) \tag{5.9}$$

Substituting in (5.6) taking the time derivative, the final equation of motion for $g(x,y)$ is reduced to

$$\dot{g}(\mathbf{r},t) = \int_A Q^{-1}(\mathbf{r},\mathbf{r}') \left[\nabla \cdot (\frac{\rho(|\nabla g|)}{\mu_0}\nabla g(\mathbf{r}',t)) - \dot{H}_a(t)\right] \mathrm{d}^2 r' \tag{5.10}$$

For a given time varying applied field $H_a(t)$ and an initial distribution of the stream function $g(\mathbf{r},t_0)$, the evolution of the stream function can be determined by solving equation (5.10).

5.3 Numerical solution

Numerical solution of g can be obtained readily by time integration, tabulating the functions in a grid with points $\mathbf{r}_i = [x_i, y_i]$ covering the total area transverse to the applied field. From g, $H_{z_i} = Q_{ij}g_j + H_a$, $J_{x_i} = (\frac{\partial g}{\partial y})_i$ and $J_{y_i} = -(\frac{\partial g}{\partial x})_i$ are obtained, according to (5.5) and (5.1). Note that the kernel is calculated only once for a particular geometry but every time step spatial derivatives must be computed.

One of the main points in this formulation is the evaluation of the kernel for the diagonal elements which are singular according to (5.7). For thin discs, as shown in [32], the field in a point (x,y,z) of a tiny current loop with center in $(0,0,0)$ and axis along z is:

$$H_z(x,y,z) = \frac{1}{4\pi}\frac{2z^2 - x^2 - y^2}{(x^2+y^2+z^2)^{5/2}} \tag{5.11}$$

Hence, the constant function $Q(\mathbf{r},\mathbf{r}')$ for all the grid points is given by :

$$Q(\mathbf{r},\mathbf{r}') = \frac{1}{4\pi}\lim_{z\to 0}\frac{3z^2 - d^2}{(d^2+z^2)^{5/2}} \tag{5.12}$$

where d is the distance between $\mathbf{r}$ and $\mathbf{r}'$.

Approximating Q by (5.12) and using its Fourier expansion with as many points as in the spatial grid, Brandt ([32],[8]) shows that the singularity is avoid without significant errors. The expression for Q is

$$Q(\mathbf{r},\mathbf{r}') = \frac{1}{ab}\sum_{k_x,k_y}\sum_{k'_x,k'_y} Q_{k_x,k_y,k'_x,k'_y}\sin(k_x x)\sin(k_y y)\sin(k'_x x')\sin(k'_y y') \tag{5.13}$$

This kernel can be evaluated with better accuracy and without singularities for diagonal elements by using current loops uniformly distributed over the whole cell [42].

In the case of the slab where $Q(\mathbf{r},\mathbf{r}') = \delta(\mathbf{r}-\mathbf{r}')$, since $\int\int_A \delta(\mathbf{r}-\mathbf{r}')\delta(\mathbf{r}-\mathbf{r}'')\,\mathrm{d}^2r'\mathrm{d}^2r'' = 1$, then $Q^{-1}(\mathbf{r},\mathbf{r}') = \delta(\mathbf{r}-\mathbf{r}')$ and the final equation (5.10) is simplified to a local equation without any singularities:

$$\dot{g}(\mathbf{r},t) = \nabla\cdot\left(\frac{\rho}{\mu_0}\nabla g(\mathbf{r},t)\right) - \dot{H}_a(t) \tag{5.14}$$

Arbitrary non-linear resistivity $\rho = E/J$ can be inserted in this formulation. In this work power-law $E-J$ characteristic for superconductors is used, i.e. $E = E_c\cdot(J/J_c)^n$ with the parameters $J_c = 10^8\,\mathrm{Am}^{-2}$, $E_c = 10^{-4}\,\mathrm{Vm}^{-1}$ and $n = 21$. For the thin disc, the sheet critical current density is $\sigma_c = 10^4\,\mathrm{Am}^{-2}$, corresponding to $d = 10^{-4}\,\mathrm{m}$ for $J_c = 10^8\,\mathrm{Am}^{-2}$. To model the coupling behavior between superconductors (figures 5.1.(b) and (d)), a normal conductor is considered with a constant resistivity ,e.g. that of copper at liquid nitrogen temperatures $\rho = 2\cdot 10^{-9}\,\Omega\mathrm{m}$ and the correspondent sheet resistivity of $\rho_s = \rho/d = 2\cdot 10^{-5}\,\Omega\mathrm{m}$.

5.4 Validation

The formulation was applied to two simple situations for validation: a square thin disc and a square infinite slab (figures 5.1.(c) and 5.1.(a) respectively). Because of symmetries the results shown below correspond to a quarter of the total model, $0 \leq x \leq a, 0 \leq y \leq b$, with $2a = 2b = 4\,\text{mm}$ being the width and the length of the square.

The field profiles for the slab shown in figure 5.2 are similar to Bean's model [5], where the field decreases linearly in the penetrated area, from the edges to the center, with slope $\mu_0 J_c$ given by $\nabla \times \hat{\mathbf{z}} H = \mathbf{J}$. Another characteristic to compare is the field value $\mu_0 H_p$ at which the magnetic flux has penetrated to the center of the slab. According to Bean's model this value is calculated as $\mu_0 H_p \approx \mu_0 J_c a = 0.25\,\text{T}$ for an slab of infinite length, compared to $\mu_0 H_a \simeq 0.27\,\text{T}$ for the square slab shown in figure 5.2. Further increase of the applied field results in a finite field at the center.

The stream function g of the induced current has the shape of a typical roof. The streamlines, $g = const.$, represent the lines of the current flow which is restricted to the penetrated area (figures 5.2.(a) and 5.2.(b)). As expected, the lines are straight and turn sharply in the corners to pass by 90° from one direction to the other.

For the thin disc (figure 5.3) the field profile is non-linear. The streamlines have a rectangular shape in the penetrated part where the current is $\sigma = \sigma_c$ and become circular in the inner part unpenetrated by the flux. Current flow in field free regions is due to the zero thickness of the disc similar to that in a infinite thin strip. At the value $\mu_0 H_a \simeq 0.02\,\text{T}$ the disc is fully penetrated, which is about double of the theoretical value $\mu_0 H_p$ for an infinite strip [25], as shown in the corresponding field profile along the lines $x = 0$ and $y = 0$ (figure 5.3.(c)). For a longer superconductor, $b = 1.6\,\text{mm}$, (figure 5.3.(d)) the saturation field is reduced to that predicted for infinite strip. The significant scattering at corner due to the approximation of Q does not seem to affect the result within the conductor.

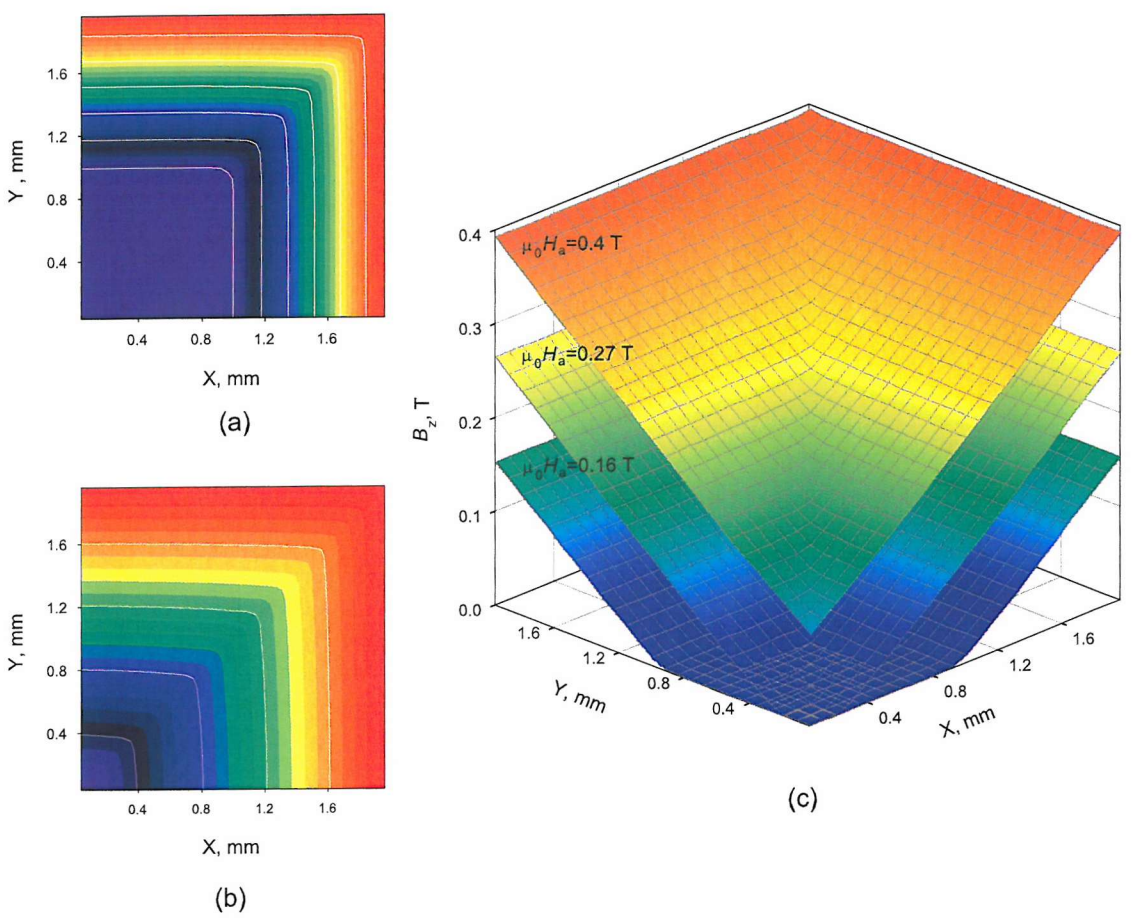

Figure 5.2: Streamlines of the induced current in a square slab for the applied fields $\mu_0 H_a = 0.16\,\mathrm{T}$ (a) and $\mu_0 H_a = 0.4\,\mathrm{T}$ (b), and corresponding magnetic field profile (c).

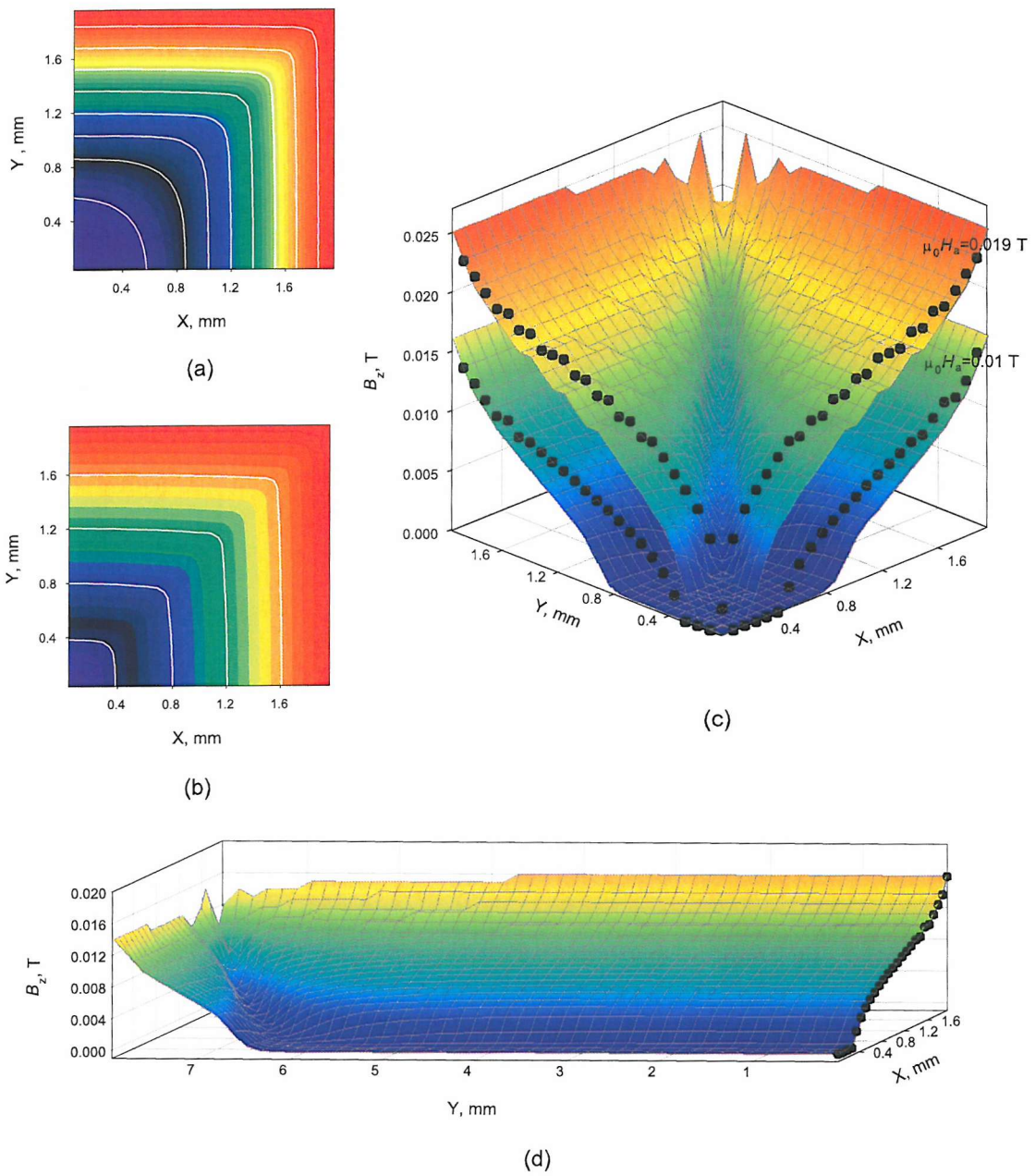

Figure 5.3: Streamlines of the current in a square disc, for applied fields $\mu_0 H_a = 0.01\,\mathrm{T}$ (a) and $\mu_0 H_a = 0.019\,\mathrm{T}$ (b), and corresponding magnetic field profile (c). Magnetic field profile for a thin disc of length 8 mm (d). Analytical field profile for a infinity disc of the same width is shown (•).

5.5 Results and comments

As the formulation applies satisfactorily to isolated thin discs and slabs as shown in previous section, it is reasonable to extend it for modelling the coupling between two superconductors through a matrix. It is sufficient to consider the non-linear resistivity in the superconducting region and a constant resistivity for the normal conductor region. Then taking

$$\rho(|\nabla g|) = \begin{cases} E = E_c \cdot (J/J_c)^n & \text{superconducting region} \\ \text{constant } \rho & \text{matrix region} \end{cases} \tag{5.15}$$

and given an initial distribution of the stream function $g(\mathbf{r}, t_0) = 0$, the evolution of the stream function can be determined by solving equation (5.10).

We have performed the calculations for slabs and thin discs with width $2a = 1.4\,\text{mm}$ and length $2b = 8\,\text{mm}$ with a normal matrix $w = 0.3\,\text{mm}$ wide. Again, due to symmetries, only the quarter $[0, 2a + d/2] \times [0, b]$ of the model will be used (see figure 5.1).

5.5.1 Slab

Figures 5.4 and 5.5 show the coupling phenomenon produced at different ramp rates of the field $\dot{B}$. Plots are represented for two possible states: partial penetration, $H_a < H_p$ (figure 5.4) and full penetration, $H_a \geq H_p$ (figure 5.5). At partial penetration and small ramp rate of the applied field ($\dot{B} = 0.63\,\text{Ts}^{-1}$) the slabs are uncoupled (figure 5.4.(a)). Their behavior is similar to that for two independent slabs where the current is flowing inside the superconductors in rectangular loops only in the penetrated area. At higher ramp rate ($\dot{B} = 100\,\text{Ts}^{-1}$) the current starts to cross the matrix, there is no current returning within the same superconductor, and the center of the matrix is shielded from the magnetic field (figure 5.4.(b)). The total coupling current is equal to the total current along the slab in the penetrated area.

Similarly, increasing the applied field the slabs remain uncoupled at low $\dot{B}$ (figure 5.5.(a)) and coupled at high $\dot{B}$ (figure 5.5.(b)). It should be noticed that the full penetration field of coupled slabs is double than that for uncoupled ones.

The field profile along x-axis at $y = 0$ is presented in figure 5.6.(a). For a given applied field, with increasing $\dot{B}$ the field in the matrix decreases. Notice that for a small

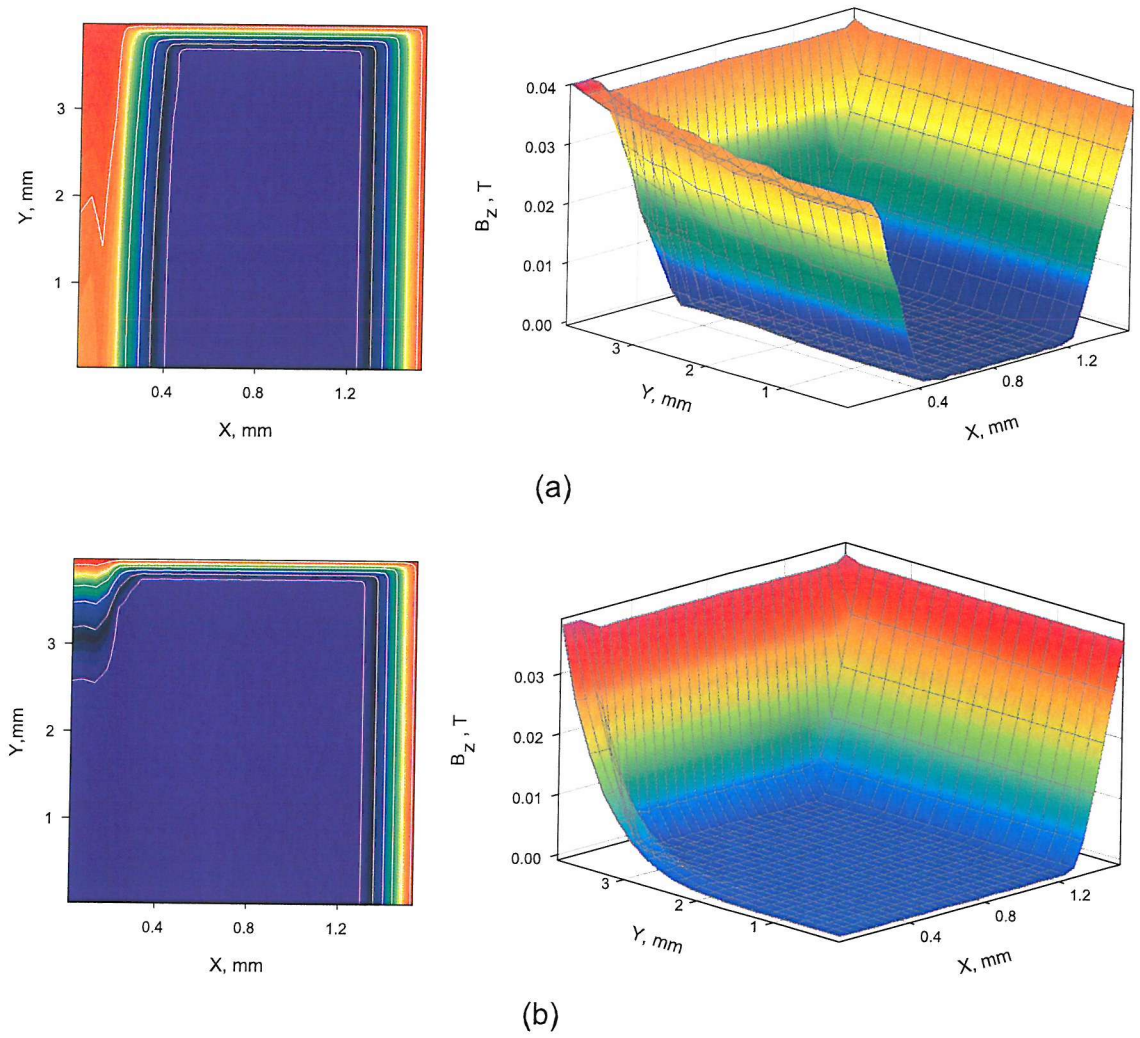

Figure 5.4: Streamlines and magnetic field profiles of partially penetrated slabs in an applied field $\mu_0 H_a = 0.04\,\mathrm{T}$ ramping at $\dot{B} = 0.631\,\mathrm{Ts}^{-1}$ (a) and $\dot{B} = 100\,\mathrm{Ts}^{-1}$ (b).

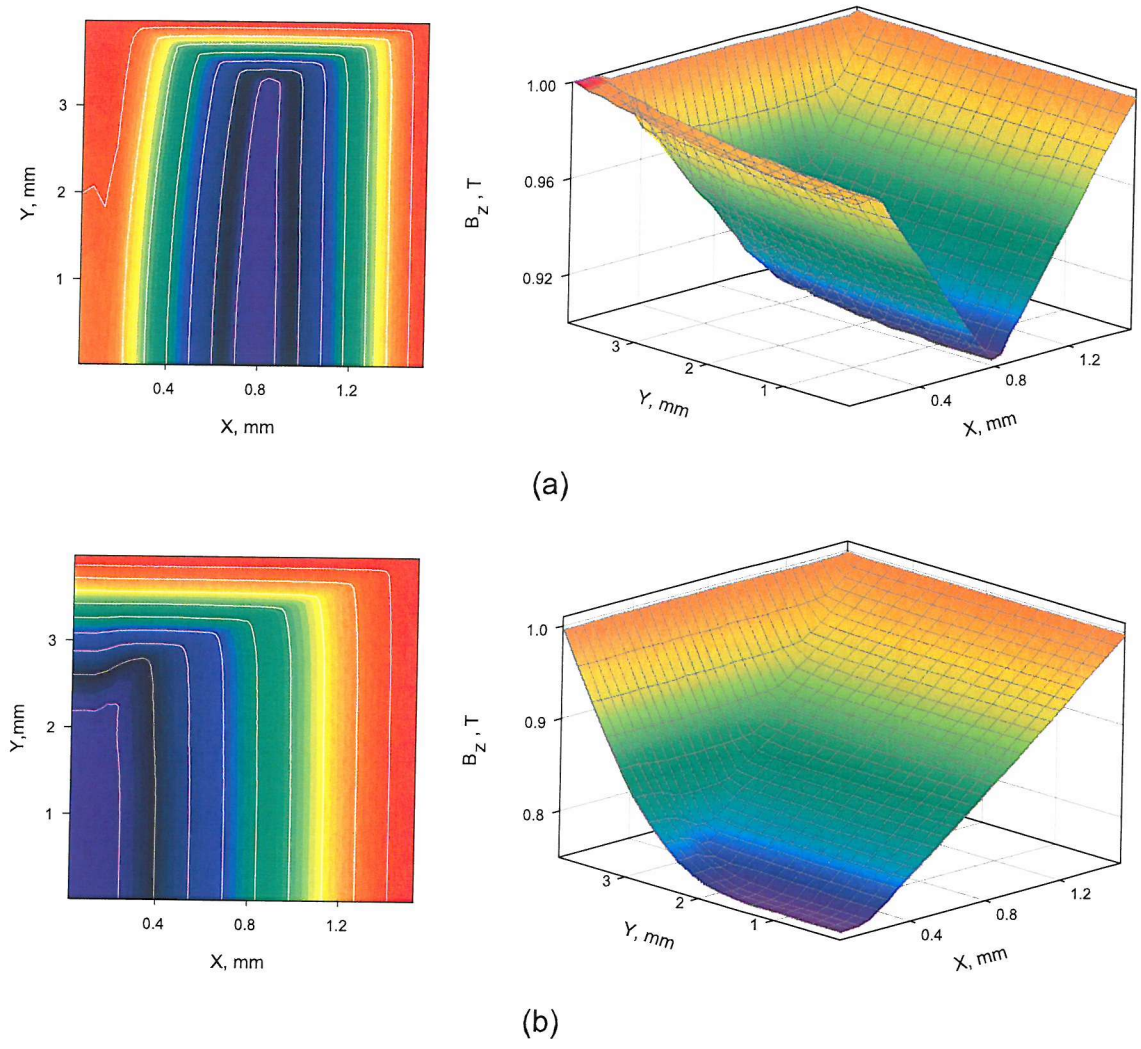

Figure 5.5: Streamlines and magnetic field profile of fully penetrated slabs in an applied field $\mu_0 H_a = 1\,\mathrm{T}$ ramping at $\dot{B} = 0.631\,\mathrm{Ts}^{-1}$ (a) and $\dot{B} = 100\,\mathrm{Ts}^{-1}$ (b).

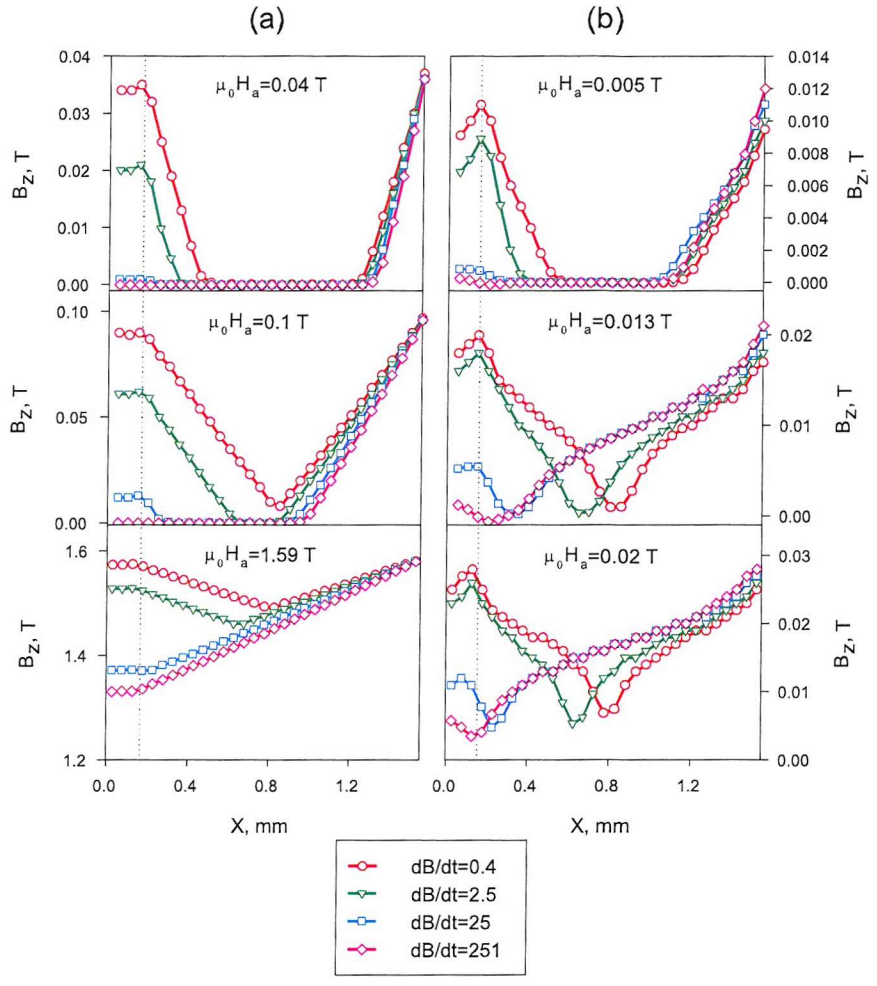

Figure 5.6: Magnetic field profile along the x-axis in the middle of the slab (a) and the thin disc (b) at different ramp rates of the applied field.

applied field ($\mu_0 H_a = 0.04\,\mathrm{T}$), at total coupling the field decreases to zero in the normal matrix, however for fully coupled saturated slabs ($\mu_0 H_a = 1.59\,\mathrm{T}$) the field reduces to a finite value.

In figure 5.6.(a) we can see that at $\dot{B} = 25\,\mathrm{Ts}^{-1}$ for $\mu_0 H_a = 0.04\,\mathrm{T}$ the slabs are fully coupled, whereas for $\mu_0 H_a = 0.1\,\mathrm{T}$ clearly only partially coupled and for $\mu_0 H_a = 1.59\,\mathrm{T}$ nearly fully coupled, indicating a higher $\dot{B}_c$ for $\mu_0 H_a \approx \mu_0 H_p$.

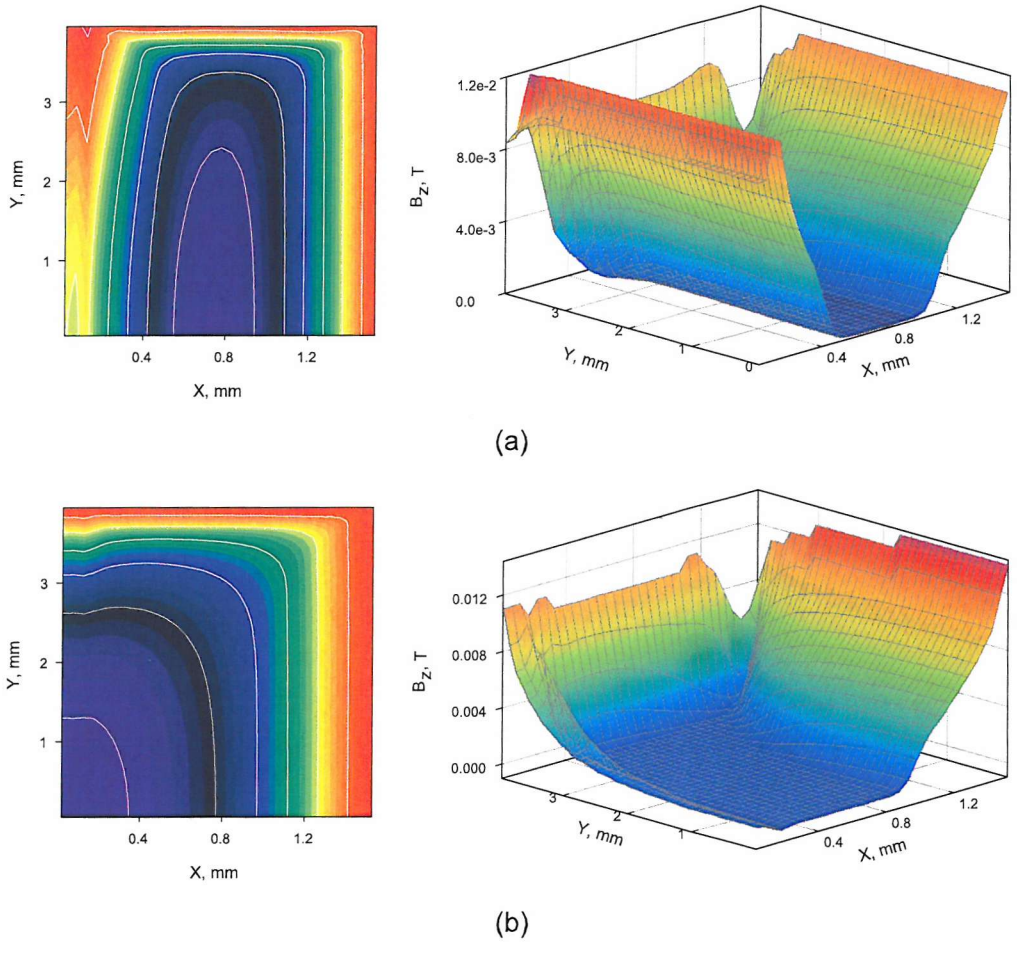

Figure 5.7: Streamlines and magnetic field profile of partially penetrated thin discs in an applied field ramping at $\dot{B} = 1\,\mathrm{Ts}^{-1}$ (a) and $\dot{B} = 100\,\mathrm{Ts}^{-1}$ (b) to $\mu_0 H_a = 6.325 \cdot 10^{-3}\,\mathrm{T}$.

5.5.2 Thin disc

As expected the coupling between thin discs increases with increasing $\dot{B}$ (figures 5.7 and 5.8). In contrast to slabs, the field profile is non-linear in both uncoupled and coupled cases. It should be noted that the applied field is smaller than that used for the slabs, due to a smaller full penetration field (0.02 T). At partial penetration, the field free region of fully coupled discs also has induced current,due to the zero thickness of the discs, which flows across the normal matrix from one disc to the other (figure 5.7.(b)). For higher fields it is difficult to model the coupling since it would require a more fine mesh to represent with accuracy the field profile for such cases.

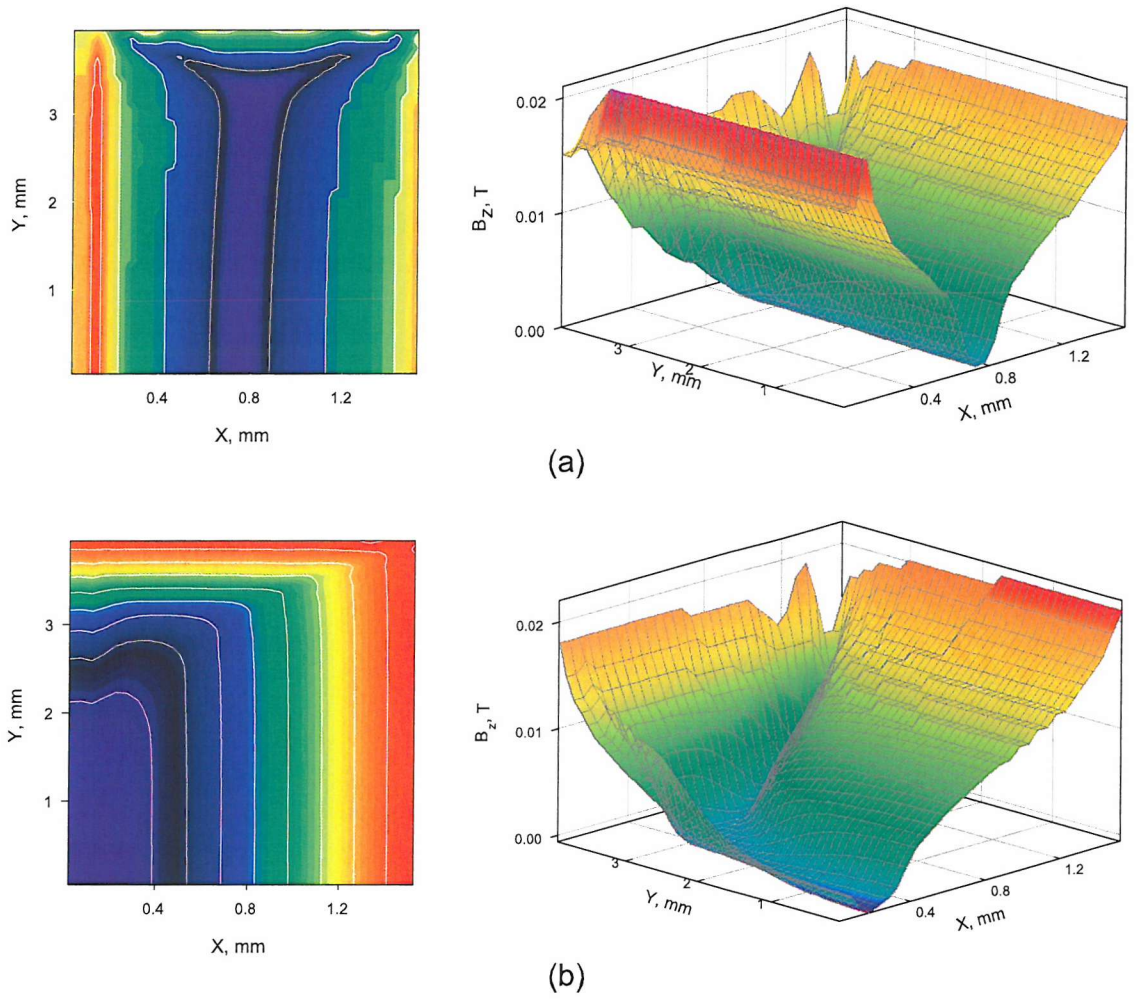

Figure 5.8: Streamlines and magnetic field profile of totally penetrated thin disc in an applied field ramping at $\dot{B} = 1\,\mathrm{Ts}^{-1}$ (a) and $\dot{B} = 100\,\mathrm{Ts}^{-1}$ (b) to $\mu_0 H_a = 0.013\,\mathrm{T}$.

The field profile along x-axis at the center ($y = 0$) is shown in figure 5.6.(b). Similarly to the slab, the reduction of the field in the normal conductor with increasing f is observed. However, a difference with the slab, notice that the field in the matrix is not constant and changes from a positive gradient to a negative one as the superconductors become coupled.

5.5.3 Critical coupling field $\dot{B}_c$

The objective of the modelling presented in this chapter is to obtain quantitative information about the coupling phenomenon for the whole range of the applied field. It is particularly important for practical applications the obtention of the critical coupling field rate $\dot{B}_c$, defined as the ramp rate of the field which induces all the current in the superconductor to cross through the matrix to the other superconductor. The only theoretical model developed to predict $\dot{B}_c$ is given for two fully penetrated infinite slabs [41] where

$$\dot{B}_c = 16\rho J_c a/(2b)^2 \tag{5.16}$$

We have now obtained for the first time a quantitative determination of $\dot{B}_c$ for partially penetrated slabs.

In figure 5.9, the coupling current (J_x integrated at $x = 0$ along y-axis) is plotted against the applied field and the ramp rate for discs and slabs. Given a particular $\mu_0 H_a$, the coupling current increases with $\dot{B}$ until the critical value $\dot{B}_c$ is reached, then becomes constant with further increase of $\dot{B}$. The level of full coupling current increases with the applied field $\mu_0 H_a$ before full penetration, and reaches saturation at $\mu_0 H_a \geq \mu_0 H_p$.
At a fixed $\dot{B}$ there are differences in the profiles between slabs and thin discs. For the slabs there is a stronger dependence of the coupling on the applied field. The coupling current increases with the field and saturates at the value of the coupling current induced by that ramp rate. For the disc at low field the situation is different, the current reaches the maximum value immediately as soon as the field is applied.

The critical coupling field rate $\dot{B}_c$ can be obtained identifying in figure 5.9 when the coupling current reaches saturation for a given applied field. For the slabs (figure 5.10.(a)), $\dot{B}_c$ increases linearly with the applied field to reach a pronounced maximum of $\sim 190\,\mathrm{Ts}^{-1}$ just before full penetration. At higher fields beyond full penetration $\dot{B}_c$ reduces to a constant value of $\dot{B}_c \approx 34\,\mathrm{Ts}^{-1}$, in agreement with that $\approx 35\,\mathrm{Ts}^{-1}$ obtained with the formula (5.16) for saturated slabs.

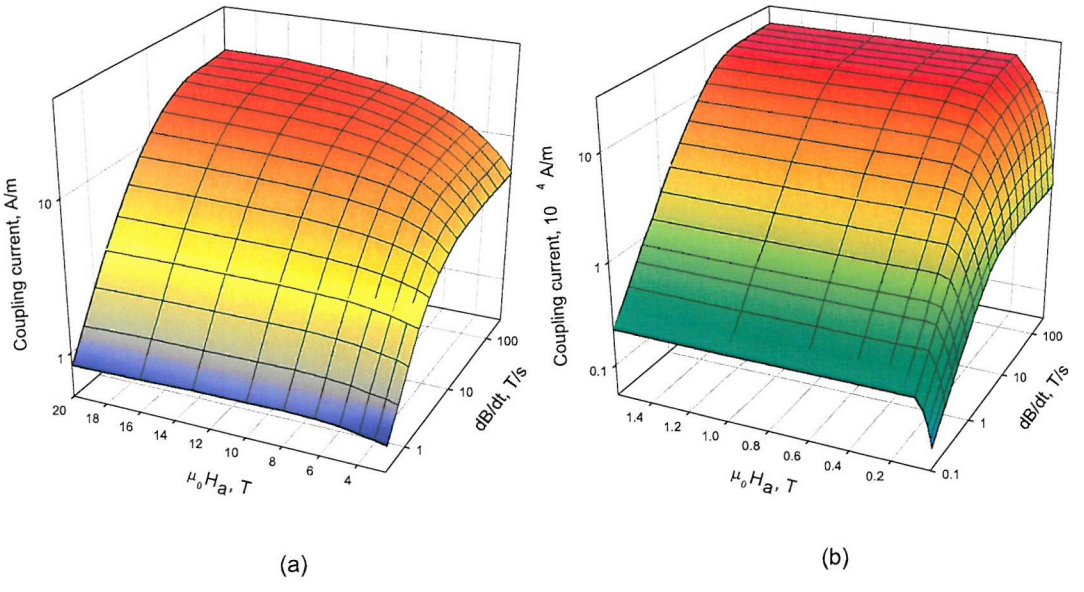

Figure 5.9: Coupling current for thin discs (a) and slabs (b) as a function of the applied field and its ramp rates $\dot{B}$.

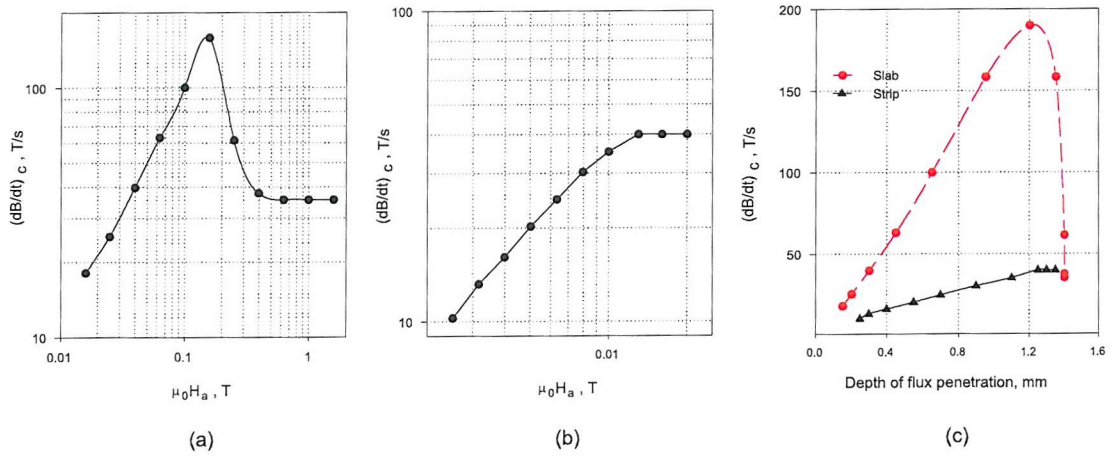

Figure 5.10: Critical coupling filed rate $\dot{B}_c$ as a function of the applied magnetic field for a slab (a) and for a thin disc (b). Corresponding $\dot{B}_c$ as a function of the flux penetration depth (c).

For think discs, the critical coupling field rate also increases linearly with the applied field at low fields until reaches saturation of $\dot{B}_c = 40\,\mathrm{Ts}^{-1}$ when is fully penetrated.

In figure 5.10.(c) the coupling field is compared between slabs and thin discs as a function of depth of field penetration. As expected the coupling between thin discs is produced much sooner at small penetration, however for total penetration at high fields the critical current field rates are similar.

5.5.4 Coupling current during a ramp field oscillation

In most of practical applications, superconductors are in oscillating magnetic fields. As it was shown in previous chapter, the time evolution of the coupling effect in sinusoidal fields is complex due to the continuous variation of $\mathrm{d}B/\mathrm{d}t$. To consider a simpler model and to continue with the calculations shown in previous section, here it will analyzed the coupling effect during a cycle of a ramp field, $\mu_0 H_a = \mu_0 \dot{H}_a t$. The applied field, plotted in figure 5.11.(b), is raised to a maximum $\mu_0 H_m$ higher than total penetration field $\mu_0 H_p$ then is reduced to $-\mu_0 H_m$ and returns to zero to finish the cycle time.

The coupling current profiles are shown in figure 5.11. Since the time intervals vary at different ramp rates, the results are plotted against $t \cdot \dot{B}$. The coupling current increases in time to saturate before the peak field $\mu_0 H_m$. According to figure 5.10.(a), at $\mid \dot{B} \mid = 25\,\mathrm{T/s}$ slabs are totally penetrated only at low fields, hence the coupling current at the beginning of the cycle is equal than that for higher ramp rates, however at higher fields increases slower to saturate later. At $\mid \dot{B} \mid = 158.5\,\mathrm{T/s}$, the slabs are totally coupled for the whole range of the applied field (see figure 5.10.(a)) and therefore the coupling current increases faster to saturate when $\mu_0 H = \mu_0 H_p$ at the maximum coupling current. Consistent with the values of $\dot{B}_c$ in figure 5.10.(a), observe in the profile for $\mid \dot{B} \mid = 63.1\,\mathrm{T/s}$ that at about $\mu_0 H_p$ the coupling current is not maximum yet, however for higher fields the slab are fully coupled.
The coupling current decreases with reducing the applied field to reach a minimum, and then remains constant until the applied field has decreased to $-\mu_0 H_m$. Notice that for high ramp rates the minimum is reached when the field has reduced $2\mu_0 H_p$ from the positive peak. Observe that the profiles from peak to peak become linear for high ramp rates.

With respect to the applied field in the matrix shown in figure 5.11.(b), it is observed that the field increases with reducing $\dot{B}$ as expected. For a low ramp rate, the matrix is shielded at the beginning and then starts to increase with the applied field since the slabs

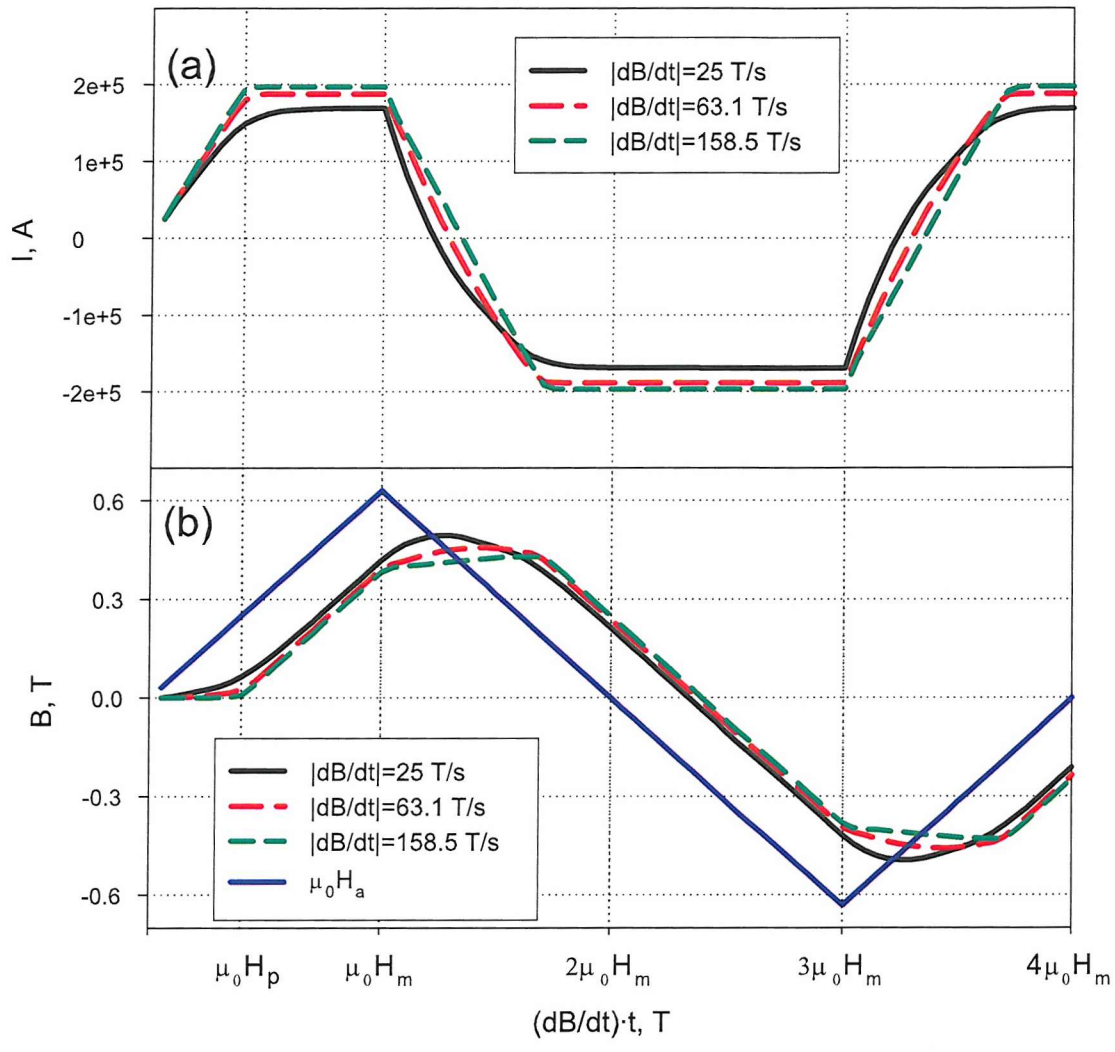

Figure 5.11: Coupling current evolution (a) and magnetic field in the normal matrix (b) for a cycle time.

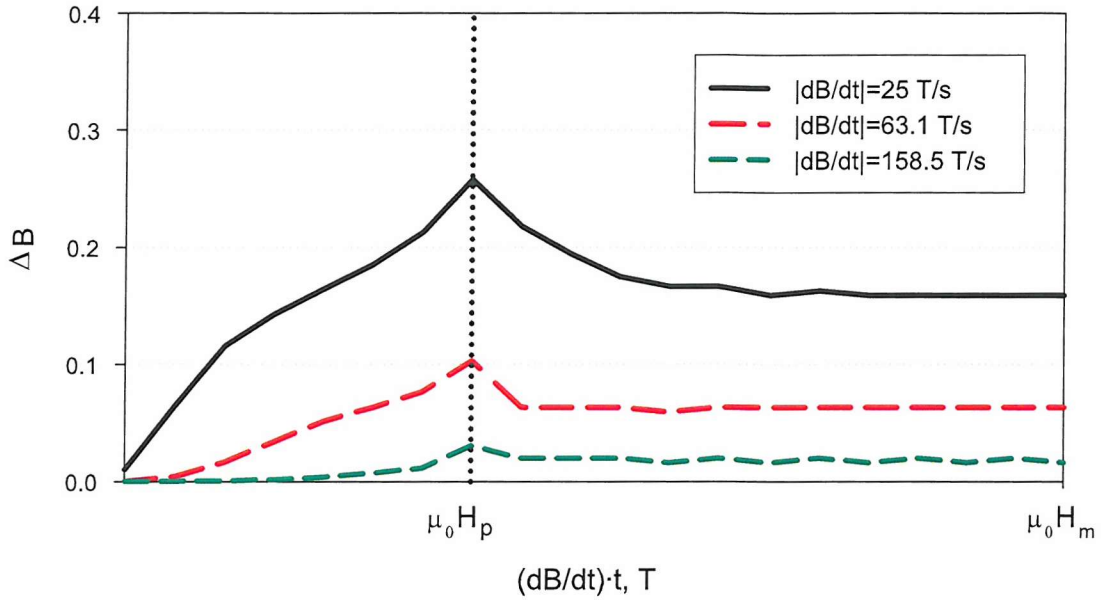

Figure 5.12: Profile of the relative penetrated flux, as given in the text.

are not coupled. For higher $\dot{B}$, since the slabs are totally coupled, the field is shielded before total penetration field, and then increases at the same rate as the applied field. Notice that after field reductions the field in the normal matrix continues increasing for a period of time before reducing with the same slope as the applied field, leading to field trapped in the normal matrix when the applied field has returned to zero.

A detailed plot of the first quarter of the cycle time is seen in figure 5.12. To compare the coupling for different ramp rates, it is represented the relative penetrated flux, ΔB in the normal matrix, defined as the penetrated flux divided by the applied field for $t \leq H_p/\dot{H}$, that is, before full penetration. For $t > H_p/\dot{H}$ (full penetration), having into account that a increment of the applied field beyond full penetration leads to a finite field in the normal matrix, the relative penetrated flux is defined as $(B-(\mu_0 H_a - \mu_0 H_p))/\mu_0 H_p$. Observe that the field increases more for low ramp rates since the slabs are not totally coupled. The field decreases after total penetration situation according to figure 5.10.(a) where it was seen a reduction of $\dot{B}_c$ after total penetration.

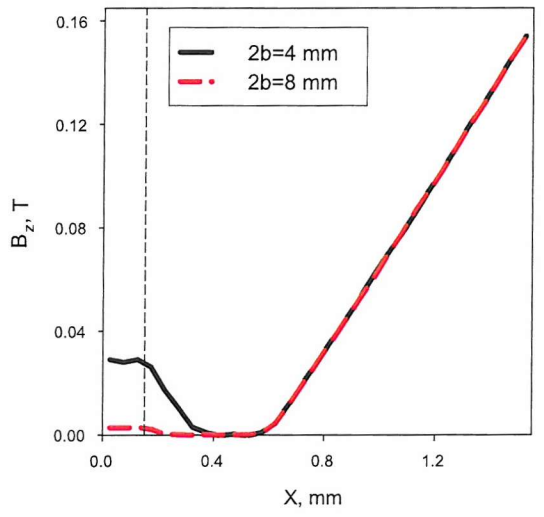

Figure 5.13: Magnetic field profile along the x-axis in the middle ($y = z = 0$) of the slab at $\mu_0 H_a = 0.158\,\mathrm{T}$ and ramp rate $100\,\mathrm{Ts}^{-1}$.

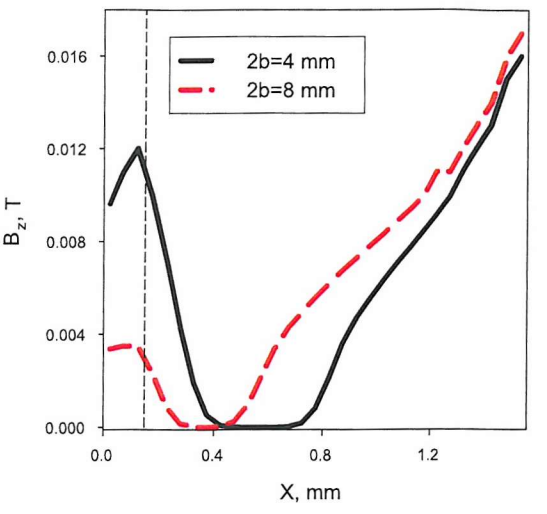

Figure 5.14: Magnetic field profile along the x-axis in the middle ($y = z = 0$) of the thin disc at $\mu_0 H_a = 0.01\,\mathrm{T}$ and ramp rate $25.119\,\mathrm{Ts}^{-1}$.

5.5.5 Influence of the length of the superconductor

It is known by theory (equation (5.16)) that for infinite saturated slabs in the critical state, the critical field ramp rate increases with reducing the length of the superconductor. In this section $\dot{B}_c$ is calculated numerically for infinite slabs and thin disc of different lengths including partial and total penetration cases. The objective is to find a relation between length and $\dot{B}_c$ and compare it with the theoretical prediction.

Observe first the plot of the magnetic field profiles along x-axis in figures 5.13 and 5.14 for the slab and thin disc respectively with lengths 4 and 8 mm. At the same ramp rate $\dot{B}$, the field in the normal matrix differs for the different lengths indicating different coupling behavior. Whereas for the longest slab the field is almost zero in the normal matrix since it is almost fully coupled, for the short one, has not decreased so much (figure 5.13) and the coupling is only partial. The same effect occurs for the thin disc (figure 5.14) where it is observed that the field has decreased more for the long one. We can confirm therefore the expected increment of $\dot{B}_c$ with reducing the length in both geometries.

The quantitative values of $\dot{B}_c$ are shown in figure 5.15.(a) for slabs at different applied fields. The increase of B_c with reducing the length is found for the whole range of the applied field. To compare with formula (5.16), in figure 5.15.(b) it is plotted $B_c(2b)^2$ as a function of the applied field. For small fields just before full penetration, exactly inverse

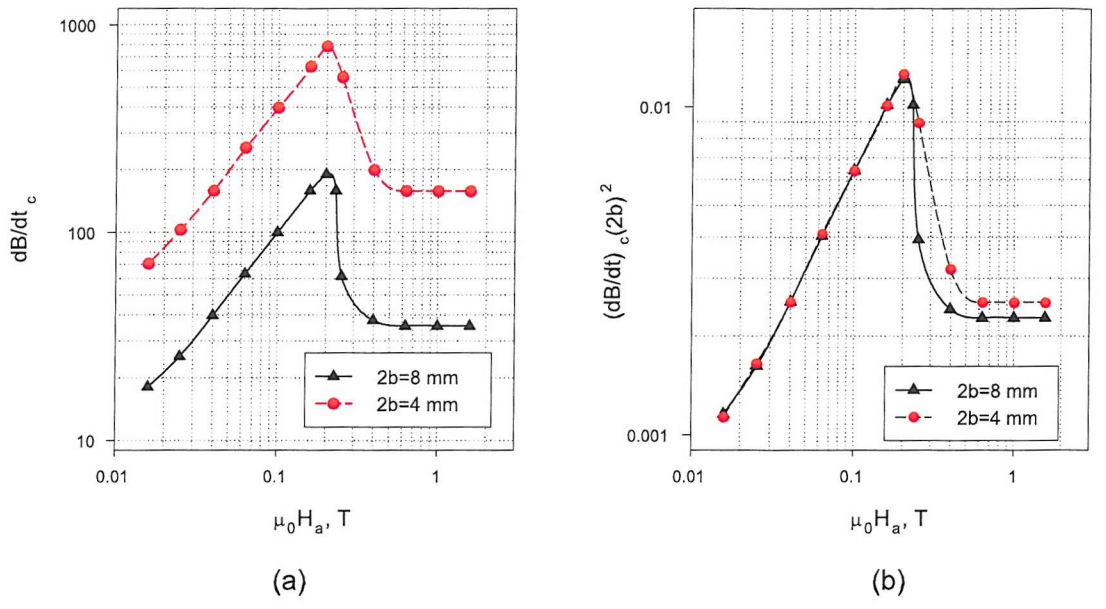

Figure 5.15: Critical field ramp rate as a function of the applied magnetic field for slabs of different lengths (a). To compare with formula (5.16), it is shown $\dot{B}_c(2b)^2$ (b).

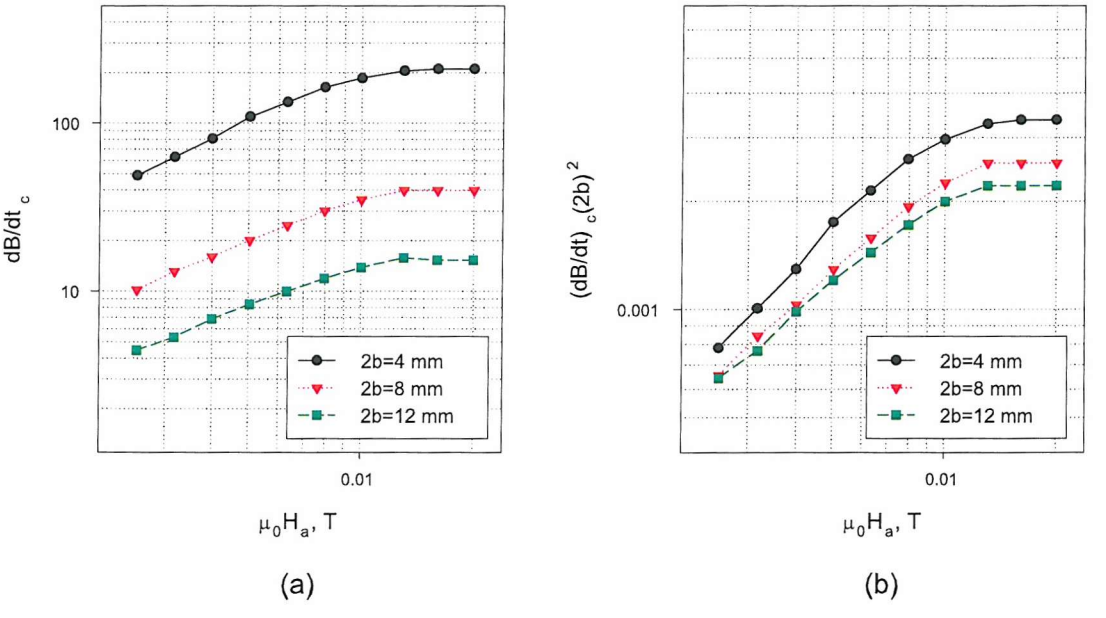

Figure 5.16: Critical field ramp rate as a function of the applied magnetic field for thin discs of different lengths (a). To compare with formula (5.16), it is shown $\dot{B}_c(2b)^2$ (b).

quadratic dependence of $\dot{B}_c$ on the slab length is found, the same as in formula (5.16). At higher fields, $H \gg H_p$, the dependence varies a little but is almost $\dot{B}_c \sim 1/4b^2$.

For the thin disc, $\dot{B}_c$ is shown in figure 5.16. As expected, the critical ramp rate of the field is higher for the short thin disc. However, a difference with the infinite slab, there is not a inverse quadratic relation (figure 5.16.b).

Slabs with length $b \leq 2a$

So far we have studied slabs with different lengths $2b$ such that $b \gg 2a$. In such cases, at saturation field, H_p, the slab is totally penetrated along the width (figure 5.17.(a)). However, when the slab is shorter than wide, the field reaches the center first along the length as it is shown in figure 5.17.(b), and therefore current will flow along the slabs in the y-direction only in a small region.

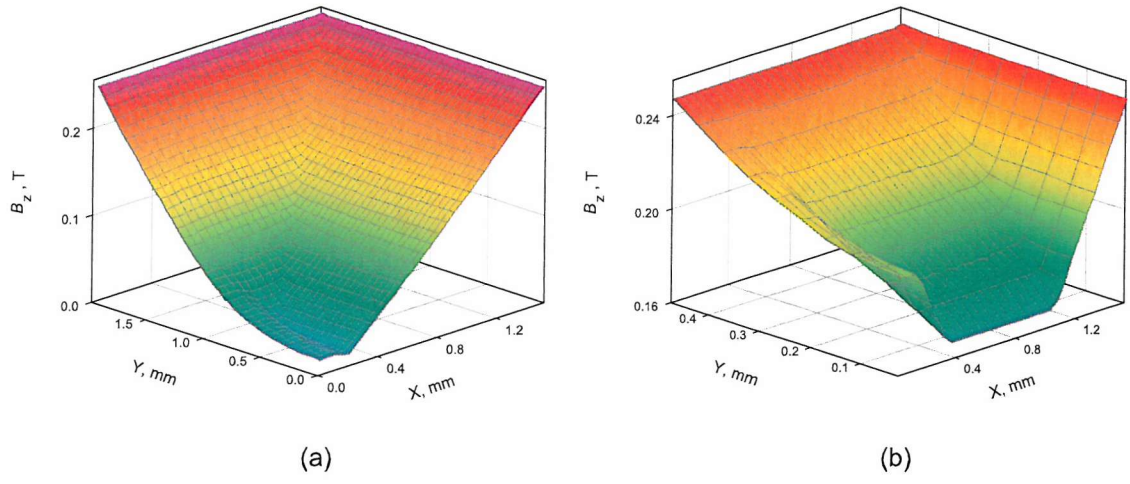

Figure 5.17: Magnetic field profile of saturated slabs in and magnetic field ramping at $398.107\,\mathrm{Ts}^{-1}$ to $\mu_0 H_a = 0.251\,\mathrm{T}$ with length $2b = 4\,\mathrm{mm}$ (a) and $2b = 1\,\mathrm{mm}$ (b).

The critical ramp rate as a function of the applied field is seen in figure 5.18. For comparison with long slabs it is also represented an example of $b > 2a$, $2b = 4\,mm$. Similarly to the plot shown for long slabs in figure 5.15, $\dot{B}_c$ increases linearly with the applied field to reach a maximum just before full penetration, and further increase of the applied field beyond full penetration results in a reduction of $\dot{B}_c$ to a constant value (figure 5.18.(a)). As the length of the slab is reduced the total penetration is

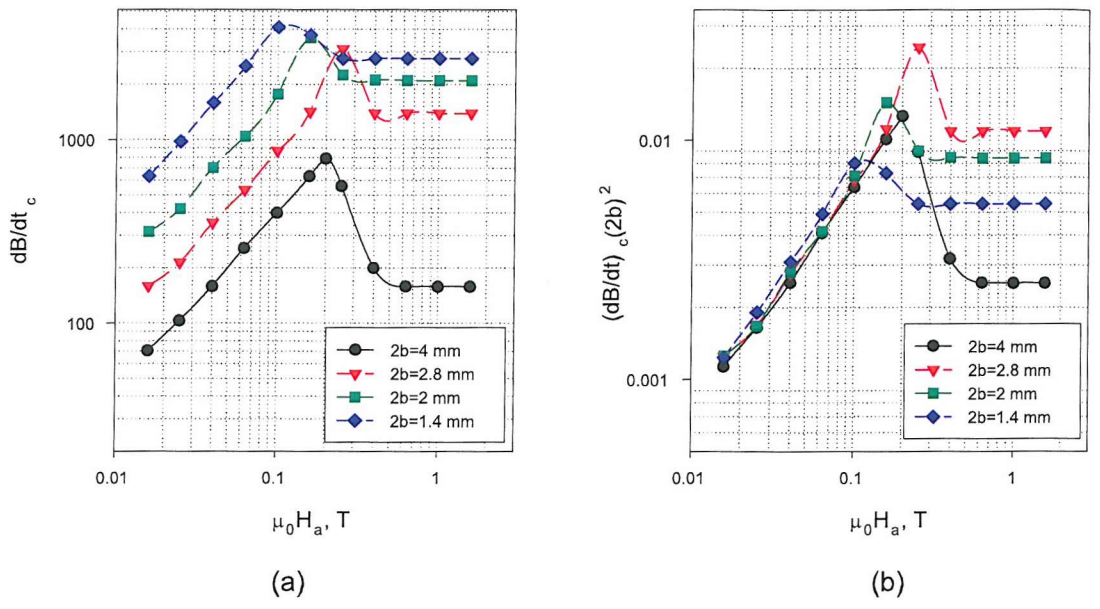

Figure 5.18: Critical field ramp rate as a function of the applied magnetic field for slabs of different lengths (a). To compare with formula (5.16), it is shown $\dot{B}_c(2b)^2$ (b).

produced before, hence the peaks in the curves are reached at lower fields. Compare the pronounced jump after the peak for $2b = 4\,mm$ with the reductions on $\dot{B}_c$ for shorter slabs with $b \leq 2a$.

With respect to the influence of the superconductor length on $\dot{B}_c$, it is seen that at low fields when the slabs are only partially penetrated, there is a inverse quadratic relation between $\dot{B}_c$ and the length (figure 5.18.(b)) as it was found for longer slabs. However for saturated slabs that relation is $\dot{B}_c \sim 1/2b$ for $b \leq 2a$ a difference with longer slabs (observe in 5.18.(b) the case $2b = 4\,mm$).

For a more precise analysis of the behavior of fully coupled slabs observe the field and current profiles shown in figure 5.19 for a short saturated slab with $2b = 1\,\text{mm}$. The streamlines of the induced current (figure 5.19.(a)) indicate that all the current is flowing in the y direction along the slab in the outer part and then turns to cross the normal matrix. Since the width of the carrying current part in the y-direction is equal to half length of the superconductor b, the coupling current in the matrix becomes very large and therefore it has to increase in the outer part as it is shown by streamlines in figure 5.19.(a). As a consequence of that, notice that the field in the normal matrix has

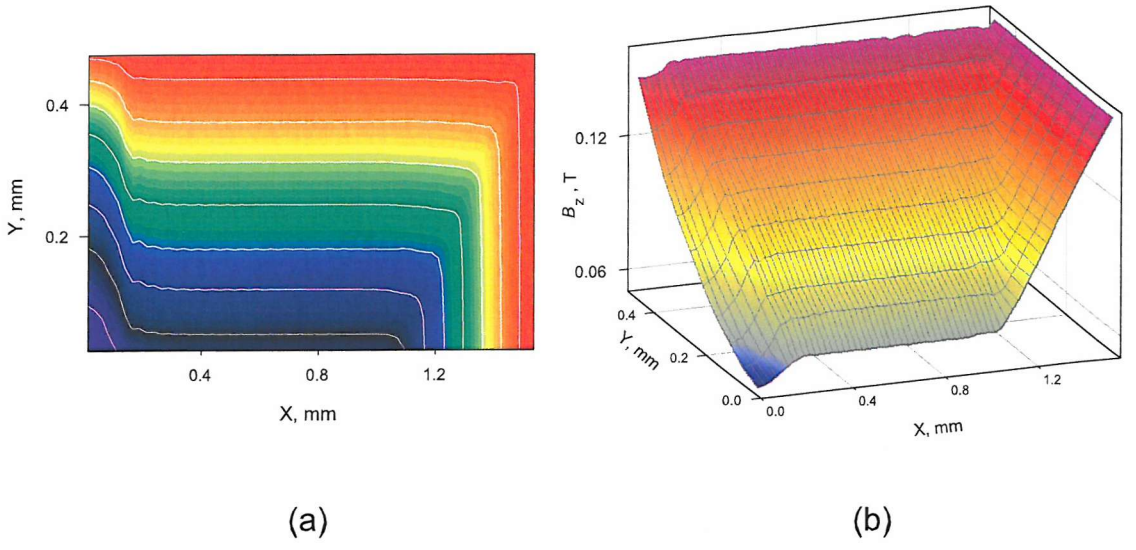

Figure 5.19: Streamlines (a) and magnetic field profile (b) for a penetrated slab of length $2b = 1\,\text{mm}$.

decreased more than in the superconductors when they are fully coupled 5.19.(b). With reducing the length of the slab the coupling current in the normal matrix becomes higher and therefore more voltage is required, and $\dot{B}_c$ increases as it was seen in figure 5.18.

5.5.6 Influence of J_c on the critical coupling field rate

In this section the coupling effect is investigated for different values of the critical current density. For infinite saturated slabs, equation (5.16) establishes a proportional correspondence between this parameter and the critical ramp rate $\dot{B}_c$. For the investigation we have considered values of $J_c = 10^8$ and $2 \cdot 10^8\,\text{Am}^{-2}$ for the slab and $\sigma_c = 10^8$ and $2 \cdot 10^8\,\text{Am}^{-1}$ for thin discs.

According to Bean's model, for infinite slabs the field penetrates into the superconductor with a slope given by $\nabla \times \mathbf{H} = \mathbf{J}$, and therefore the depth of flux penetration is inversely proportional to the critical current density. In figure 5.20, with the field plotted along x-axis at $y = 0$, it is seen that the penetration in the superconductor with $J_c = 10^8\,\text{Am}^{-2}$ is double than that for $J_c = 2 \cdot 10^8\,\text{Am}^{-2}$.

At low applied fields (figure 5.20.(a)), with increasing the ramp rate the field in the matrix part has been reduced to the same value, indicating independence of the coupling effect respect to J_c. However, at applied fields higher than the full penetration

field (figure 5.20.(b)), at the same ramp rate the slab with lower J_c is already totally coupled whereas for double J_c there is still current returning inside the slab.

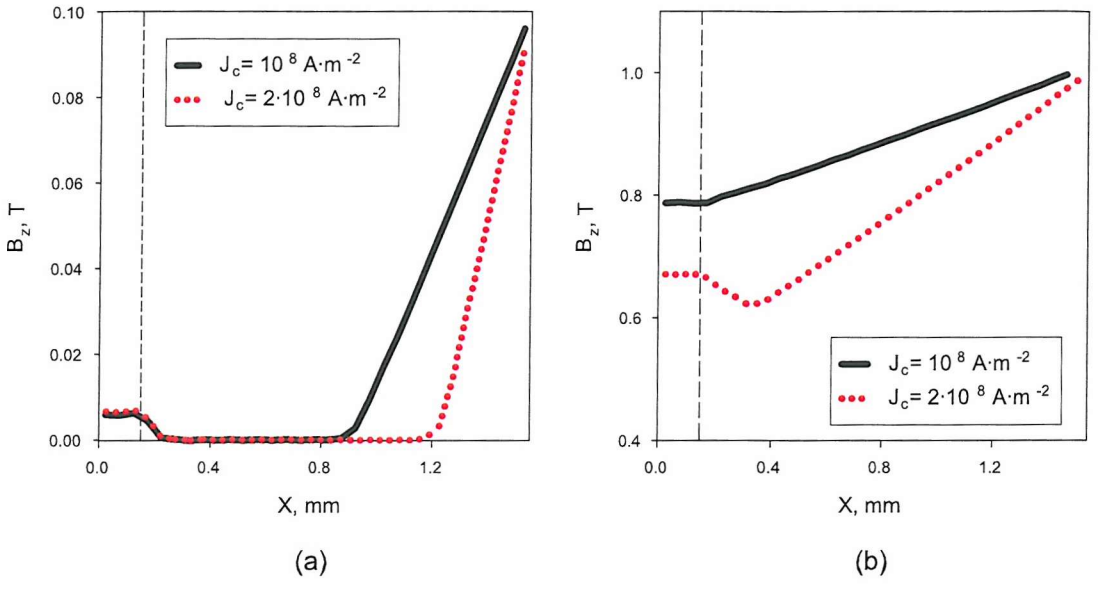

Figure 5.20: Magnetic field profile along the x-axis in the middle ($y = z = 0$) of the slab at: (a) $\mu_0 H_a = 0.1\,\mathrm{T}$ and ramp rate $39.811\,\mathrm{Ts}^{-1}$, and (b) $\mu_0 H_a = 1\,\mathrm{T}$ and ramp rate $25.119\,\mathrm{Ts}^{-1}$.

For thin discs, the depth of flux penetration increases with reducing σ_c as it is expected (figure 5.21). Similarly to the slab, the field along x-axis in the normal matrix region is independent of σ_c (5.21.(a)) at low fields, but varies at higher fields (figure 5.21.(b)).

Detailed evaluation of the influence of J_c at different applied fields is represented in figure 5.22 where $\dot{B}_c$ is plotted as a function of the applied field. Observe for the slab (figure 5.22.(a)), at low fields before total penetration, the unexpected independence of the critical ramp rate on J_c. However at higher fields, just after the superconductor with $J_c = 2 \cdot 10^8\,\mathrm{Am}^{-2}$ has reached full penetration, there is a dependence on J_c. Specifically, $\dot{B}_c$ is almost double for $J_c = 2 \cdot 10^8\,\mathrm{Am}^{-2}$ than for $J_c = 10^8\,\mathrm{Am}^{-2}$ when the slabs are saturated in agreement with formula (5.16).

For the thin disc (figure 5.22.(a)) similarly to the slab, $\dot{B}_c$ is independent of J_c for low fields but as the applied field is increased it is observed a stronger influence being $\dot{B}_c$ at full penetration double for $\sigma_c = 2 \cdot 10^4\,\mathrm{Am}^{-1}$ than for $\sigma_c = 10^4\,\mathrm{Am}^{-1}$.

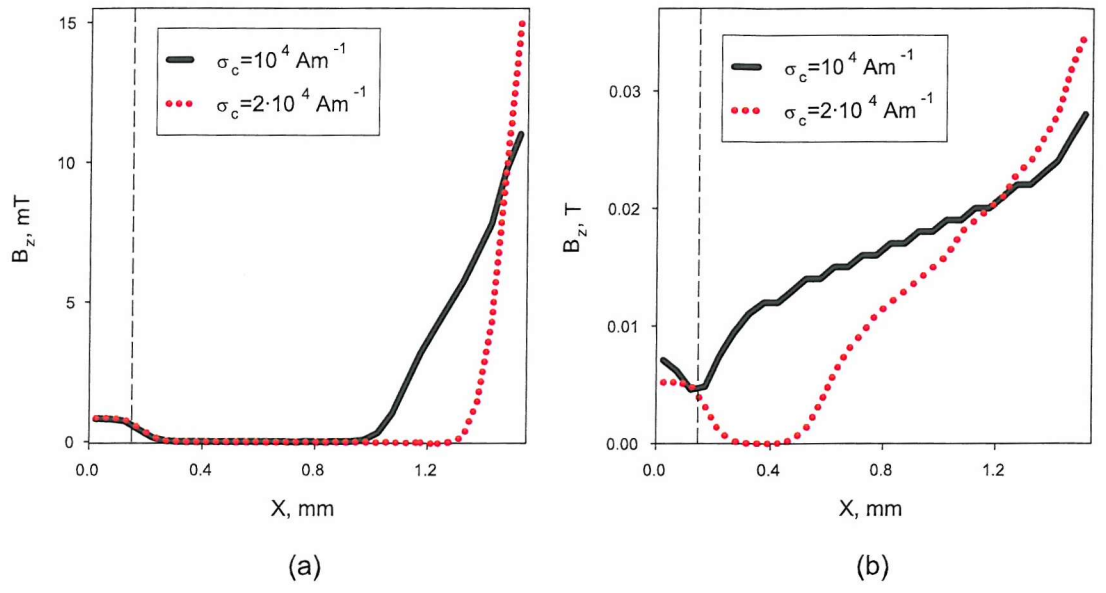

Figure 5.21: Magnetic field profile along the x-axis in the middle ($y = z = 0$) of the thin disc at: (a) $\mu_0 H_a = 5.024 \cdot 10^{-3}\,\mathrm{T}$ and ramp rate $39.811\,\mathrm{Ts}^{-1}$, and (b) $\mu_0 H_a = 0.02\,\mathrm{T}$ and ramp rate $63.096\,\mathrm{Ts}^{-1}$.

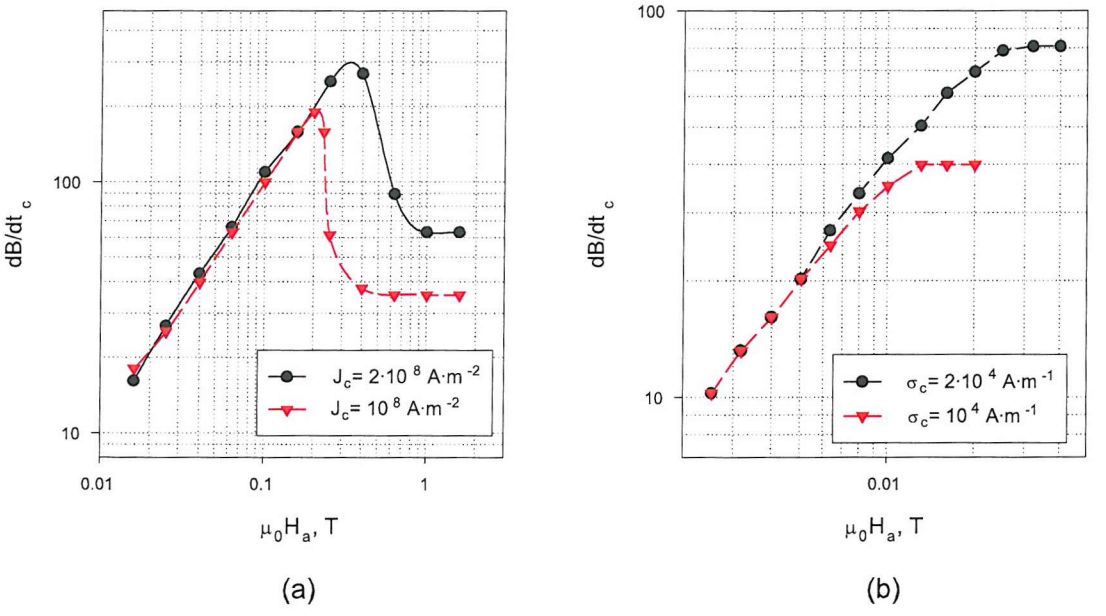

Figure 5.22: Critical field ramp rate as a function of the applied magnetic field for different critical current density J_c of the slab (a) and for different σ_c of the thin discs (b).

5.5.7 Influence of the matrix resistivity of the superconductor

Another parameter which is expected to affect to the coupling effect is the resistivity of the normal metal between the slabs and the sheet resistivity of the normal metal between thin discs. According to equation (5.16) the critical field ramp rate $\dot{B}_c$ is proportional to the resistivity. Figures 5.23 and 5.24 show the field profiles along x-axis for partial penetrated slabs and thin discs respectively. As expected, it is seen less field in the normal matrix and therefore more coupling with reducing the resistivity in both geometries.

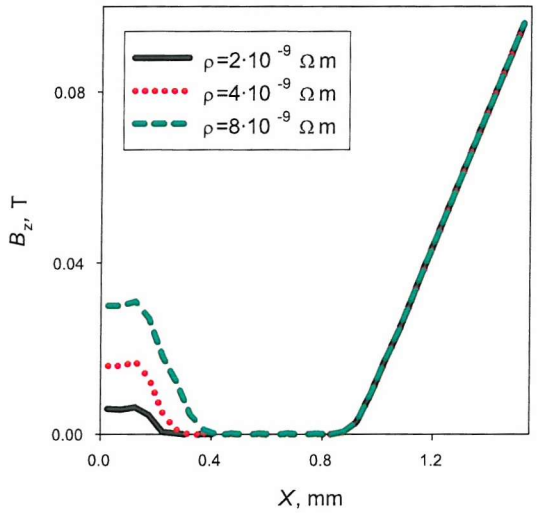

Figure 5.23: Magnetic field profile along the x-axis in the middle ($y = z = 0$) of the slab at $\mu_0 H_a = 0.1\,\mathrm{T}$ and ramp rate $39.811\,\mathrm{Ts}^{-1}$.

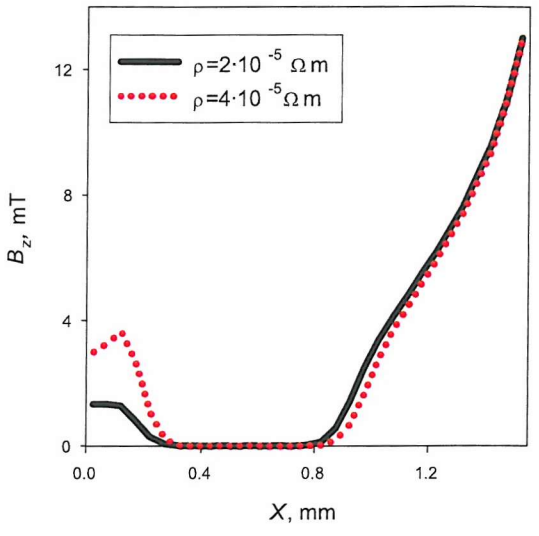

Figure 5.24: Magnetic field profile along the x-axis in the middle ($y = z = 0$) of the thin disc at $\mu_0 H_a = 6.325\,\mathrm{mT}$ and ramp rate $25.119\,\mathrm{Ts}^{-1}$.

The exact values of $\dot{B}_c$ at different applied fields $\mu_0 H_a$ are presented in figure 5.25.(a) for the slab. At any applied field, if the resistivity of the normal metal is reduced, the total coupling produces at a lower ramp rate. The same situation is found for the thin disc, as shown in figure 5.26.(a).

In relation with equation (5.16), the critical ramp rate is plotted divided by the resistivity in figures 5.25.(b) and 5.26.(b) for the slab and thin disc respectively. For the thin disc, $\dot{B}_c$ is directly proportional to the resistivity of the normal matrix. For the infinite slab we found the same relation for both partially penetrated and saturated slabs in accordance with the formula, only for applied fields just after full penetration,

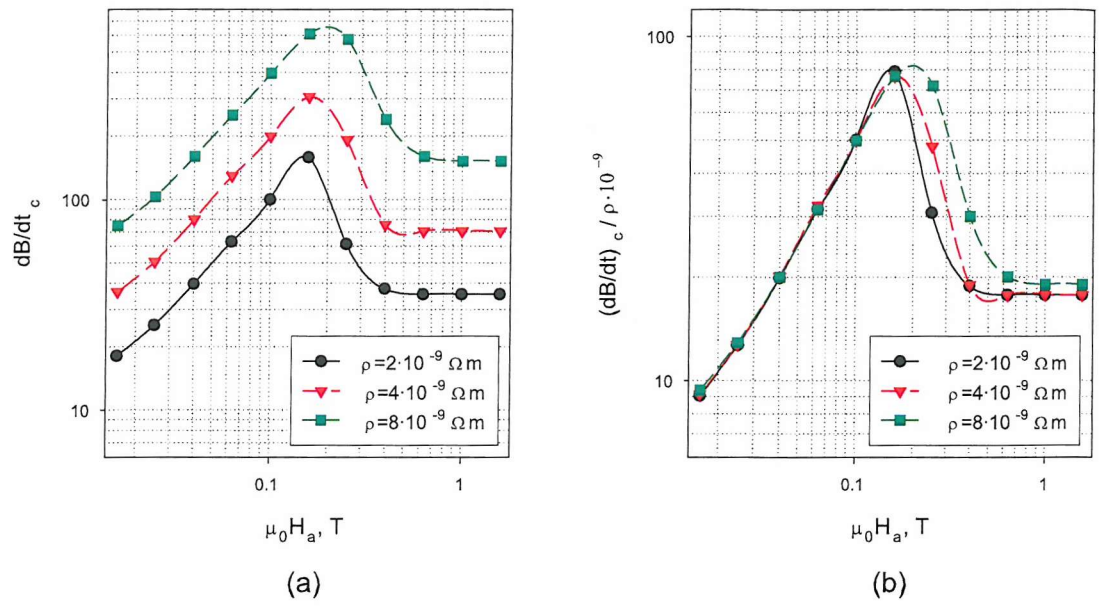

Figure 5.25: Critical field ramp rate for a slab as a function of the applied magnetic field for different resistivity of the normal matrix (a). To verify equation (5.16), the critical ramp rate is divided by the resistivity (b).

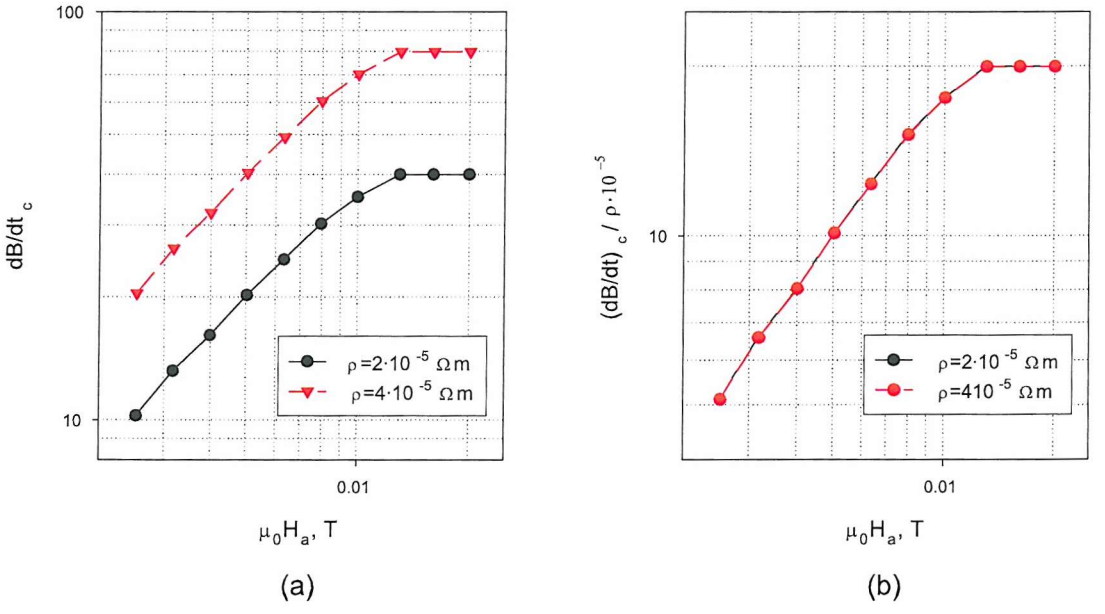

Figure 5.26: Critical field ramp rate for a thin disc as a function of the applied magnetic field for different resistivity of the normal matrix (a). To compare to equation (5.16), the critical ramp rate is divided by the sheet resistivity (b).

the increment of $\dot{B}_c$ with increasing ρ is found more pronounced.

5.5.8 Influence of the matrix width

According to equation (5.16) given for infinite saturated slabs there is not influence of the matrix width on the critical magnetic filed ramp rate $\dot{B}_c$. However numerical results obtained here for $w = 3\,\text{mm}$ and $w = 5\,\text{mm}$ show differences even for the infinite slab, as it can be observed looking at the plots of the field in figures 5.27 and 5.28. Notice that the field in the normal matrix has decreased more for slabs or thin discs separated by thinner matrices indicating that the superconductors couple easily.

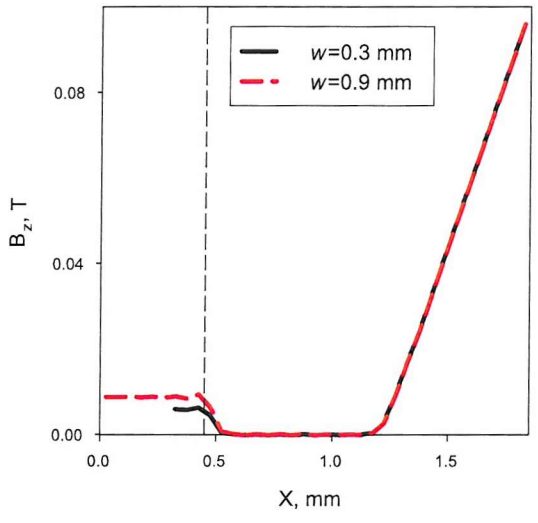

Figure 5.27: Magnetic field profile along the x-axis in the middle ($y = z = 0$) of the thin slab at $\mu_0 H_a = 0.1\,\text{T}$ and ramp rate $39.811\,\text{Ts}^{-1}$.

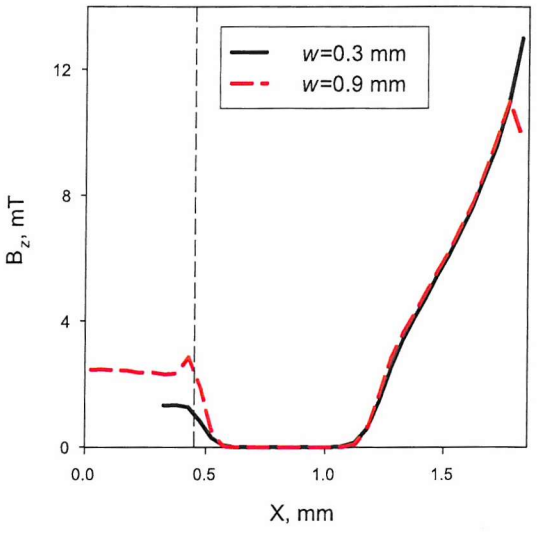

Figure 5.28: Magnetic field profile along the x-axis in the middle ($y = z = 0$) of the thin disc at $\mu_0 H_a = 6.325\,\text{mT}$ and ramp rate $25.119\,\text{Ts}^{-1}$.

This effect is observed not only for low fields but for the whole range of the applied field, as shown in figure 5.29. For both slab and thin discs, the behavior of $\dot{B}_c$ as a function of the applied field is found similar for the different matrix widths, but always requiring a higher $\dot{B}_c$ for the model with wider matrix.

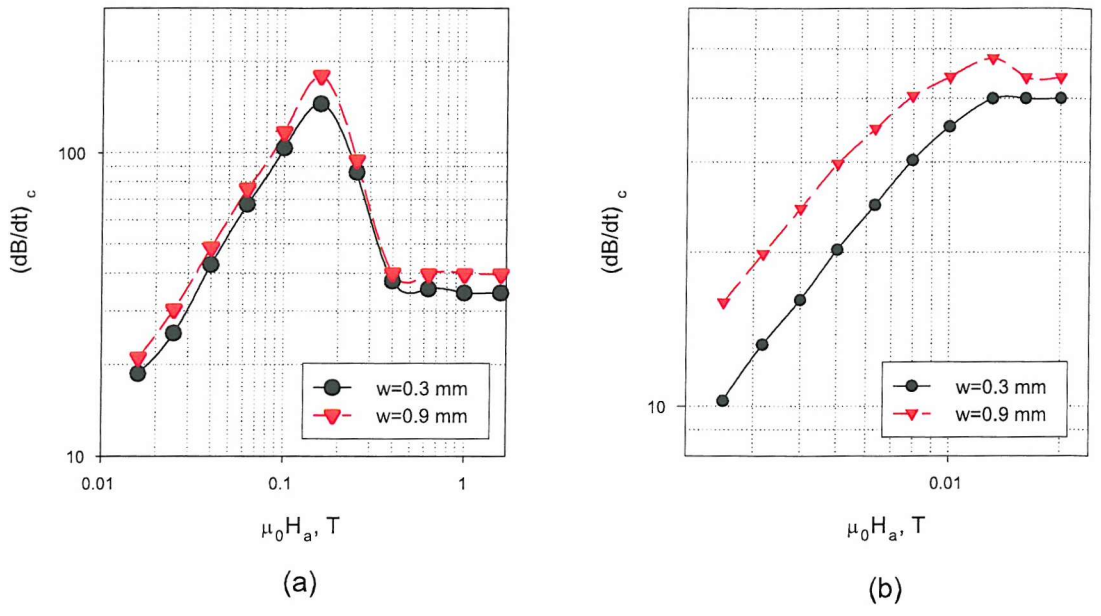

Figure 5.29: Critical field ramp rate as a function of the applied magnetic field for different widths of the normal matrix between slabs (a) and thin discs (b).

5.6 Conclusion

In this chapter an integral method was described for calculating the ac response of thin discs and infinite slabs of finite length. This formulation was extended to study the coupling between two superconductors through a normal matrix. Calculations were carried out in order to obtain $\dot{B}_c$ for infinite slabs and thin discs, as a function of the applied field. The results not only show good agreement with the theoretical prediction for fully penetrated slabs, but also provided previously unknown correlations for partially penetrated superconductors. In the case of the slab, we have found a strong dependence of the $\dot{B}_c$ on the field penetration at low fields. $\dot{B}_c$ increases linearly with the applied field until the slab is saturated, then reduces to a constant equal to the value given by theory. For the thin disc, although $\dot{B}_c$ also increases with the applied field, it does not reach such a high peak as the slab. Although it was expected a lower $\dot{B}_c$ for thin discs due to demagnetization effect, for high fields we found similar values in both geometries. This is due to the increase in the resistance between the discs compared with the slabs. It should be noted that the situation is the reverse for twisted conductors, where the coupling current flows along the direction of the applied field.

Quantitative analysis of the influence on the critical coupling field rate of parameters such as the critical current density, the length of the superconductors and the normal matrix resistivity, was given. Whereas results varying such parameters showed an agreement with theoretical prediction for infinite saturated slabs, it was found that the width of the normal matrix influences $\dot{B}_c$ in disagreement with the independence between both parameters expected by theory.

Despite the simplicity of the formulation it has been very effective for modelling both geometries considered here. Further work could be done in order to refine the formulation and apply it to finite superconductors of finite height.

Chapter 6

Further work and recommendations

Integration formulation can be used for modelling infinite slabs and thin discs with finite length in an ac applied field, as it was shown in chapter 5. Since in both geometries the induced current is restricted to a plane, it is possible to obtain the integral equation for the stream function g of the current density ($\mathbf{J}(x,y) = -\hat{\mathbf{z}} \times \nabla g(x,y)$) satisfying div$\mathbf{J} = 0$.

The same formulations could be extended to model superconductors with finite dimensions proved that the induced current has not component in the direction of the applied field and therefore the current is restricted to a plane. Figure 6.1 shows the geometry of the superconductor indicating the profile of the induced current.

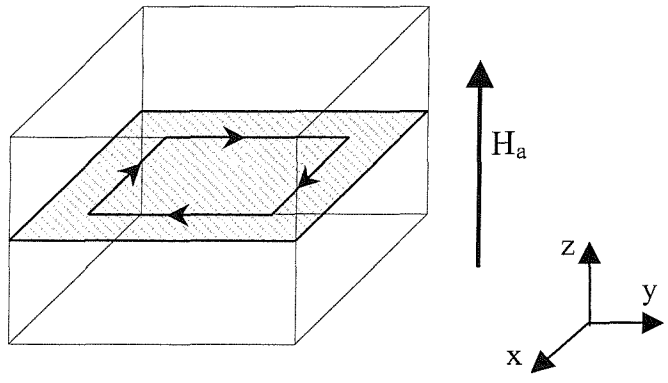

Figure 6.1: Sketch of the induced currents in a finite superconductor under an ac applied field.

The profile of the different components of the induced current in the xy-plane at $z = b/2$, being $2b = 10\,\text{mm}$ the height of the superconductor, was calculated with Flux3D and is shown in figure 6.2. Observe that the z-component of the current is negligible compared to the other ones.

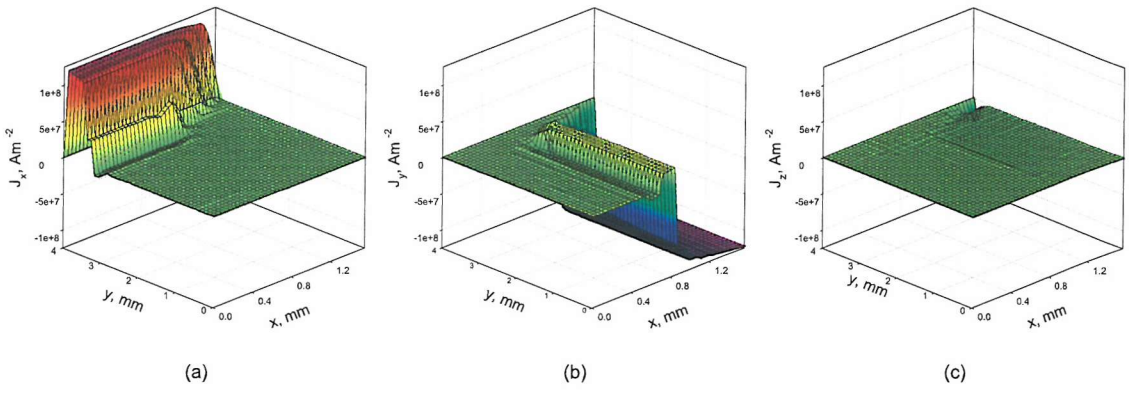

Figure 6.2: Profiles of J_x (a), J_y (b) and J_z (c), obtained with Flux3D in a finite superconductor under an ac applied field.

The stream function $g(x, y, z)$ varies in z due to the finite height and relates to the current by

$$\mathbf{J}(x, y, z) = -\hat{\mathbf{z}} \times \nabla g(x, y, z) = \frac{\partial g}{\partial y}\hat{i} - \frac{\partial g}{\partial x}\hat{j} \tag{6.1}$$

Similarly to the infinite slab, it is necessary to find a relation between the stream function g and the field distribution given by a scalar function Q, corresponding to the magnetic field generated by sheet current cylinders of finite height.

Tabulating the functions in a volume with points $\mathbf{r} = (x, y, z)$ covering the total volume the solution could be easily obtained.

Bibliography

[1] A. A. Abrikosov, *On the magnetic properties of superconductors of the second group*, Sov. Phys. JETP **5** (1957), 1174.

[2] P. Alméras, T. Dell'Orto, C. Coluzza, J. R. L. de Almeida, G. Margaritondo, Y. Y. Xue, R. L. Meng, and C. W. Chu, *Local chemical composition of HBCCO HTS's*, Journal of Applied Physics **76** (1994), 1100.

[3] N. Amemiya, K. Miyamoto, S. Murasawa, H. Mukai, and K. Ohmatsu, *Finite element analysis of ac loss in non-twisted Bi-2223 tape carrying ac transport current and/or exposed to dc or ac external magnetic field*, Physica C **310** (1998), 30–35.

[4] S. P. Ashworth and M. Suenaga, *The calorimetric measurement of losses in HTS tapes due to ac magnetic fields and transport currents*, Physica C **315** (1999), 79–84.

[5] C. P. Bean, *Magnetization of high-field superconductors*, Rev. Mod. Phys. **36** (1964), 31–9.

[6] J. G. Bednorz and K. A. Müller, *Possible high-Tc superconductivity in the Ba-La-Cu-O system*, Phys.B **64** (1986), 189–93.

[7] C. Beduz, E. Cereda, B. Dutoit, C. M. Friend, G. F. de la Fuente, T. Hughes, L. Le Lay, R. Navarro, D. M. Spiller, Y. Yang, and S. Zanella, *Electrical AC loss measurements of Bi-2223 tapes, performed under the Brite Euran Research programme SACPA*, Physica C **310** (1998), 67–70.

[8] E. H. Brandt, *Square and rectangular thin superconductors in a transverse magnetic field*, Phys.Rev.Lett. **74** (1995), no. 15, 3025.

[9] E. H. Brandt and M. Indenbom, *Type-II superconductor strip with current in a perpendicular magnetic field*, Physica Review B **48** (1993), no. 17, 12893–12906.

[10] E.H. Brandt, *Superconductors of finite thickness in a perpendicular magnetic field: strips and slabs*, Phys. Rev. B **54** (1996), no. 6, 4246.

[11] R. J. Creswick C. P. Poole, H. A. Farach, *Superconductivity*, Academic Press, London, 1995.

[12] W. J. Carr, *Ac loss and macroscopic theory of superconductors*, Gordon and Breach Science Publishers, New York, 1983.

[13] K. Fujiwara, T. Nakata, and H. Fusayasu, *Acceleration of convergence characteristic of the ICCG method*, IEEE Trans. Magn. **29** (1993), no. 2, 1958–1961.

[14] V. L. Ginzburg and L. D. Landau, *On the theory of superconductivity*, Zh.Eksp.Teor.Fiz.(J. Exp. Theor.Phys.) **20** (1950), 1064.

[15] F. Grilli, M. Costa, Y. Yang, C.Beduz, and B. Dutoit, *Finite element method analysis of the coupling effect between superconducting filaments of different aspect ratio*, Supercond. Sci. Technol. **16** (2003), 1228–1234.

[16] E. Hairer, S.Ps Norsett, and G. Warner, *Solving ordinary differential equations I. Nonstiff problems*, Springer Verlag, Berlin, 1987.

[17] E. Hairer and G. Warner, *Solving ordinary differential equations II. Stiff and differential-algebraic problems*, Springer, Berlin, 1996.

[18] Webpage http://www.cedrat.com.

[19] H. Hughes, Y. Yang, C. Beduz, Z. Yi, L. Jansak, A. E. Mahdi, R. L. Stoll, J. K. Sykulski, M. R. Harris, and R.J.Arnold, *Measurements of sellf-field AC losses in PbBi-2223 Ag-sheathed tapes*, Physica C **235-240** (1994), 3423–3424.

[20] A. E. Mahdi J. K. Sykulski, R. L. Stoll and C. P. Please, *Modelling HTc superconductors for ac power loss estimation*, IEEE Trans.Magn. **33** (1997), no. 2, 1568–71.

[21] D. A. H. Jacobs, *A generalization of the conjugate gradient method to solve complex systems*, IMA J.Numerical Anal. **6** (1986), 447–452.

[22] F. London and H. London, *The electromagnetic equations of the superconductor*, Proc. Roy. Soc. **A149** (1935), 71.

[23] M. Maslouh, F. Bouillault, A. Bossavit, and J. Vérité, *From Bean's model to the H-M characteristic of a superconductor: some numerical experiments*, IEEE Trans. Appl. Supercond. **7** (1997), no. 3, 3797.

[24] W. Meissner and R. Ochenfeld, *Ein neuer effekt bei entritt der supraleitfähigkeit*, Die Naturwissenschaften **21** (1933), 787–8.

[25] W. T. Norris, *Calculation of hysteresis losses in hard superconductors carrying ac: isolated conductors and edges of thin sheets*, J.Phys. D **3** (1970), 489–507.

[26] H. Kamerlingh Onnes, *Further experiments with liquid helium. On the change of the electrical resistance of pure metal at very low temperature*, Leiden Comm. **120b,122b,124c** (1911).

[27] A. Ostermann, P. Kaps, and T. D. Bui, *The solution of a combustion problem with Rosenbrock methods*, ACM Transactions on Mathematical Software (TOMS) **12** (1998), 42–47.

[28] Y. Saad, *Ilut, a dual threshold incomplete ilut factorization*, Num.Lin.Alg. **1** (1994), 387–403.

[29] Y. Saad and M. H. Schultz, *Gmres:a generalized minimal residual algorithm for solving nonsymetric linear systems*, SIAM J.Sci.Comput. **7** (1986), 856–869.

[30] A. Sandu, J. G. Verwer, J. G. Blom, E. J. Spee, and G. R. Carmichael, *Benchmarking stiff ODE solvers for atmospheric chemistry problems II: Rosenbrock solvers*, Atmospheric Environment **31** (1997), 3459–3472.

[31] A. Sandu, J. G. Verwer, M. Van Loon, G.R. Carmichael, F.A. Potra, D. Dabdub, and J.H. Seinfeld, *Benchmarking stiff ODE solvers for atmospheric chemistry problems I: implicit versus explicit*, Atmospheric Environment **31** (1997), 3151–3166.

[32] Th. Schuster, H. Kuhn, and E. H. Brandt, *Flux penetration into flat rectangular superconductors with anisotropic critical current*, Phys.Rev.B **56** (1997), no. 6, 3413.

[33] T. P. Sheahen, *Introduction to high-temperature superconductivity*, Plenum Press, New York, 1994.

[34] S. Stavrev, F. Grilli, B. Dutoit, N. Nibbio, E. Vinot, I.Klutsch, G. Meunier, P. Tixador, Y. Yang, and E. Martinez, *Comparison of numerical methods for modelling of superconductors*, IEEE Trans. Magn. **38** (2002), no. 2, 849.

[35] J. G. Verwer, E. J. Spee, J. G. Blom, and W. Hundsdorfer, *A second order Rosenbrock method applied to photochemical dispersion problems*, SIAM J. Sci. Comput. **20** (1999), 1456–1480.

[36] E. Vinot, G. Meunier, and P. Tixador, *Different formulations to model superconductors*, IEEE Trans. Magn. **36** (2000), no. 4, 1226–29.

[37] H. A. Van Der Vorst, *Bi-CGSTAB: A fast and smoothly converging variant of BI-CG for the solution of nonsymmetric linear systems.*, SIAM J.Sci.Comput. **13** (1992), 631–644.

[38] M. N. Wilson, *Superconducting magnets*, Oxford: Clarendon Press, New York, 1982.

[39] M. K. Wu, J. R. Ashburn, C. J. Torng, P. H. Hor, R. L. Meng, L. Gao, Z. J. Huang, Y. Q. Wang, and C. W. Chu, *Superconductivity at 93 k in a new mixed-phase Y-Ba-Cu-O compound system at ambient pressure*, Phys. Rev. Lett. **58** (1987), 908–910.

[40] Y. Yang, T. J. Hughes, C. Beduz, and F. Darmann, *Experimental study on ac losses in AG sheathed PbBi2223 tapes with twist filaments*, Physica C **310** (1998), 147–153.

[41] Y. Yang and E. Martinez, *Handbook of superconducting material*, Zd D A Cardwell and D S Grinley IOP Publishing Litd, 2003.

[42] Y. Yang, E. Martinez, and C. Beduz, *Numerical modelling of the critical state and calculation of ac losses and current profiles in multifilamentary Bi-2223 tapes*, Inst.Phys.Conf.Ser. **167** (1999), 855–858.

[43] T. Yazawa, J. J. Rabbers, B. ten Haken, H. H. J. ten Kate, and Y. Yamada, *Numerical calculation of current density distributions in high temperature superconducting tapes with finite thickness in self field and external field*, Physica C **310** (1998), 36–41.

[44] Y.Saad, *Iterative methods for sparse linear systems*, January 3RD 2000.